Quantification of Carbon Contamination Resulting from Sample Preparation in Transmission Electron Microscopy

Dissertation

Zur Erlangung des akademischen Grades

Doktors der Naturwissenschaften

- Dr. rer. nat. -

vorgelegt von

Julia Elisabeth Menten, M.Sc.

geboren in Waltham, Massachusetts / USA

Fakultät für Chemie

der

Universität Duisburg-Essen

2023

DuEPublico

Duisburg-Essen Publications online

UNIVERSITÄT DUISBURG ESSEN

Offen im Denken

ub | universitäts bibliothek

Diese Dissertation wird via DuEPublico, dem Dokumenten- und Publikationsserver der Universität Duisburg-Essen, zur Verfügung gestellt und liegt auch als Print-Version vor.

DOI: 10.17185/duepublico/81892
URN: urn:nbn:de:hbz:465-20240503-070157-5

Alle Rechte vorbehalten.

Promotionsausschuss:

1. Gutachter: Prof. Dr. Robert Schlögl

2. Gutachter: Prof. Dr. Andreas Hütten

Prüfungsvorsitzender: Prof. Dr. Eckhard Spohr

Disputation am 9. April 2024

In omnibus negotiis prius quam aggrediare, adhibenda est praeparatio diligens. – In all matters, before beginning, a diligent preparation should be made.

Marcus Tullius Cicero, De Officiis

Before anything else, preparation is the key to success.

Ascribed to Alexander Graham Bell

Abstract

Transmission electron microscopy (TEM) is a powerful technique for high resolution investigations of specimens that is of much current research interest. Often, TEM measurements are impaired by carbon contamination, which arises when volatile organic components (VOCs) are reduced by the electron probe and form amorphous carbon on the studied sample. This results in a layer of contamination that increases the overall thickness of the sample and therefore decreases the quality of images and spectroscopic data obtainable from TEM investigations. In the course of the work reported here, carbon contamination in TEM experiments resulting from the processes involved in sample preparation was investigated.

One aim of this work is the analysis of solvent contamination resulting from outgassing at environmental TEM pressure, which is studied by proton-transfer-reaction mass spectrometry. In addition, the adsorption of contaminating species to the surfaces of the octagon and removal of these VOCs by applying high vacuum and plasma cleaning is discussed.

Another part of this thesis focuses on carbon contamination accumulated by electron beam exposure, which was quantified by electron energy loss spectroscopy thickness measurements. Here, specimens were prepared with different solvents that are commonly used either in chemical synthesis or in the sample preparation process by electron microscopists. The resulting contamination was compared as a function of the drying time and the time a sample remains in the microscope. The efficiency of several established mitigation strategies addressing carbon contamination was studied. Furthermore, utilizing a self-designed and built sample cleaning station for the removal of hydrocarbon contaminants by vacuum is discussed as an additional approach for mitigating carbon contamination.

Zusammenfassung

Transmissionselektronenmikroskopie (TEM) ist eine leistungsstarke Arbeitstechnik zur Untersuchung von Proben und von großem aktuellen Forschungsinteresse. Häufig werden TEM-Messungen durch Kohlenstoffkontamination beeinträchtigt, die entsteht, wenn flüchtige organische Verbindungen vom Elektronenstrahl zu amorphem Kohlenstoff auf der Probe reduziert werden. Dies führt zu einer Kontaminationsschicht, die die Gesamtdicke der Probe erhöht und somit die Qualität der erhaltenen Bilder und spektroskopischen Daten beeinträchtigt. In dieser Arbeit wurde die Kontamination untersucht, die aus der TEM-Probenvorbereitung resultiert.

Ein Teil der Arbeit setzt sich mit der Analyse von ausgasenden Lösungsmittelmolekülen auseinander, die im Druckbereich von ‚environmental' TEM das Vakuum beeinträchtigen. Dieser Prozess wurde mittels Protonen-Transfer-Reaktions-Massenspektrometrie analysiert. Ferner wird die Adsorption kontaminierender Spezies an den Oberflächen des Oktagons und die Entfernung der Verunreinigungen durch das Pumpen in den Hochvakuumbereich und die Anwendung von Plasma zu Reinigungszwecken diskutiert.

Ein weiterer Teil dieser Arbeit befasst sich mit der Kontamination, die durch den Elektronenstrahl akkumuliert wurde. Es wird die Dicke der Probe durch Elektronenenergieverlustspektroskopie-Messungen bestimmt. Dazu wurden Proben mit verschiedenen Lösungsmitteln präpariert, die häufig entweder in der chemischen Synthese oder bei der Probenvorbereitung durch Elektronenmikroskopiker verwendet werden. Die resultierende Kontamination wurde in Abhängigkeit von der Trocknungszeit und der der Verweildauer einer Probe im Elektronenmikroskop untersucht. Zusätzlich wurde die Effizienz verschiedener Methoden zur Verminderung der Kohlenstoffkontamination analysiert und mit einem neuen Ansatz zur Reinigung der Proben durch eine selbstgebaute Probenreinigungsstation verglichen, in der Kohlenwasserstoffverunreinigungen durch Vakuum entfernt werden.

Preface

The work of this thesis was carried out from March 2019 to February 2020 at the Fritz Haber Institute of the Max Planck Society in Berlin in the department of inorganic chemistry and from March 2020 to August 2023 at the Max Planck Institute for Chemical Energy Conversion in Mülheim an der Ruhr in the department of heterogeneous reactions under supervision of Prof. Dr. Robert Schlögl.

This thesis is divided in three main parts, which focus on carbon contamination as a consequence of the sample preparation in transmission electron microscopy. The independent chapters discussing the work of this thesis are written in a manuscript-style for scientific publications, thus some information may be repeated when proceeding through this work.

List of abbreviations

BF	bright field
EDX	energy-dispersive X-Ray
EELS	electron energy loss spectroscopy
ETEM	environmental transmission electron microscopy
HAADF	high-angle annular dark field
HRTEM	high-resolution transmission electron microscopy
iDPC	integrated differential phase contrast
LOD	limit of detection
LOQ	limit of quantification
MS	mass spectrometry
ppb	parts per billion
PTR	proton-transfer-reaction
SCS	sample cleaning setup
SILP	supported ionic liquid phase
STEM	scanning transmission electron microscopy
TEM	transmission electron microscopy
TOF	time-of-flight
UHV	ultra high vacuum
VOC	volatile organic component

Table of Contents

Abstract . . . i

Zusammenfassung . . . ii

Preface . . . iii

List of abbreviations . . . iv

1 Introduction **1**

1.1 Transmission electron microscopy . . . 1

1.2 Carbon contamination in electron microscopy . . . 7

1.3 Removal of residual molecules from a vacuum system . . . 22

1.4 Thickness measurements in TEM . . . 29

1.5 Proton-transfer-reaction mass spectrometry . . . 31

1.6 Outline of this thesis . . . 34

References . . . 37

2 Contamination analysis of the gas composition in environmental transmission electron microscopy **47**

2.1 Abstract . . . 47

2.2 Introduction . . . 48

2.3 Methods . . . 50

2.4 Results . . . 56

2.4.1 Long-term measurements under ETEM conditions . . . 56

2.4.2 Removal of solvent molecules by vacuum . . . 60

2.4.3 Plasma cleaning of the octagon . . . 63

2.4.4 Residual gas composition and fragmentation products . . . 66

2.5 Discussion . . . 74

2.6 Conclusion . . . 78
2.7 Supporting information . . . 80
References . . . 88

3 Carbon contamination in TEM caused by organic solvents utilized for sample preparation 93

3.1 Abstract . . . 93
3.2 Introduction . . . 94
3.3 Methods . . . 96
3.4 Results and discussion . . . 99
3.4.1 Carbon contamination depending on the solvent . . . 99
3.4.2 Comparing different drying times before sample insertion . . . 102
3.4.3 Long-term outgassing of samples in the TEM . . . 103
3.4.4 Wet Solvents . . . 107
3.5 Conclusions . . . 108
3.6 Supporting Information . . . 110
References . . . 116

4 Sample-specific preparation techniques for improved transmission electron microscopy measurements 121

4.1 Abstract . . . 121
4.2 Introduction . . . 122
4.3 Methods . . . 124
4.3.1 TEM sample preparation . . . 124
4.3.2 EELS thickness measurements . . . 124
4.3.3 Contaminant removal using techniques discussed in the literature . 125
4.3.4 SCS working principle . . . 125
4.3.5 Data evaluation of the pressure measurements . . . 128

4.4 Results and discussion 129
4.4.1 Cleaning of TEM samples in the SCS 129
4.4.2 Assessment of the SCS parameters 133
4.4.3 Contamination of TEM grids 135
4.4.4 Comparison of cleaning methods on the example of toluene 141
4.4.5 Nanoparticle samples cleaned by SCS 146
4.5 Conclusions 148
4.6 Supporting information 150
References 156

5 Conclusions and outlook 160

Acknowledgements 165
List of figures 167
List of tables 174
Eigenständigkeitserklärung 176

1 Introduction

1.1 Transmission electron microscopy

Transmission electron microscopy (TEM) is a versatile technique for investigating smallest sample features with a resolution down to the atomic scale. TEM is employed in a multitude of research applications of much interest, including catalysis, energy storage, the life sciences or material research among many others[39]. The resolution in the field of microscopy is given by the Abbe diffraction limit, which dictates that the resolution in light microscopy is limited by the wavelength. In electron microscopy, a far higher resolution is achieved due to the wavelength of electrons being orders of magnitudes shorter, allowing to resolve the features of a sample in much greater detail. In the early 1930s, Max Knoll and Ernst Ruska were the first to publish the concept of a transmission electron microscope[52].

Although, in principle, light and electron microscopy have similarities, the instrumental setup of an electron microscope differs from that of its optical counterpart:

- For magnifying and focusing the electron beam, electromagnetic lenses instead of optical lenses are required.
- A vacuum in the setup is necessary, as otherwise the electrons would be scattered by a gaseous environment.
- The image and spectroscopic information obtained by TEM experiments need to be collected by detectors and fluorescent screens.

All TEM measurements in this work were carried out on a Thermo Scientific Talos F200X microscope. A schematic overview of the most important components is shown in fig. 1.1.

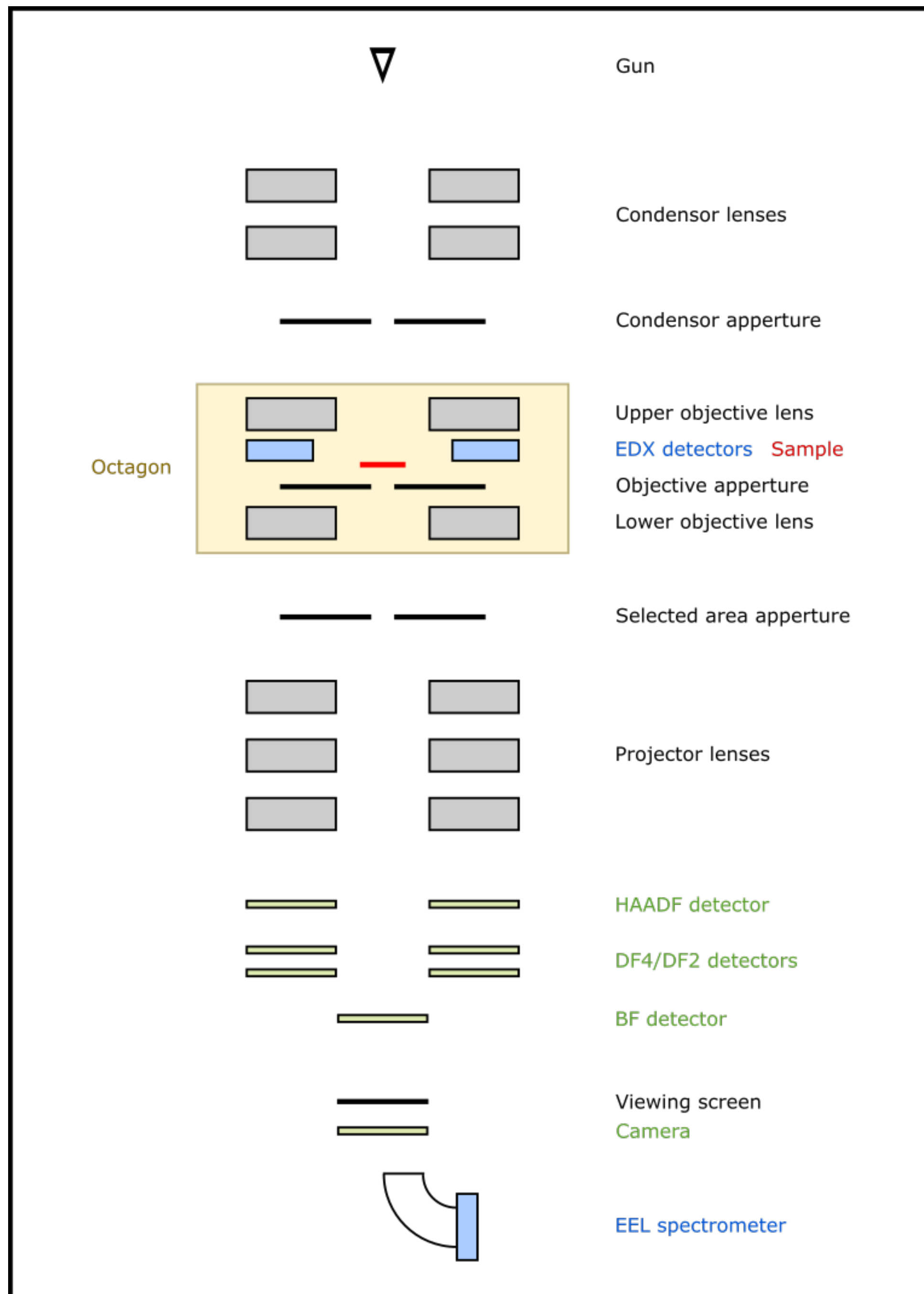

Figure 1.1: Schematic overview of the most important TEM components in a Thermo Scientific Talos F200X microscope.

The electron beam required for probing the specimen is generated in the gun. A Schottky-type electron emitter consists of a filament made out of ZrO-covered tungsten, which is

heated to a temperature of 1700 K, while at the same time a strong electrical field is applied[88]. Under these conditions, the potential barrier of the tip is reduced, allowing for the emission of working electrons.

Electromagnetic lenses focus and magnify the electron beam. The lenses are made out of solenoid magnets, so changes in the applied current result in different deflection properties. Lens systems are required in different parts of the TEM: The condenser, objective and projector lens systems direct the electrons to the image acquisition systems. The condenser lens system illuminates the sample, the objective lenses form the image and in the projection lens system, the image is magnified. The enclosure of the objective lenses and the sample is typically referred to as the octagon of the microscope because it comprises eight vacuum ports that, e.g., are connected to the airlock though which the sample holder is inserted, but also to the vacuum pumping system or the stage for positioning the sample.

A set of imaging and spectroscopic techniques can be applied to investigate the specimens' structural information. Images can be acquired in different operating modes. Components for image acquisition are displayed in green in fig. 1.1. TEM images are obtained by illuminating the sample with a wide-spread electron beam and are captured by the camera located below the viewing screen. For resolving smallest sample features, this method can be extended to high-resolution TEM (HRTEM). In HRTEM, the sample is aligned along a zone axis of the specimen's lattice, and as a result, interference of the beam with the sample's lattice allows for displaying atomic columns. For this, the samples need to be very thin, as a large amount of material would impair the interference required for the image formation. In scanning TEM (STEM) mode, the electron beam scans across a defined small area of the specimen. Depending on the local sample composition, the beam is deflected over a range of different angles that are covered by a set of detectors. The bright field (BF) detector is aligned with the optical axis. Electrons scattered to small angles are collected by the dark field detectors DF2 and DF4, electrons scattered to larger angles are collected by a high-angle annular dark field (HAADF) detector. HAADF images are

of particular relevance for imagining specimens consisting of heavy elements as, due to the high atomic number, Z, of their nuclei, Rutherford scattering leads to large deflection angles, which are $\propto Z^2$. Typical collection semi-angles of each of these detectors in our microscope are listed in table 1.1 for a camera length of 98 mm.

Detector	Collection semi-angle / mrad
BF	0 - 14
DF2	19 - 30
DF4	35 - 85
HAADF	90 - 200

Table 1.1: Typical collection semi-angles of the detectors in the Thermo Scientific Talos F200X microscope at a camera length of 98 mm.

In addition to obtaining images, different spectroscopic devices can give insight in a sample's chemical composition. These are are displayed in blue in fig. 1.1. One spectroscopic method is energy-dispersive X-Ray (EDX) spectroscopy, which allows for determining the elemental composition based on the characteristic X-rays emitted by individual atoms [31]. The electron beam may excite an electron in the inner shell, resulting in an empty vacancy. This gap is filled by another electron from an outer shell, while emitting an X-ray photon at a frequency that corresponds to the energy difference between the outer and the inner shell. In fig. 1.2, an EDX spectrum of a sample consisting of Fe_3O_4 is shown with spectral features arising from different transitions being labeled. Additional signals result from impurities in the sample and the material of the grid and sample holder, respectively, and bremsstrahlung contributes to the background of the measurement.

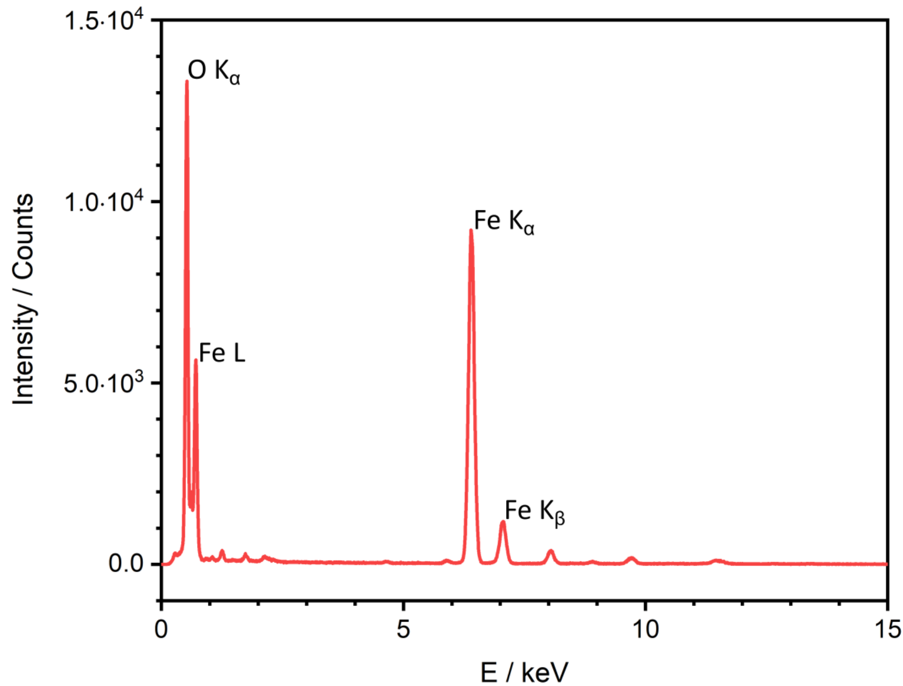

Figure 1.2: Example of an EDX spectrum of an Fe_3O_4 sample. Sample-specific features are labeled.

Another spectroscopic technique is electron energy loss spectroscopy (EELS), where the change of the electron's kinetic energy is measured after the electron beam, which is divided by a post-column filter, has interacted with the sample[18]. A wealth of structural and chemical information can be obtained with this analytical method. In fig. 1.3, the different energy loss regions are shown for a sample consisting of Fe_3O_4: In fig. 1.3(a), the zero loss signal can be seen, which consists of electrons that are not part of inelastic scattering events. By determining the full width at half maximum of the zero loss signal, the energy resolution for the chosen settings can be determined. The low loss region shown in fig. 1.3(b), with an energy loss of up to 50 eV represents the regime in which the incident electron beam interacts with weakly bound outer shell electrons of the sample. This part of the spectrum provides information on plasmon excitation and the band structure[17]. At higher energies in the core loss region (> 50 eV), elements and their oxidation states can

be identified by characteristic features at specific energies[80], as illustrated by fig. 1.3(c). At an energy of 532 eV, the O K edge occurs, while at 721 eV and 708 eV, the Fe L_2 and Fe L_3 edges contribute to the spectrum. The local oxidation state can be determined from the amplitude ratio of the two Fe edge features and their energy shifts.

By considering both the zero loss peak and the total spectrum intensity, also the sample thickness can be determined[18], which is discussed in section 1.4.

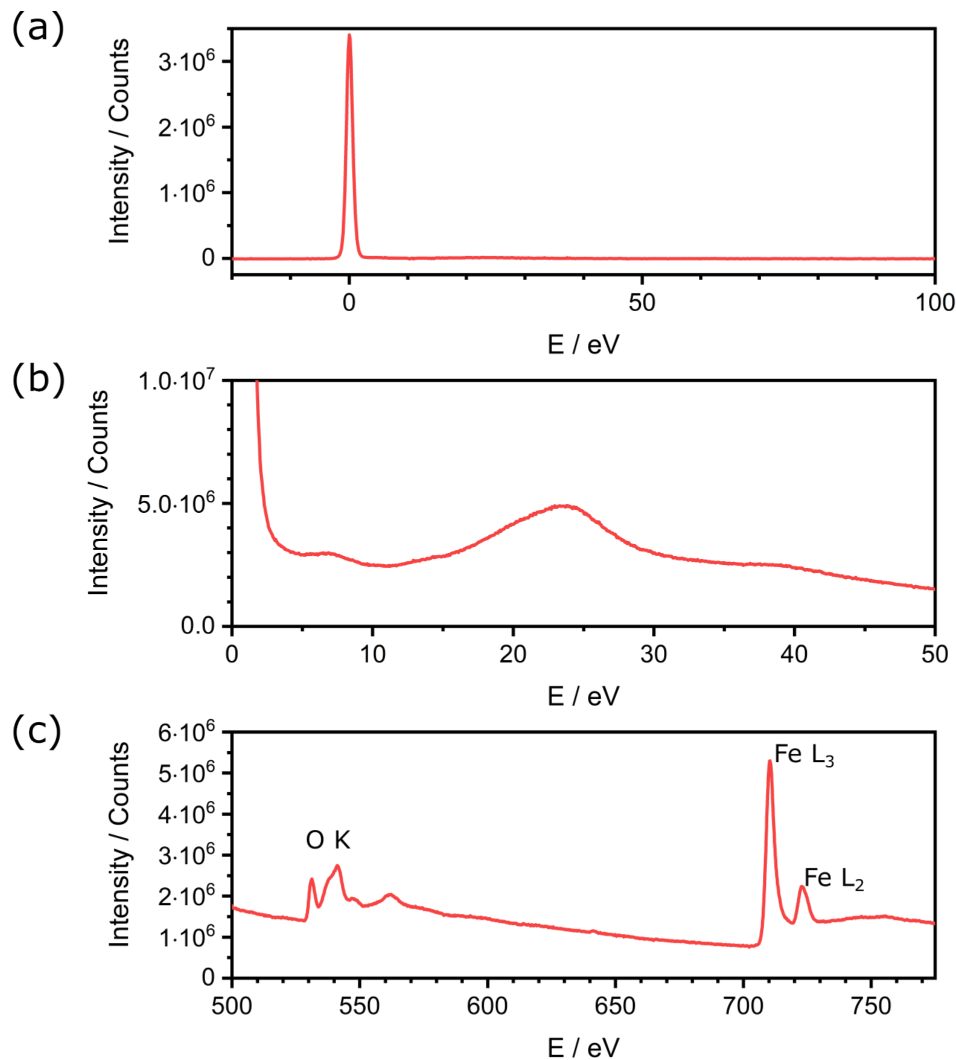

Figure 1.3: Zero loss signal (a), low loss spectrum (b) and core loss spectrum (c) of EELS data of a Fe_3O_4 sample. Data was acquired with a pixel exposure time of $5 \cdot 10^{-6}$ s, $2 \cdot 10^{-4}$ s and 0.5 s, respectively.

Nowadays, TEM experiments are not limited to measurements in vacuum. Obtaining information about specimens when exposed to external stimuli has gained more and more in relevance. Some applications made possible by in-situ experiments involve heating, cooling and exposure to electric or magnetic fields. Moreover, measurements of samples in a controlled gas environment are possible[9,39]. In particular, for catalysis research, experiments in a reactive gas environment are of interest[35]. Environmental transmission electron microscopy (ETEM), in which the entire TEM octagon is immersed in a specific gas atmosphere, can be employed for such measurements[9]. Using ETEM, samples can be investigated under conditions that are not suitable for classical TEM: ETEM has a wide variety of applications that reach from biological samples, which can be investigated without being dehydrated, to catalyst samples that require analysis in a reactive gas atmosphere[54]. Moreover, experiments that demand a closed-cell approach with micro-electromechanical systems can be performed at non-standard TEM conditions, e.g., TEM measurements of samples in liquids[13].

TEM experiments have different challenges, that need to be overcome. Obstacles include different elastic and inelastic damaging mechanisms, which can be destructive or reduce the quality of obtained data[8,88]. Knock-on damage displaces atoms of the investigated structure[8,19,22], radiolysis breaks chemicals bonds due to the incident beam[19,20], and electrostatic charging hinders charge compensation due to non-conductive properties[10,41]. Also, specimen heating by the incident beam[8,70] or structural changes (e.g., decomposition[91] or phase segregation[27]) must not be neglected. For mitigating these effects, different strategies can be implemented. These include sample cooling, low-dose experiments and variations of the incident beam energy[20,21].

1.2 Carbon contamination in electron microscopy

In the field of electron microscopy, a long-standing problem regularly faced is the accumulation of carbon contamination on the specimen[23,24,40,44]: Volatile organic components

(VOCs) get reduced when they are exposed to the electron probe and form a layer of carbonaceous material (fig. 1.4).

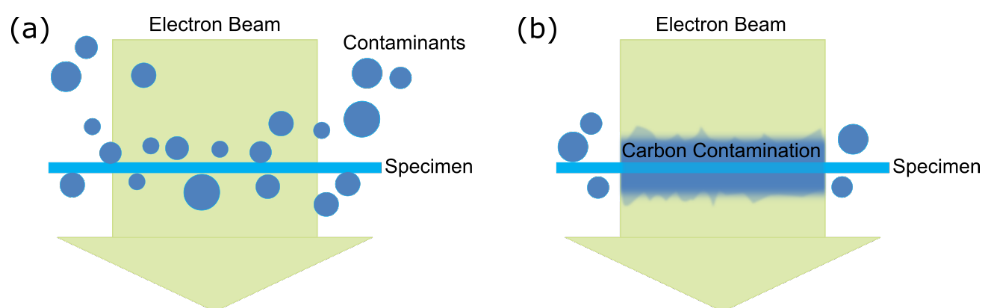

Figure 1.4: (a) Volatile contaminants surround the sample environment and (b) form amorphous carbon when exposed to the electron beam for extended durations.

When exposing hydrocarbon compounds to an ionization source, e.g., the electron beam, different damaging mechanisms might affect these molecules. These include fragmentation, dimerization or polymerization[81], which can result from radical formation by ionization via electron beam exposure[76]. Depending on the hydrocarbon compound, the impact of ionization on chemical bonds differs, though it can be generalized that it is likely that gaseous compounds are removed by the vacuum, while fragments with a high carbon content remain on the TEM grid, where they polymerize[82].

In the early stages of electron microscopy, vacuum technology was not as advanced as later on and oil-diffusion pumps were utilized for achieving a low-pressure environment. These systems had the disadvantage that pumping oil backstreamed into the vacuum chamber and thus impaired the vacuum quality and/or contaminated the sample[37,63,69].

In many cases, contaminants stem from the sample itself in the form of residual solvent molecules from synthesis or from being included as a part of the sample as ligands or stabilizing agents[5,42]. Equipment used for the sample preparation and measurements is another source of contamination that needs to be considered. Grids can be impaired by carbonaceous species[36,64], but also adsorption of contaminants to sample holders is

documented, which can impair the vacuum quality[30]. The thickness of the contamination layer depends on several factors, which include the magnification, the beam current and the irradiation time[23,66,78]. Hydrocarbon contamination growth can be linked to diffusion of adsorbed hydrocarbon compounds towards the electron beam[43,71,74], though contrary observations have also been reported[55].

Techniques requiring a thin specimen are often not applicable when contamination has been accumulated on the sample. For example, in HRTEM the interference of the electron beam along the atomic columns is impaired when amorphous carbon is deposited on the sample's surface. This can be seen for the example of an HRTEM investigation of an Al-4Cu-1Li-0.25Mn alloy; see fig. 1.5. The sample consists of the alloy (dark area) with a precipitate of a different composition (light area), for witch HRTEM investigations were of interest. In fig. 1.5(a), an overview at low magnification can be seen. The sample was investigated at high magnification (fig. 1.5(b)), which resulted in carbon contamination, which can be seen as the bright spots in fig. 1.5(c). While in fig. 1.5(d), on the left hand side of the image, the atomic columns of both phases of the alloy are discernible, on the right hand side carbon contamination was deposited during the investigation, making it impossible to obtain information about the sample's lattice. Again, at lower magnifications, the contamination that has formed a spot with bright contrast is visible in fig. 1.5(e). The goal of such experiments is achieving high-quality images in which the atomic columns can clearly be discerned without being obscured by carbon contamination, like in in fig. 1.5(f)[38].

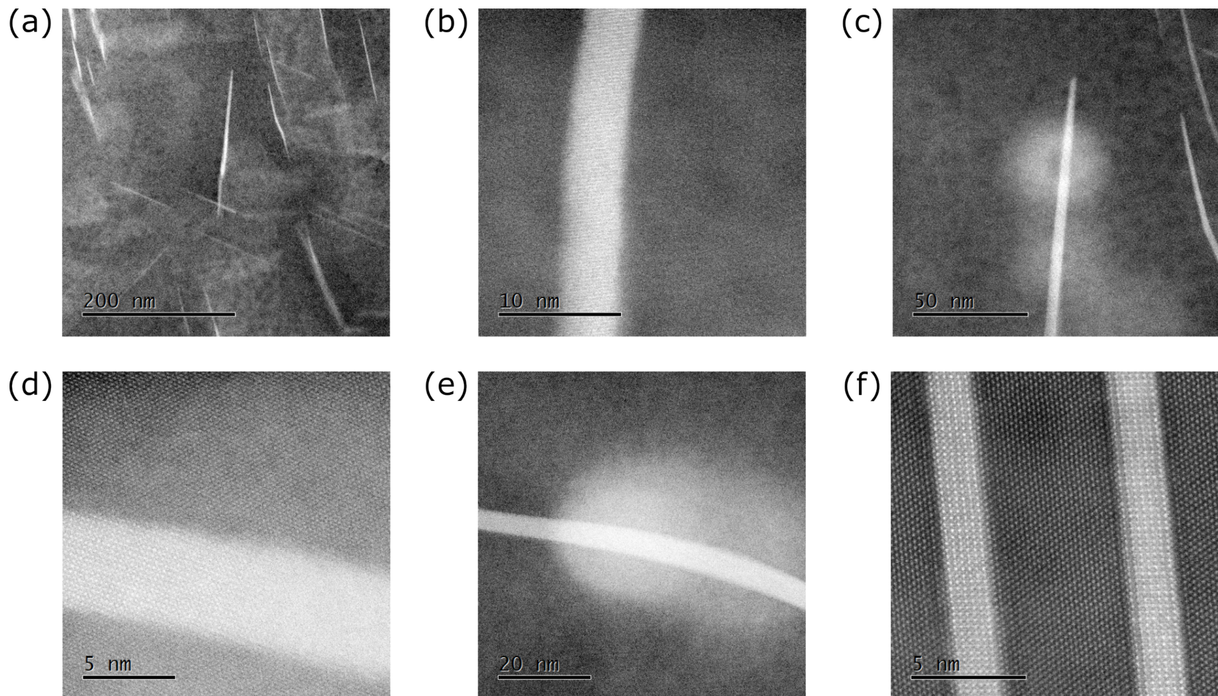

Figure 1.5: (HR)TEM image of an Al-4Cu-1Li-0.25Mn alloy (dark) with a precipitate (light). Subfigure (a) shows the sample at low magnification, (b) shows an area of the sample at high magnification, which was contaminated afterwards (c). In (d), the atomic columns can be displayed on the left hand side, while being obscured by contamination on the right hand side. The contamination of this area can be seen in (e). In (f), the sample is shown with the atomic columns being visible without carbon contamination. Sample provided by Ines Häusler, image taken by Walid Hetaba. Fig. 1.5(f) is published in [38] (license for redistribution: https://creativecommons.org/licenses/by/4.0/).

How carbon contamination can reduce the quality of obtained data is illustrated in fig. 1.6 for a sample consisting of functionalized carbon nanotubes shown before (a) and after (b) the area marked by the red square was scanned for 2 min. In this area, the carbon nanotubes have significantly increased in thickness. At the same time, the surface was contaminated, resulting in a loss of the typical carbon nanotube surface structure, which can be seen in the image taken before extended beam exposure (a). After the sample was scanned for 2 min, the surface appears more homogeneous, indicating the deposition of amorphous carbon. Though this effect is clearly visible in the marked area, these changes

can also be observed in other parts of the image. These images were obtained in scanning electron microscopy mode instead of scanning transmission electron microscopy mode and therefore display the surfaces of the carbon nanotubes well.

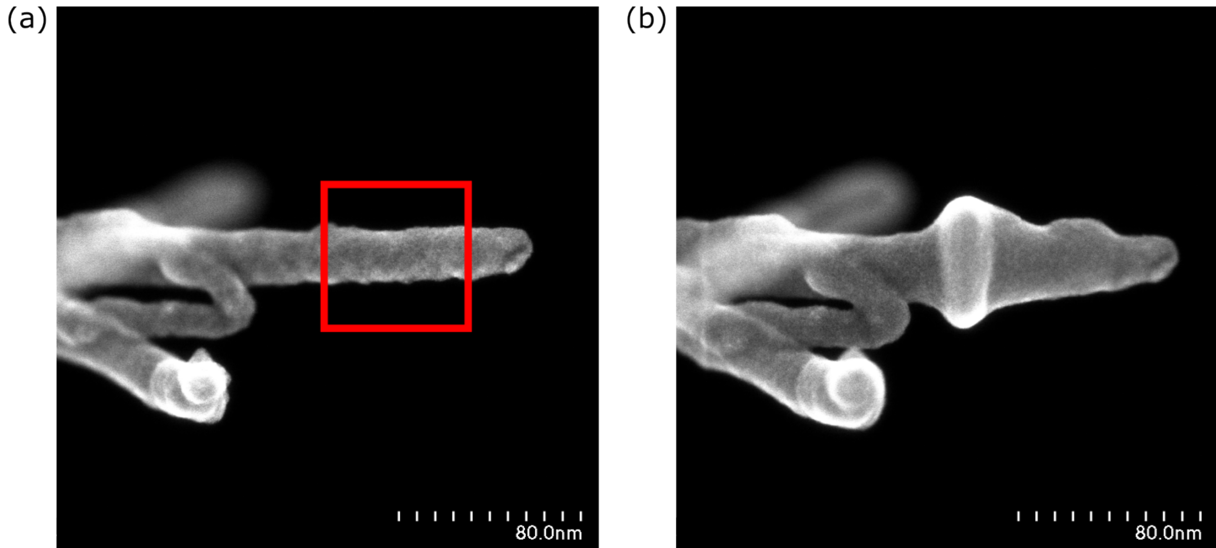

Figure 1.6: Functionalized carbon nanotube sample before (a) and after (b) scanning the area of the sample marked by the red square for 2 min. Sample provided by Wenchao Wan, images taken by Norbert Pfänder.

In STEM, the increased thickness of a contaminated specimen results in beam broadening[14]. This leads to a decrease of the spatial resolution, but also in a loss of contrast in the detectors[16] In EDX spectroscopy, the sample needs to be scanned many times for obtaining a high quality spectrum. With each scan, the observed area gets thicker as carbon is accumulated on it. This results in a loss of spatial resolution and makes elemental quantification more difficult, as bremsstrahlung from carbon can exceed the intensity of other elemental signals. An example is presented in fig. 1.7, which shows a sample of manganese nanoparticles that were prepared in mesitylene and investigated by EDX for gaining insight in the sample composition without focus on displaying the particles. The investigated area at the bottom was analyzed by scanning 876 frames with a dwell time of 20 µs, which corresponds to a frame time of 1.71 s. The strongly contaminated spot is where the beam was placed in between measurements by the microscope.For acquiring

the images after EDX analysis, the contrast settings in the detectors had to be adjusted, as otherwise the exposed area would have been too bright in the case of the HAADF image and too dark in case of the BF image. Despite these adjustments, the contrast is weaker after EDX analysis, as the sample thickness has significantly increased. Even though here only the general sample composition was determined, the increased thickness makes investigations of small structures like displaying single nanoparticles challenging.

Moreover, the elemental composition of the sample, as determined by EDX, significantly changes: When averaging the signal from the first 50 scans and comparing the result with that the summed signal of the last 50 scans, the overall atomic fraction of carbon increases, while that of the manganese, oxygen and chlorine becomes smaller. The corresponding spectra are shown in fig. 1.8. While the count rate of sample components like manganese remains similar, at the same time, the count rate of carbon significantly increases. The increase of the oxygen and silicon signals are likely linked to silica, which was part of the sample. A part of the residual mesitylene is adsorbed to the porous structure of the silica and therefore, silica diffuses towards the electron beam as well.

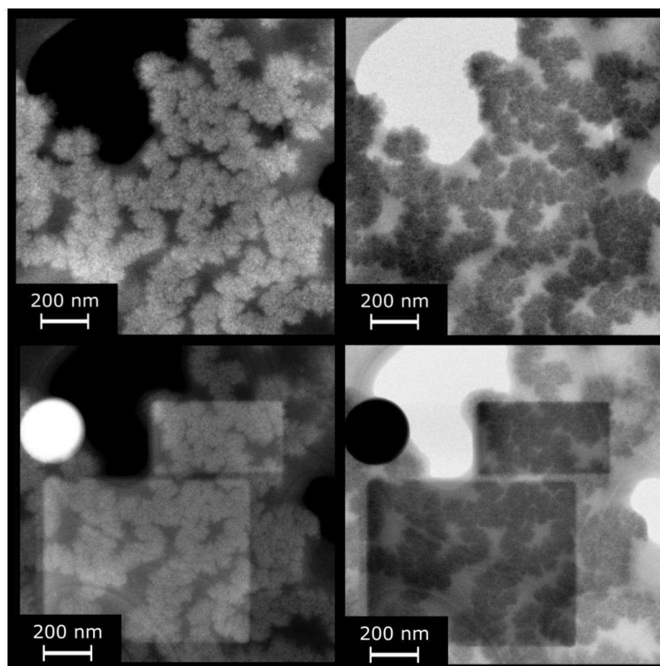

Figure 1.7: HAADF (left) and BF (right) images of manganese nanoparticles before (top) and after (bottom) EDX analysis.

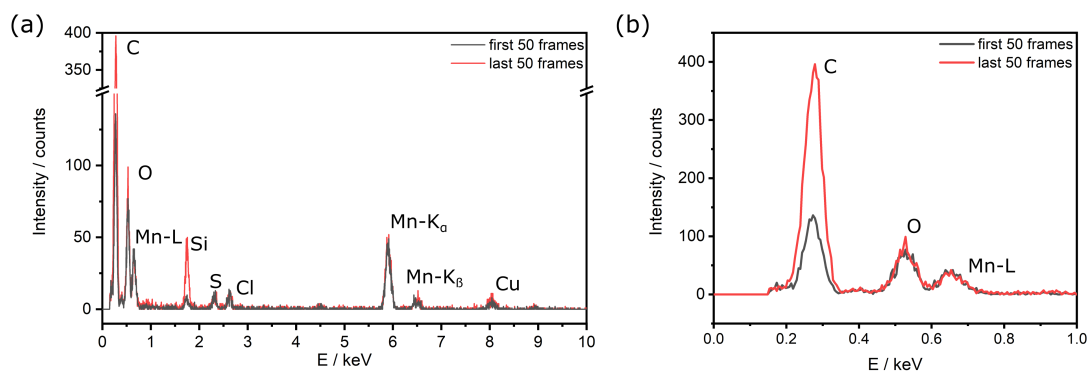

Figure 1.8: Spectra of the first 50 and the last 50 scans of manganese nanoparticles obtained during EDX analysis (a), with the energy range between 0 keV and 1 keV. An enlargement is shown in (b).

The main components of the samples and their atomic fractions are listed in table 1.2.

Element	atomic fraction (first 50 frames) / %	atomic fraction (last 50 frames) / %
C	66.1±2.6	81.6±1.6
O	18.3±3.0	8.1±1.6
Mn	9.5±1.4	4.2±0.6
Cl	1.9±0.3	0.8±0.3
other elements	4.2	5.3

Table 1.2: Atomic fraction in % by averaging the signal of the first 50 frames and last 50 frames.

While manganese and oxygen can be detected at the same ratio, it becomes more difficult to detect elements like chlorine, which are only present in small traces.

The influence of carbon contamination on samples requiring high magnification is shown in fig. 1.9. The investigated sample consists of ruthenium nanoparticles embedded in supported ionic liquid phase (SILP)[72]. Though a dry sample preparation without any additional solvent was possible, the SILP itself contains high amounts of carbonaceous material for anchoring the nanoparticles to the surrounding silica. For EDX acquisition, 360 frames were taken with a dwell time of 25 µs corresponding to a frame time of 7.5 s. The long dwell time was chosen to receive a high enough number of counts to allow a determination of the sample's elemental composition despite the small sample volume determined by the high magnification. The electron beam exposure has led to agglomeration of some particles, while other particles remained in their original state. Especially small particles lack contrast at the end of the EDX measurement due to the sample thickness. In addition, the silica support functionalized with SILP displayed well at the beginning, while later on it could not be studied anymore. The area after EDX analysis is shown in fig. 1.9(c), with the bright portion in the center being the investigated area. The example of these nanoparticles demonstrates that carbon contamination not only results from solvents used in the sample preparation, but also from components of

the sample itself.

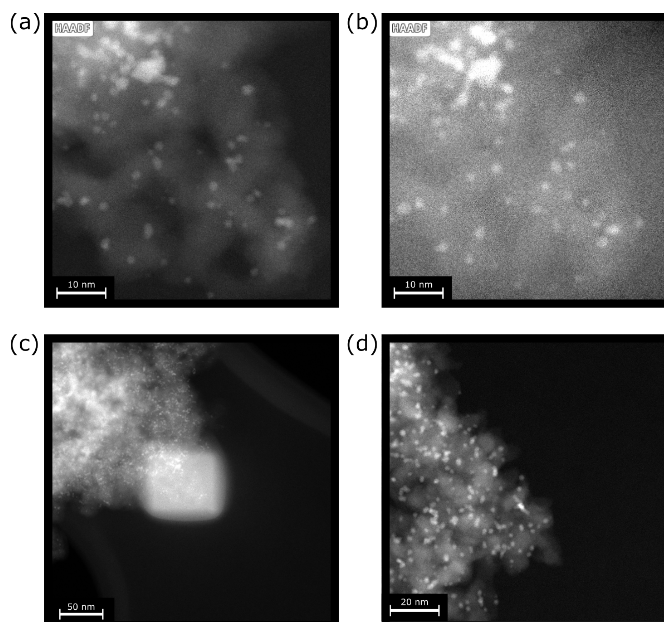

Figure 1.9: HAADF images at the beginning (a) and end (b) of EDX acquisition. The investigated area is shown at a lower magnification in (c). A similar area without contamination is shown in (d).

For the characterization of contamination by EELS, the solvents toluene, THF, methanol, ethanol and isopropanol were applied to silicon TEM membranes and investigated by EELS. By using a grid material that did not contain any carbon, the features of the EEL spectra can be linked exclusively to the modification of the carbon content of the deposited contamination. The sample thickness rapidly increases when exposing the grids to the electron beam, so the spectra could not be measured under ideal conditions. Therefore, they are quite noisy and some features cannot be displayed well due to the weak signal intensity.

Due to the large thickness of the formed contamination layer, the data had to be deconvolved to remove plural scattering events that impair the shape of the EELS features. For this step, the relative sample thickness determined in the low-loss region is considered, which is discussed in depth in section 1.4. The impact of this step for the example of a

toluene sample is illustrated in fig. 1.10. The deconvolved data display relevant features more prominently while, at the same time, the tail of the broad peak is reduced[28]. Displaying the data processed without deconvolution, one notes a broad feature at an energy around 315 eV that can clearly be linked to the plural scattering effects resulting from the sample thickness.

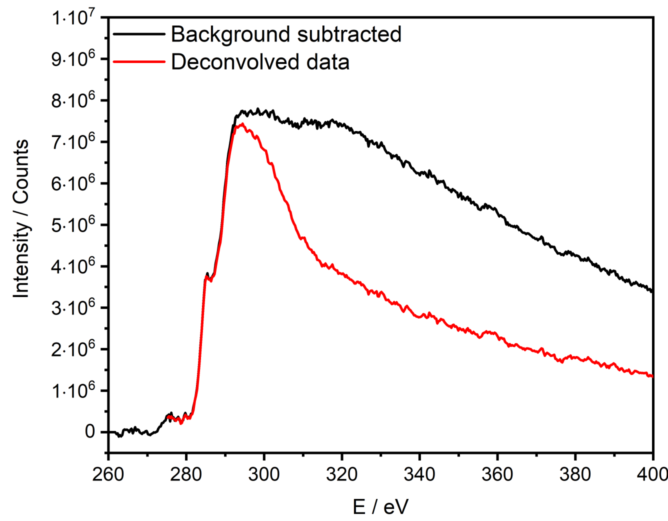

Figure 1.10: EELS measurements of contamination resulting from toluene after background subtraction (black) and after deconvolution of the carbon K-edge (red).

For extracting meaningful data, a high jump ratio of the investigated feature is beneficial. The jump ratio is defined as the ratio of the intensity of the first feature of an elemental edge after background subtraction to the intensity of the background immediately before the rise of this feature, which is supposed to be at least 0.15 in case of carbon as otherwise only little informative value can be extracted from the edges[53].

The EEL spectra of an amorphous carbon film used for TEM sample support and of the contamination resulting from THF are shown in fig. 1.11 (a) and (b), respectively. In the case of the amorphous carbon film, the sample had a relative thickness of 0.19 t/λ, and a jump ratio of 2. The data was collected with a pixel exposure time of 0.02 s and an energy resolution of 1.2 eV. For investigating the contamination resulting from THF, the

sample was measured with 0.01 s/pixel exposure time, had a relative thickness of 0.56 t/λ and and energy resolution of 2.1 eV. The determined jump ratio was 0.12. In the figure, the measured spectrum is shown in black. The background and signal intensities used for the determination of the jump ratio are marked. The background that needs to be subtracted from the total spectrum is shown in red, resulting in the carbon K-edge spectrum, which is displayed in blue. In case of the carbon film, features can be displayed far better, which is necessary for obtaining information about the oxidation state or for elemental quantification by EELS.

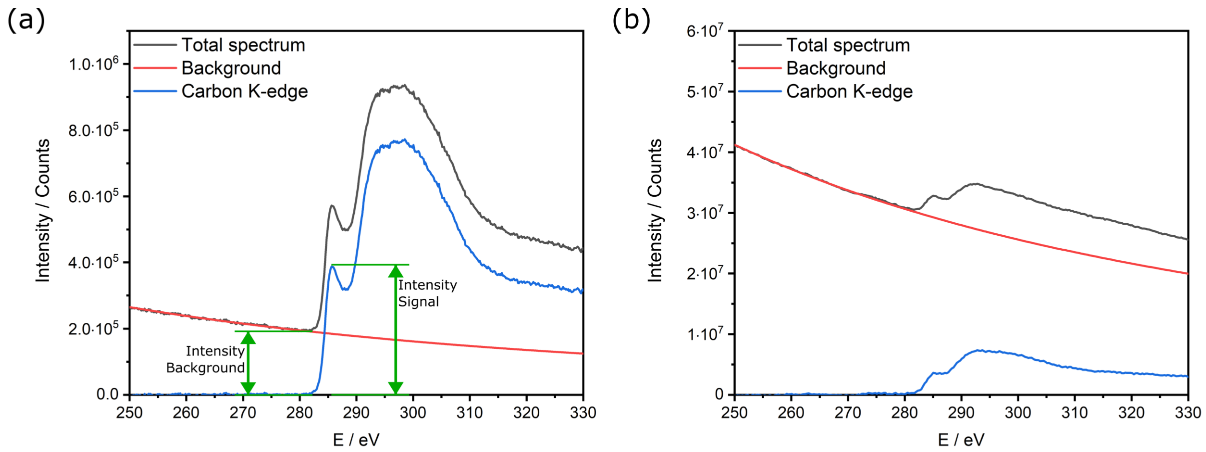

Figure 1.11: EEL spectrum of the carbon K-edge of the amorphous film of a TEM grid (a) and of contamination resulting from THF (b). The total measured spectrum is shown in black, the background is displayed in red. The carbon K-edge after background subtraction is shown in blue. In (a), the green double arrows mark the intensities adopted for the determination of the jump ratio.

In fig. 1.12, the carbon K-edge of contamination deposited from the aforementioned solvents is presented. All samples show the characteristic π^* transition peak at 284 eV, followed by a broad signal with few distinct features. That signal, at approximately 292 eV, can be attributed to σ^* transitions. The signal's shape is typical for amorphous carbon and differs from that of other carbon modifications[4,56,61]. Compared to the spectra of other solvents, those of methanol and isopropanol have a lower intensity, and despite

dedicated attempts at deconvolution, in these spectra features could not be resolved as clearly as in the spectra of other solvents.

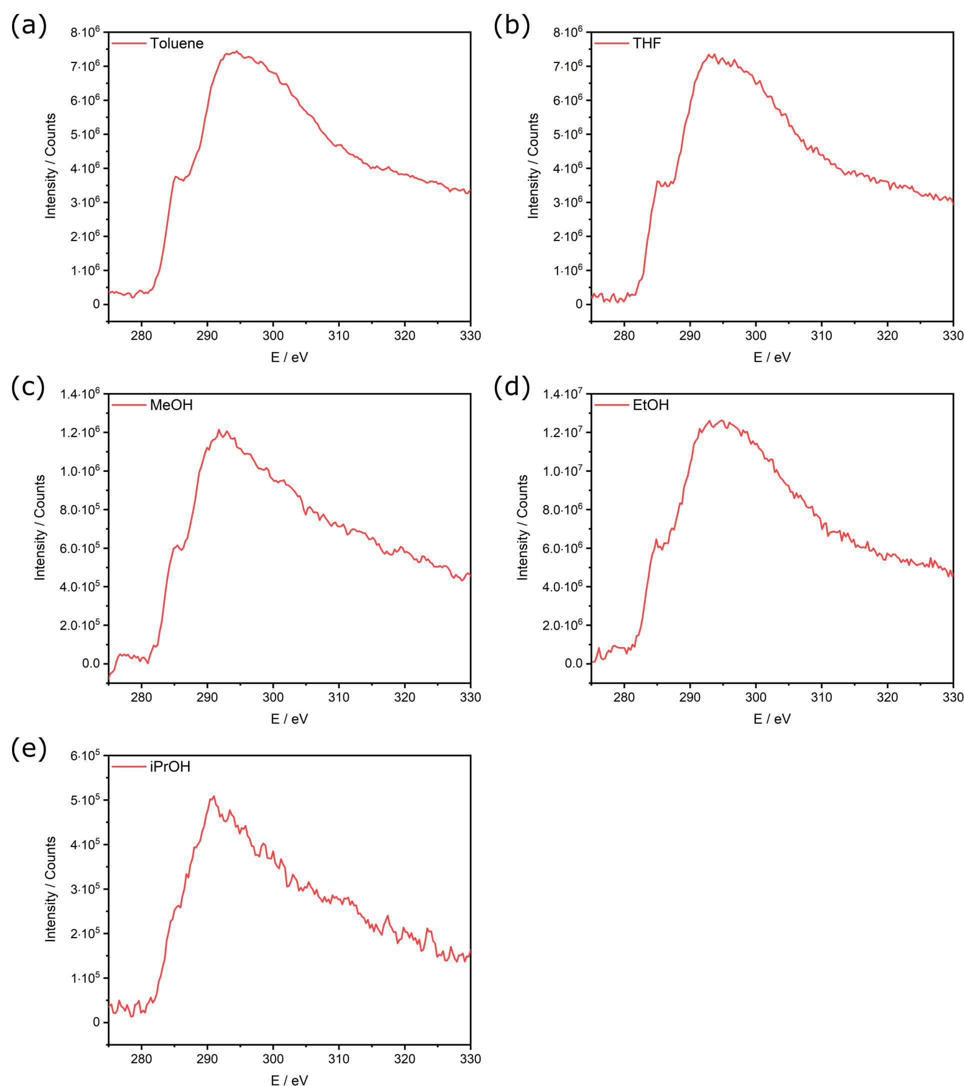

Figure 1.12: EELS measurements of the carbon K-edge of the investigated solvents.

For all samples, the signal of the carbon K-edge was summed up over a certain number of pixels (see table 1.3) in a rather thin part of the investigated area. All spectra were acquired with a dispersion of 0.3 eV and an exposure time of 0.01 s/pixel. The energy resolutions, relative thicknesses and the jump ratio of the EELS measurements are listed in table 1.3. The relative thickness is given in t/λ, which is the ratio of the thickness of

the sample, t, to the inelastic mean free path of the electrons in the sample, λ.

Solvent	Energy resolution / eV	Relative thickness / t/λ	Jump ratio	Summed spectra / px
Toluene	2.1	0.71	0.14	20
THF	2.1	0.56	0.12	22
MeOH	1.5	0.80	0.10	30
EtOH	2.1	0.42	0.09	26
iPrOH	2.1	1.29	0.06	28

Table 1.3: For the carbon K-edge measurents of different solvents, the energy resolution, relative thickness, jump ratio and number of pixel are listed.

The normalized spectra of toluene, EtOH and THF, shown in fig. 1.13, resemble each other strongly. Differences in the shape of the carbon K-edge of iPrOH and MeOH can be linked to the large sample thickness and the low jump ratio, which both decrease the quality of the obtained information, resulting in an overall noisy signal.

Though in theory the ratio between sp^2 and sp^3 hybridization of the amorphous carbon can be determined[3,73], the quality of the data obtained for the contaminating solvents does not allow a meaningful quantification. In general, the increased sample thickness due to deposited contamination reduces the signal of EELS features, as seen in the example above, which makes quantification of the sample's element composition and determination of the elements' oxidation states more challenging[79]. The impact of an increased sample thickness, which leads to plural scattering events is further discussed in section 1.4.

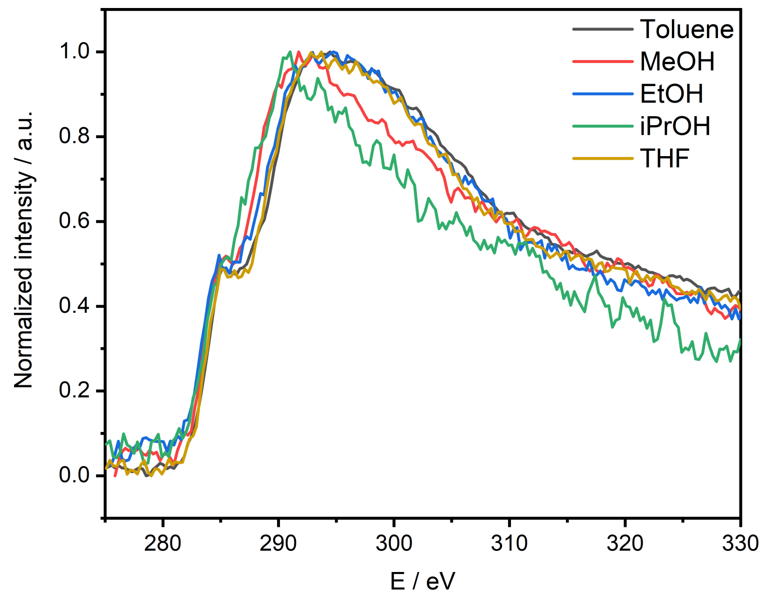

Figure 1.13: Normalized carbon K-edge EEL spectra of contamination resulting from different solvents.

Another application, in which carbon contamination reduces the quality of the obtained data is integrated differential phase contrast (iDPC). When analyzing a sample in STEM mode, the electrostatic potential can be measured, as the deflected electrons are collected by a segmented dark-field detector. Integrating the obtained vector field image results in a scalar image of the intensity of the electrostatic potential caused by the investigated specimen in which the intensity shows nearly proportional behavior with the atomic number of the sample[90]. Therefore, using iDPC, light elements can be analyzed far better, allowing to even investigate lithium[60] and hydrogen atoms[12]. For comparison, the contrast in HAADF images increases with the square of the atomic number of the sample, making HAADF a good method for displaying elements with a high atomic number, while lighter elements appear at lower contrast. The downside of iDPC is that carbon contamination strongly affects such measurements as the light carbon atoms can be displayed very prominently by this technique. Moreover, the increased sample thickness caused by the contamination impairs the achievable contrast[60].

Over time, many mitigation methods have been developed to tackle the problem of carbon contamination. Depending on the procedure, some techniques can be applied before the sample gets inserted, while others rely on cleaning of the sample within the microscope.

One of the most commonly applied methods is plasma cleaning: Atoms of a suitable gas or gas mixture are ionized by a high frequency electromagnetic field. The resulting ions react with contaminant atoms and break these down to species that can be removed by the vacuum. A plasma created from synthetic air (80% N_2 / 20% O_2) has mainly oxidizing characteristics, while the cleaning mechanism of an argon plasma relies on sputtering effects[2,26,68]. Plasma cleaning shows excellent results even after short cleaning times[15,48,49], though sample-thinning effects must not be neglected[67,89].

An alternative to plasma cleaning is ozone cleaning. Here, in a low vacuum environment, the specimen is illuminated with ultraviolet light with wavelengths of 184.9 nm and 253.7 nm. At the wavelength of 184.9 nm, the formation of ozone (*O_3) from O_2 molecules is most effective, while light with a wavelength of 253.7 nm photosensitizes hydrocarbon contamination[25] and additionally decomposes ozone to molecular oxygen and atomic oxygen, which then reacts as a strong oxidation agent with contaminants[34,84]. The volatile reaction products include H_2O and CO_2, which can be removed by the vacuum[77].

Heating the sample can also be utilized for mitigating carbon contamination. The sample can either be heated before being inserted into the microscope, or by a designated heating holder. It is important to note that not all specimens are suitable for this method. Heating can lead to morphological changes[83] and one has to consider that outgassing in the TEM vacuum can impact the sample environment or even lead to reactions with the TEM grid[92]. When heating a sample outside of the microscope, undesired oxidation by air can alter the sample. Heating has become an established method for carbon mitigation, though it has not been proven to be successful for all applications[11].

With the sample in the microscope, beam showering the specimen offers a strategy for contamination mitigation. By illuminating a large area of the grid (in TEM mode) or

by scanning at a low magnification (in STEM mode), hydrocarbons can be reduced to amorphous carbon and, as a result, diffusion towards areas to be investigated at high magnifications can be reduced [21].

Cooling the specimen also offers the possibility to decrease carbon accumulation during TEM investigations. By cooling either the specimen directly or utilizing a cryo shield in the immediate vicinity of the sample, hydrocarbons get immobilized and therefore diffusion towards the electron beam gets reduced [43,44]. The specimen needs to be cooled during the whole measurement procedure as at increasing temperatures contaminants desorb and impair the experiments. Water adsorption, e.g., on the sample holder, is another problem that needs to be considered when performing measurements at low temperatures, as the formation of ice can obstruct the view [45,46]. Overall, it is difficult to achieve stable conditions without thermal drifts during the measurements. In many cases, the technical requirements for cooling a sample exceed the benefits of this procedure, so other mitigation strategies might be preferable.

Other approaches for reducing contamination that have been given little attention include washing the sample with activated charcoal and organic solvent [58], etching by the electron beam in a low-pressure oxidizing environment [57] or baking with activated charcoal [1]. These methods have been tested in a very limited range of applications and therefore might not prevail.

1.3 Removal of residual molecules from a vacuum system

Despite the availability of many possible contamination mitigation strategies for TEM experiments, the removal of residual contaminant molecules from a vacuum setup is crucial for obtaining high-quality data. This issue not only affects electron microscopy experiments, but also many other scientific investigations that require a low pressure for

performing well in their designated scope.

For a better understanding of the processes involved in contaminant removal in a vacuum, a few considerations need to be taken into account: The mean free path, $\bar{l}$, of a molecule is the average distance a particle moves between interactions with another particle and is given by eq. (1.1).

$$\bar{l} = \frac{k \cdot T}{\sqrt{2} \cdot \pi \cdot {d_m}^2 \cdot p} \tag{1.1}$$

Here, k is the Boltzmann constant, T the temperature, d_m the molecule's diameter and p the pressure. The mean free path is very short at ambient pressure, as the high density of molecules results in many collisions, and increases with a lower pressure.

In electron microscopy, the pressure in the sample environment extends over many orders of magnitude and is very different for TEM (approximately 10^{-7} mbar), compared to ETEM (up to 100 mbar[54]) experiments. Spatial limitations, i.e., the small gap between the pole pieces in the octagon, need to be considered in experiments regarding the removal of accumulated contaminants.

Given that an N_2 molecule has a diameter of $374 \cdot 10^{-12}$ m[51], a value for $\bar{l} \cdot p$ of $6.51 \cdot 10^{-5}$ m · mbar can be calculated based on eq. (1.1) for a temperature of 20 °C. Accordingly, the mean free path for such a molecule is approximately $6.5 \cdot 10^{-6}$ m at ETEM conditions (10 mbar), while at a TEM pressure of 10^{-7} mbar, the mean free path is about 651 m.

The flow regime of particles through an orifice in a vacuum environment depends on the mean free path $\bar{l}$ and the diameter of the restriction d_s and is described by the Knudsen number in eq. (1.2)[51].

$$K_n = \frac{\bar{l}}{d_s} \tag{1.2}$$

For $K_n < 0.01$, gas molecules are in a state of viscous flow and interact with each other significantly more often than with surfaces in the vacuum vessel due to their short mean free path. If $K_n > 0.5$, a free molecular flow is attained, in which molecules hit surfaces in

the vacuum chamber and recoil, changing their direction, while collisions between different gas molecules virtually do not occur anymore. Between these flow regimes, a Knudsen flow can be assumed which represents a transition between the two aforementioned behaviours of the gas molecules[51].

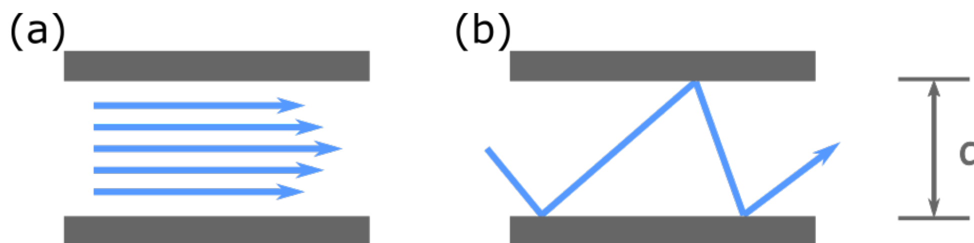

Figure 1.14: Different flow regimes of particles in a vacuum, (a) viscous flow ($K_n < 0.01$), (b) molecular flow ($K_n > 0.5$).

Spatial restrictions in the immediate environment of a sample in the octagon indicate that, while the pressure is in the range prevalent in an ETEM, a viscous flow of particles is likely, while at TEM pressure the particles move in a free molecular flow. This allows for the assumption that contaminants in the gas phase can get removed easier at ETEM pressures regime than in the TEM pressure regime.

When a sample is introduced into the vacuum in the microscope, different processes modify its closest surroundings. A significant contribution comes from molecules outgassing from the sample. These might either be solvent residues from the synthesis or preparation, or sample components, e.g., ligands. Apart from outgassing of VOCs, gas-borne molecules can also adsorb and subsequently desorb from the pole pieces and other surfaces in the TEM. By employing a liquid nitrogen cold trap, a part of the residual contaminants is adsorbed as long as the device is kept at low temperatures. Additional factors contributing to the pressure are permeation and leaks, though their contribution should be relatively small in a TEM system in operation.

Cleaning TEM samples by vacuum is discussed in chapter 4. Therefore, a designated

setup for preparing the specimens is pumped from ambient pressure to the range of approximately 10^{-8} mbar. This process comprises different physical processes of molecular removal that are displayed in fig. 1.15, which shows the dependence of the pressure, p, on the pumping time, t[29]. First, the gas volume is removed with a turbomolecular pump, which, dependent on the pumping speed, happens in a matter of seconds as the pressure decreases exponentially with time. After this, the pressure reduction in the setup is mostly determined by surface desorption processes proportional to t^{-1}. The pressure decrease not only depends on molecules adsorbed to the surfaces within the setup, but also on VOCs originating from the sample. For our setup, is was observed that this step takes up to 10 h, though its duration strongly varies, depending on the sample. At very low pressures, the pressure decrease is mostly limited by diffusion processes that have a time dependence which is proportional to $t^{-\frac{1}{2}}$, e.g., through elastomer sealings. The final pressure depends on permeation processes that establish a constant pressure value. These two processes cannot be avoided in our setup and co-determine the final pressure reached after extended pumping[29].

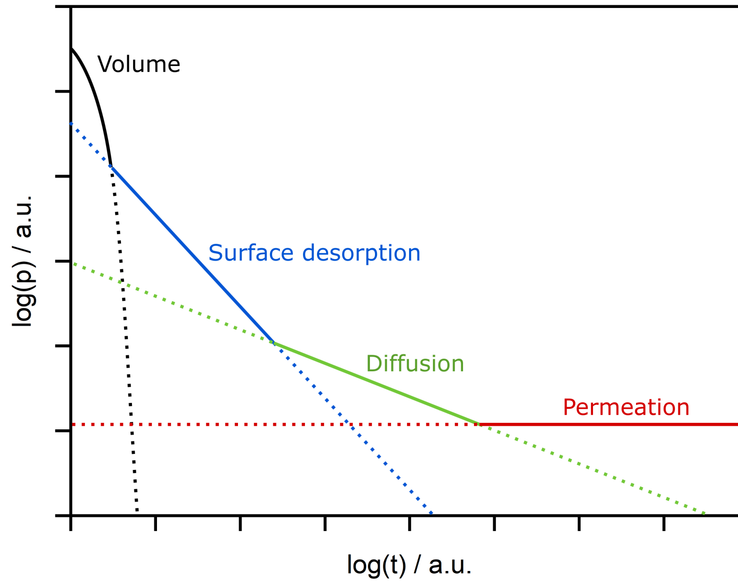

Figure 1.15: Schematic overview of physical processes that influence the pressure when pumping a setup from ambient to low pressure.

Damage by ionizing radiation, such as that caused by the electron beam, is not limited to carbon contamination on TEM samples. Radiation effects also require consideration when measuring the pressure. For the pressure measurements in all applications discussed in this work one needs to consider that the actual pressure might differ from that detected by the pressure gauges for several reasons: For all pressure measurements, a combined Pirani/cold-cathode combination gauge was utilized. The Pirani component is responsible for determining the pressure in a range between 10^{-2} mbar up to atmospheric pressure. Its main components are a tungsten wire that is heated to a temperature between 110 °C and 130 °C and a Wheatstone bridge. Due to the thermal conductivity of the gas molecules surrounding the wire, the walls of its encasing are consequently heated as well. In order to maintain the wire's temperature, a certain voltage needs to be applied to the Wheatstone bridge, which is dependent on the pressure[32]. A significant disadvantage of this measurement principle is its dependence on the residual gas in the vacuum chamber as the thermal conductivity strongly depends on its composition. As the gauge's pressure

reading is calibrated for one gas, which is usually nitrogen, the true value might differ from the displayed pressure value if a different gas is measured. The value can be adjusted by a correction factor, which shows a linear behavior with pressure up to 10 mbar for most gases and at higher values deviates from this trend. In particular, if a high amount of hydrocarbon contaminants contributes to changes in the gas composition, the displayed pressure might significantly differ from the the actual value [7,32].

In the vacuum range between 10^{-9} mbar to 10^{-3} mbar, the pressure is measured by an inverted magnetron cold-cathode ionization gauge [86]. The measurement principle is based on a high voltage applied between a cathode and an anode, which results in electrons being ejected from the cathode by field emission. These electrons can ionize residual gas molecules, resulting in a discharge current that is pressure dependent. In addition, a magnet is located on the outside of the gauge, resulting in spiral trajectory of the electrons emitted from the cathode, which increases their time of flight and therefore the probability of ionization events. In general, the long-term stability of these gauges is decreased by sputtering of the cathode material and ionization process of residual hydrocarbon components, resulting in the deposition of insulating carbonaceous material on the electrodes [75,85]. Especially the high amounts of contaminants investigated in this work impair the accuracy and sensitivity of the gauges, often resulting in pressure readings lower than the actual pressure [87].

How well gas molecules can be removed in a vacuum system is described by the conductance, C. The conductance between two components can be determined by considering the volumetric flow rate, q_{Vp}, and the pressure difference at the two ends of the component, Δp [51]:

$$C = \frac{q_{Vp}}{\Delta p} \tag{1.3}$$

The corresponding volumetric flow rate depends on the dimensions of the orifice between these two components and is related to the cross-section of the orifice, A, the mean thermal

velocity of a molecule, $\bar{c}$, and the pressure difference, Δp[51]:

$$q_{Vp} = A \cdot \frac{\bar{c}}{4} \cdot \Delta p \tag{1.4}$$

To ascertain a high volumetric flow rate, and therefore to allow successful contaminant removal, the SCS discussed in section 4 has a linear setup geometry with large flanges that have the same diameters as the sample chamber; here mainly the baffle cooler contributes to a reduction of the conductance, resulting in an overall large conduction value. For comparison, the octagon setup design discussed in section 2 comprises a pumping system adapted from a transmission electron microscope. The components are pumped through flexible corrugated hoses with small diameters and with further restrictions determined by orifices, valves and many bended flanges and hoses. Though determining the conductance of a setup is not trivial, rough estimations of this value allow for the assumption that in the SCS, the conductance is of order 10^1 L/s, while for the octagon setup it is in the range of 10^{-3} to 10^{-2} L/s, which makes the removal of gas molecules far more tedious.

The emphasis of this work is on the impact of contaminants on electron microscopy experiments. In a TEM environment, a high vacuum is required for investigations using the electron beam. The layout of the microscope is optimized to obtain high-quality data. At the same time, the vacuum system is not designed for contaminant removal due to many components, e.g., orifices for adjusting the pressure to different values, or corrugated hoses for minimizing vibrations when the microscope is in use. These spatial restrictions hinder the removal of contaminants and decrease the conductance of a setup. Therefore, for contaminant removal, a large vacuum chamber in close proximity to the vacuum pump should be used instead.

1.4 Thickness measurements in TEM

In order to quantify the accumulated contamination, EELS measurements were conducted. Different measurements for calculating the relative thickness of samples have been discussed in the literature[47,62]. The evaluation of thickness measurements is based on the log-ratio method[62] described by eq. (1.5): The thickness of the sample, d, is a function of its inelastic mean free path, λ, the intensity of the zero loss peak, I_0, and the total intensity, I_t, of the EEL spectra[18].

$$\frac{d}{\lambda} = \ln \frac{I_t}{I_0} \tag{1.5}$$

The log-ratio method only yields the relative thickness and requires a value for the inelastic mean free path in order to obtain absolute thickness values. The inelastic mean free path depends on several factors, e.g., the acceleration voltage, collection and convergence angles, and the local sample characteristics, e.g., the composition, density or degree of structural order, and therefore can only be determined approximately.

The composition of the contamination was determined by EDX analysis. It was found that, regardless of the investigated solvent, the contamination after beam exposure consisted of at least 95% of carbon with traces of predominantly nitrogen and oxygen. This method is not suitable for the quantification of hydrogen due to this element's lack of characteristic X-ray emission[31].

The inelastic mean free path for certain sample compositions was determined with the GMS DigitalMicrograph plugin "Mean Free Path Estimator" by Dave Mitchell[65]. Values for λ obtained by this method are listed in table 1.4 for an acceleration voltage of 200 kV and a collection semi-angle of 41 mrad; note that the values are in a similar range for all considered compositions due to similar atomic numbers of the elements.

Composition	Inelastic mean free path / nm
100% Carbon	128.6
95% Carbon / 5% Nitrogen	128.3
95% Carbon / 5% Oxygen	127.9

Table 1.4: Estimations of the inelastic mean free path depending on the local sample composition at 200 kV and a collection semi-angle of 41 mrad [65].

Since carbon strongly dominates the composition, for further calculations using the inelastic mean free path for the thickness evaluations we adopt the value of 128.6 nm.

One requirement for thickness calculations based on this method is that the ratio of the thickness to the inelastic mean free path must be smaller than 5 ($t/\lambda < 5$) [18]. Otherwise the zero-loss peak lacks the necessary intensity compared to the rest of the EEL spectrum for quantification because the high sample thickness results in a broad range of elastic and inelastic scattering events. An example is shown in fig. 1.16: A sample of toluene was dried for either 30 min (a) or 10 min (b) before being exposed to the electron beam for 180 s. For the sample that was dried for a longer time, the zero loss signal has a significantly higher intensity compared to the rest of the spectrum, making a quantification with eq. (1.5) possible. For the sample dried for only 10 min, the zero loss peak only contributes a minor fraction to the total spectrum intensity, making a thickness determination prohibitive. The energy losses resulting from these plural scattering events form a Landau distribution with the maximum shifted towards higher energies with increasing sample thickness [18]. Overall, EELS thickness measurements are assumed to have an error of around 10% due to multiple approximations made during the calculation process [18].

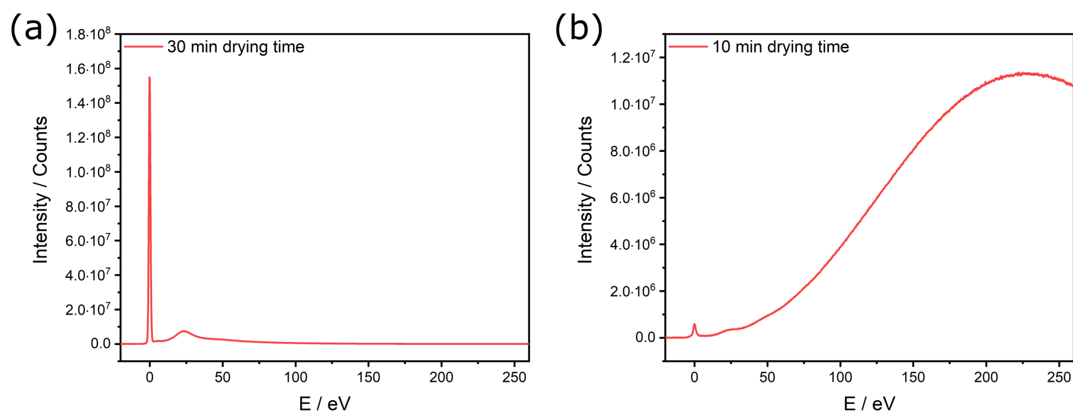

Figure 1.16: EEL spectra of toluene samples dried for (a) 30 min or (b) 10 min before being exposed to the electron beam for 180 s.

1.5 Proton-transfer-reaction mass spectrometry

For investigating carbon contamination under ETEM conditions, proton-transfer-reaction (PTR) mass spectrometry (MS) is utilized. This method is based on transferring a positive charge from protonated water molecules (H_3O^+) to VOCs in a reaction drift tube and then characterizing the protonated VOCs with a time-of-flight mass spectrometer. All measurements were carried out with a Ionicon PTR-TOF-1000 system. The proton transfer to an organic component R can be described by eq. (1.6)[33].

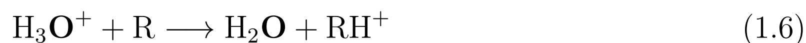

$$H_3\mathbf{O}^+ + R \longrightarrow H_2\mathbf{O} + RH^+ \tag{1.6}$$

Accordingly, this method is selective for components with a higher proton affinity than water (>165 kcal/mol)[59]. This allows for analyzing many hydrocarbon compounds with a low fragmentation of VOCs due to their soft ionization properties, while not ionising, e.g., molecules from air components.

The working principle of a PTR time-of-flight (TOF) mass spectrometer is illustrated in fig. 1.17[50].

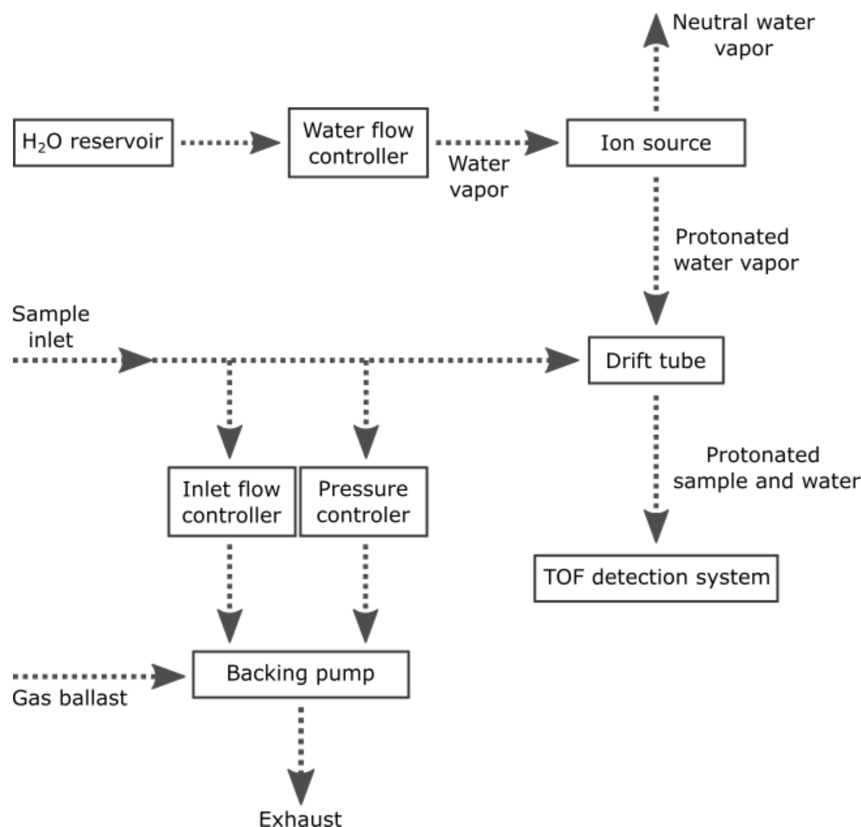

Figure 1.17: Gas flow scheme of a PTR TOF mass spectrometer.

The sample needs to enter the drift tube at a defined pressure while at the same time any mass flow or pressure regulating devices must be avoided, as these would distort the time-resolution and quantification of the VOCs. Therefore, the sample inlet flow is reduced by a back-pressure controlling system consisting of an inlet mass flow controller and a pressure controller that adjust the sample flow towards the drift tube.

The amount of water vapor entering the ion source is also adjusted by a mass flow controller. In the ion source, part of the water is protonated and enters the drift tube, while the residual neutral water vapor is removed. In the drift tube, the protonated water ionizes the sample molecules, and the sample ions are accelerated by an electric drift field towards the TOF detection system. In the TOF detector, the ions get extracted by an electric pulse with the electric energy E_{el}, which is the product of elementary charge e and

the acceleration voltage U and equal to the kinetic energy E_{kin} of the ion, which depends on the molecular mass m, and the ion velocity v (eq. (1.7)).

$$e \cdot U = \frac{m \cdot v^2}{2} \tag{1.7}$$

The time of flight t_f of an ion depends on the length of the flight path, s, and the velocity, v, which, by inserting eq. (1.7), is given by eq. (1.8).

$$t_f = \frac{s}{v} = s \cdot \sqrt{\frac{m}{2 \cdot e \cdot U}} \tag{1.8}$$

The ions are detected depending on the time of flight they require to reach the detector, which allows for measuring a complete spectrum for every electric pulse. The ions' path of flight is increased by a reflector with an electric field in the opposite direction of the their movement, deflecting them towards the detection unit. As a consequence, the ions travel farther though the detector system, which makes a better mass separation possible[6].

To achieve corrected time traces of a molecule, the measured PTR MS raw data requires processing (see fig. 1.18).

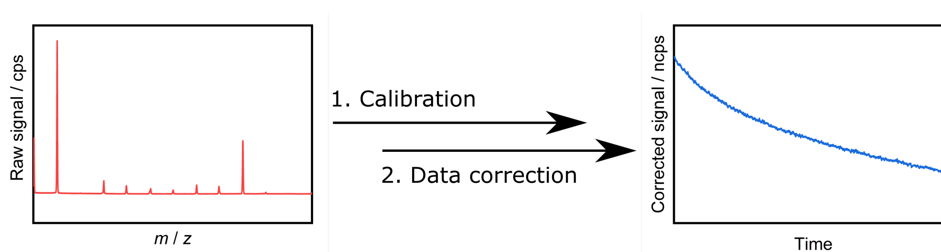

Figure 1.18: Schematic overview of the steps required for achieving corrected time traces out of PTR MS raw data.

First, the acquired data needs to be calibrated. For this, different molecules can be selected: Among these are different water species, i.e., protonated water $H_3{}^{18}O^+$ with m/z 21.022 or hydronium dimers $H_2O\text{-}H_3O^+$ with m/z 37.029 that are formed during the ionization process and at the low end of the m/z scale. Also other distinctive calibration

molecules can be produced by the ion source, e.g., NO^+ with m/z 29.997, or protonated acetone ($C_3H_7O^+$) with m/z 57.049. Additional calibration points at the higher end of the m/z scale were added by a Ionicon PerMaSCal unit, which introduces $C_6H_4I_2$ molecules with m/z 330.848 and an associated fragment with m/z 203.943 with H_3O^+ as a ionization agent. These calibration points ensure that the wide mass range required for the investigated VOCs is covered.

Obtained data was corrected for the instrumental transmission, fragmentation and the isotopic ratio of the species. In addition, the ion count rate was normalized to a primary ion signal intensity of 10^6 counts per second. The signal of an investigated hydrocarbon species (HC) is therefore given in normalized counts per second *ncps* by eq. (1.9).

$$[\mathrm{HC}]_{ncps} = \frac{[\mathrm{HC}^+_{corr}]}{[\mathrm{H_3}^{18}\mathrm{O^+}_{corr}]} \cdot 10^6 \tag{1.9}$$

For our PTR MS system, calibration measurements have shown that the resolution limit is reached at corrected intensities of 10 ncps, though the detection limit is even lower. The upper detection limit is constrained by oversaturation of the detector, as only one ion can be detected per time bin. It is exceeded, e.g., for the primary ion signal of H_3O^+ during the measurements.

1.6 Outline of this thesis

As carbon contamination is an issue in the field of electron microscopy, this work focuses on the analysis of such contamination in different TEM settings. Since many samples at our research institute are either synthesized or need to be dispersed in organic solvents for applying them to the TEM grid, the theme of my work is the impact that solvents typically used in chemical synthesis and/or by microscopists have on TEM experiments.

In chapter 2, the accumulation of different solvent residues on a decommissioned octagon was studied under ETEM conditions and analyzed by PTR MS. The temporal evolution

of the quantity of outgassing solvent molecules is followed after a freshly prepared sample is inserted in the setup. In addition, it is investigated how the gas composition under ETEM conditions changes over time after the sample holder is removed and while the octagon is brought to a typical operational TEM pressure range in between measurements. As plasma cleaning has been an established method for the removal of hydrocarbons, the impact of this cleaning procedure on solvent residues was studied as well to gain insight in how persistent the contamination may be in an octagon. For these studies, three selected solvents, THF, toluene and mesitylene, were investigated as these are commonly used in chemical synthesis. Overall, these experiments give insight in how sample outgassing affects the sample environment in the octagon and help to gain knowledge about time frames over which solvents from the sample preparation alter the gas composition in ETEM experiments.

Based on the results from the octagon studies, experiments were extended to measurements in the TEM and are discussed in chapter 3. Amorphous carbon contamination caused by electron beam exposure was analyzed for TEM grids prepared with different organic solvents. Here, the investigated solvents were selected based on their usage in chemical synthesis, i.e., THF and toluene, and microscopists' preferences for sample preparation, i.e., methanol, ethanol and isopropanol. Accumulated contamination depending on the beam exposure time was quantified by EELS thickness measurements for the different solvents. In these studies, the impact of the sample's drying time before insertion into the TEM and the influence of the TEM vacuum when samples remain for an extended time in the microscope was analyzed. Also, insight was gained on the impact that its water content has on solvent quality.

While in chapter 3, the focus was on contamination from different solvents, the choice of a solvent is often restricted by the sample's properties and should not be modified. Therefore, in chapter 4, the impact of different strategies for mitigating contamination is studied. Here, different contamination mitigation strategies are compared, namely plasma cleaning, ozone cleaning, heating of the sample and beam showering the sample. While

there are several established cleaning methods for TEM samples, all of these come with their own advantages and disadvantages. As an alternative strategy, the novel approach of vacuum removal of VOCs by a designated sample cleaning station (SCS) is discussed and is suggested as an alternative approach for customized sample preparation tailored to the sample's characteristics. With EELS thickness measurements, these methods were compared regarding their impact on the total amount of accumulated carbonaceous material, the thickness in the inner of the area exposed to the electron beam and the structural integrity of the carbon film of the grid. In addition, the impact of sample pretreatment by the SCS was studied for the examples of CoP and MoP nanoparticle samples, some of which were additionally stabilized by supported ionic liquid phase.

Final conclusions and an outlook are presented in chapter 5.

References

[1] Algara-Siller, G., Lehtinen, O., Turchanin, A., Kaiser, U., 2014. Dry-cleaning of graphene. Applied Physics Letters 104. doi:10.1063/1.4871997.

[2] Baker, M., 1980. Plasma cleaning and the removal of carbon from metal surfaces. Thin Solid Films 69, 359–368. doi:10.1016/0040-6090(80)90588-X.

[3] Berger, S.D., McKenzie, D.R., Martin, P.J., 1988. EELS analysis of vacuum arc-deposited diamond-like films. Philosophical Magazine Letters 57, 285–290. doi:10.1080/09500838808214715.

[4] Bhattacharyya, S., Lübbe, M., Bressler, P.R., Zahn, D.R., Richter, F., 2002. Structure of nitrogenated amorphous carbon films from NEXAFS. Diamond and Related Materials 11, 8–15. doi:10.1016/S0925-9635(01)00525-8.

[5] Boles, M., Ling, D., Hyeon, T., Talapin, D., 2016. The surface science of nanocrystals. Nature Materials 15, 141–153. doi:10.1038/nmat4578.

[6] Cappellin, L., Biasioli, F., Fabris, A., Schuhfried, E., Soukoulis, C., Märk, T.D., Gasperi, F., 2010. Improved mass accuracy in PTR-TOF-MS: Another step towards better compound identification in PTR-MS. International Journal of Mass Spectrometry 290, 60–63. doi:10.1016/j.ijms.2009.11.007.

[7] Carmichael, L.T., Sage, B.H., 1966. Viscosity and Thermal Conductivity of Nitrogen-n-Heptane and Nitrogen-n-Octane Mixtures. AIChE Journal 12, 559–562. doi:10.1002/aic.690120330.

[8] Chen, H., Li, K., Yang, M., Zhang, Z.and Kong, Y., Lu, Q., Du, Y., 2019. Effect of electron beam irradiation in TEM on the microstructure and composition of nano-precipitates in Al-Mg-Si alloys. Micron 116, 116–123. doi:10.1016/j.micron.2018.10.003.

[9] Creemer, J.F., Helveg, S., Hoveling, G.H., Ullmann, S., Molenbroek, A.M., Sarro, P.M., Zandbergen, H.W., 2008. Atomic-scale electron microscopy at ambient pressure. Ultramicroscopy 108, 993–998. doi:10.1016/j.ultramic.2008.04.014.

[10] Curtis, G.H., Ferrier, R.P., 1969. The electric charging of electron-microscope speci-

mens. Journal of Physics D: Applied Physics 2, 1035–1040. doi:10.1088/0022-3727/2/7/312.

[11] Danev, R., Glaeser, R.M., Nagayama, K., 2009. Practical factors affecting the performance of a thin-film phase plate for transmission electron microscopy. Ultramicroscopy 109, 312–325. doi:10.1016/j.ultramic.2008.12.006.

[12] De Graaf, S., Momand, J., Mitterbauer, C., Lazar, S., Kooi, B., 2020. Resolving hydrogen atoms at metal-metal hydride interfaces. Science Advances 6, 1–9. doi:10.1126/sciadv.aay4312.

[13] De Jonge, N., Ross, F.M., 2011. Electron microscopy of specimens in liquid. Nature Nanotechnology 6, 695–704. doi:10.1038/nnano.2011.161.

[14] De Jonge, N., Verch, A., Demers, H., 2018. The Influence of Beam Broadening on the Spatial Resolution of Annular Dark Field Scanning Transmission Electron Microscopy. Microscopy and Microanalysis 24, 8–15. doi:10.1017/S1431927618000077.

[15] Dickey, E.C., Dravid, V.P., Nellist, P.D., Wallis, D.J., Pennycook, S.J., Revcolevschi, A., 1997. Structure and bonding at Ni-ZrO2 (cubic) interfaces formed by the reduction of a NiO-ZrO2 (cubic) composite. Microscopy and Microanalysis 3, 443–450. doi:10.1017/S1431927697970343.

[16] Drees, H., Müller, E., Dries, M., Gerthsen, D., 2018. Electron-beam broadening in amorphous carbon films in low-energy scanning transmission electron microscopy. Ultramicroscopy 185, 65–71. doi:10.1016/j.ultramic.2017.11.005.

[17] Egerton, R.F., 2009. Electron energy-loss spectroscopy in the TEM. Reports on Progress in Physics 72. doi:10.1088/0034-4885/72/1/016502.

[18] Egerton, R.F., 2011. Electron Energy-Loss Spectroscopy in the Electron Microscope. 3rd ed., Springer US, New York. doi:10.1007/978-1-4419-9583-4.

[19] Egerton, R.F., 2012. Mechanisms of radiation damage in beam-sensitive specimens, for TEM accelerating voltages between 10 and 300 kV. Microscopy Research and Technique 75, 1550–1556. doi:10.1002/jemt.22099.

[20] Egerton, R.F., 2013. Control of radiation damage in the TEM. Ultramicroscopy 127,

100–108. doi:10.1016/j.ultramic.2012.07.006.

[21] Egerton, R.F., Li, P., Malac, M., 2004. Radiation damage in the TEM and SEM. Micron 35, 399–409. doi:10.1016/j.micron.2004.02.003.

[22] Egerton, R.F., McLeod, R., Wang, F., Malac, M., 2010. Basic questions related to electron-induced sputtering in the TEM. Ultramicroscopy 110, 991–997. doi:10.1016/j.ultramic.2009.11.003.

[23] Ennos, A.E., 1953. The origin of specimen contamination in the electron microscope. British Journal of Applied Physics 4, 101–106. doi:10.1088/0508-3443/4/4/302.

[24] Ennos, A.E., 1954. The sources of electron-induced contamination in kinetic vacuum systems. British Journal of Applied Physics 5, 27–31. doi:10.1088/0508-3443/5/1/307.

[25] Fikhtengol, V.S., Zolotareva, R.V., L'vov, Y.A., 1966. Ultraviolet Spectra of Elastomers and Rubber Chemicals. 1st ed., Plenum Press Data Division, New York. doi:10.1007/978-1-4615-9591-5.

[26] Fischione, P.E., 1997. Plasma processing system for transmission electron microscopy specimens and specimen holders , Patent No. 5,633,502.

[27] Funk, H., Shargaieva, O., Eljarrat, A., Unger, E.L., Koch, C.T., Abou-Ras, D., 2020. In Situ TEM Monitoring of Phase-Segregation in Inorganic Mixed Halide Perovskite. Journal of Physical Chemistry Letters 11, 4945–4950. doi:10.1021/acs.jpclett.0c01296.

[28] Galvan, D., Pei, Y.T., De Hosson, J.T.M., Cavaleiro, A., 2005. Determination of the sp3 C content of a-C films through EELS analysis in the TEM. Surface and Coatings Technology 200, 739–743. doi:10.1016/j.surfcoat.2005.02.071.

[29] Gatzen, H.H., Saile, V., Leuthold, J., 2005. Micro- and Nanofabrication. 1st ed., Springer-Verlag Berlin Heidelberg. doi:10.1201/9781420028270.ch1.

[30] Goh, Y.M., Schwartz, J., Rennich, E., Ma, T., Kerns, B., Hovden, R., 2020. Contamination of TEM Holders Quantified and Mitigated with the Open-Hardware, High-Vacuum Bakeout System. Microscopy and Microanalysis 26, 906–912. doi:10.1017/

S1431927620001762.

[31] Goldstein, J.I., Newbury, D.E., Michael, J.R., Ritchie, N.W.M., Scott, J.H.J., Joy, D.C., 2017. Scanning Electron Microscopy and X-Ray Microanalysis. 4th ed., Springer New York. doi:10.1007/978-1-4939-6676-9.

[32] Grinham, R., Chew, A., 2017. Gas Correction Factors for Vacuum Pressure Gauges: Factors Affecting the Sensitivity of Ionisation and Thermal Type Vacuum Gauges with Different Gases. Vakuum in Forschung und Praxis 29, 25–30. doi:10.1002/vipr.201700640.

[33] Hansel, A., Jordan, A., Holzinger, R., Prazeller, P., Vogel, W., Lindinger, W., 1995. Proton transfer reaction mass spectrometry: on-line trace gas analysis at the ppb level. International Journal of Mass Spectrometry and Ion Processes 149/150, 609–619. doi:10.1016/0168-1176(95)04294-U.

[34] Hansen, R.W.C., Bissen, M., Wallace, D., Wolske, J., Miller, T., 1993. Ultraviolet / ozone cleaning of carbon-contaminated optics. Applied Optics 32, 4114–4116. doi:10.1364/AO.32.004114.

[35] Hansen, T.W., Wagner, J.B. (Eds.), 2016. Controlled Atmosphere Transmission Electron Microscopy. Springer Cham. doi:10.1007/978-3-319-22988-1.

[36] Harris, P.J.F., 2001. Carbonaceous contaminants on support films for transmission electron microscopy. Carbon 39, 909–913. doi:10.1016/S0008-6223(00)00195-0.

[37] Hart, R.K., Kassner, T.F., Maurin, J.K., 1970. The contamination of surfaces during high-energy electron irradiation. Philosophical Magazine 21, 453–467. doi:10.1080/14786437008238431.

[38] Häusler, I., Kamachali, R.D., Hetaba, W., Skrotzki, B., 2018. Thickening of T 1 precipitates during aging of a high purity Al-4Cu-1Li-0.25Mn alloy. Materials 12. doi:10.3390/ma12010030.

[39] Hawkes, P.W., Spence, J.C.H. (Eds.), 2019. Springer Handbook of Microscopy. 1st ed., Springer, Cham. doi:10.1007/978-3-030-00069-1.

[40] Heide, H.G., 1960. Die Objektverschmutzung und ihre Verhütung, Springer Berlin

Heidelberg. pp. 87–90. doi:10.1007/978-3-642-50195-1_28.

[41] Hettler, S., Onoda, J., Wolkow, R., Pitters, J., Malac, M., 2019. Charging of electron beam irradiated amorphous carbon thin films at liquid nitrogen temperature. Ultramicroscopy 196, 161–166. doi:10.1016/j.ultramic.2018.10.010.

[42] Heuer-Jungemann, A., Feliu, N., Bakaimi, I., Hamaly, M., Alkilany, A., Chakraborty, I., Masood, A., Casula, M.F., Kostopoulou, A., Oh, E., Susumu, K., Stewart, M.H., Medintz, I.L., Stratakis, E., Parak, W.J., Kanaras, A.G., 2019. The role of ligands in the chemical synthesis and applications of inorganic nanoparticles. Chemical Reviews 119, 4819–4880. doi:10.1021/acs.chemrev.8b00733.

[43] Hirsch, P., Kässens, M., Püttmann, M., Reimer, L., 1994. Contamination in a scanning electron microscope and the influence of specimen cooling. Scanning 16, 101–110. doi:10.1002/sca.4950160207.

[44] Hren, J.J., 1978. Specimen Contamination in Analytical Electron Microscopy: Sources and Solutions. Ultramicroscopy 3, 375–380. doi:10.1016/S0304-3991(78)80057-6.

[45] Hren, J.J., Goldstein, J.I., Joy, D.C., 1979. Introduction to Analytical Electron Microscopy. Springer New York, New York. doi:10.1007/978-1-4757-5581-7.

[46] Hurbain, I., Sachse, M., 2011. The future is cold: cryo-preparation methods for transmission electron microscopy of cells. Biology of the Cell 103, 405–420. doi:10.1042/bc20110015.

[47] Iakoubovskii, K., Mitsuishi, K., Nakayama, Y., Furuya, K., 2008. Thickness measurements with electron energy loss spectroscopy. Microscopy Research and Technique 71, 626–631. doi:10.1002/jemt.20597.

[48] Isabell, T.C., Fischione, P.E., 1998. Applications of Plasma Cleaning for Electron Microscopy of Semiconducting Materials. MRS Proceedings 523, 31–38. doi:10.1557/proc-523-31.

[49] Isabell, T.C., Fischione, P.E., O'Keefe, C., Guruz, M.U., Dravid, V.P., 1999. Plasma cleaning and its applications for electron microscopy. Microscopy and Microanalysis

5, 126–135. doi:10.1017/S1431927699000094.

[50] Jordan, A., Haidacher, S., Hanel, G., Hartungen, E., Märk, L., Seehauser, H., Schottkowsky, R., Sulzer, P., Märk, T.D., 2009. A high resolution and high sensitivity proton-transfer-reaction time-of-flight mass spectrometer (PTR-TOF-MS). International Journal of Mass Spectrometry 286, 122–128. doi:10.1016/j.ijms.2009.07.005.

[51] Jousten, K., 2018. Handbuch Vakuumtechnik. 12th ed., Springer Fachmedien Wiesbaden. doi:10.1007/978-3-658-13386-3.

[52] Knoll, M., Ruska, E., 1932. Das Elektronenmikroskop. Zeitschrift für Physik 78, 318–339. doi:10.1007/BF01342199.

[53] Kong, L., Ji, Z., Xin, H.L., 2022. Electron energy loss spectroscopy database synthesis and automation of core-loss edge recognition by deep-learning neural networks. Scientific Reports 12, 1–12. doi:10.1038/s41598-022-25870-3.

[54] Konings, S.J.P., Kujawa, S., Trompenaars, P.H.F., 2017. Method of studying a sample in an ETEM , Patent No. US 9,658,246 B2.

[55] Kumao, A., Hashimoto, H., Shiraishi, K., 1981. Studies on specimen contamination by transmission electron microscopy. Journal of Electron Microscopy 30, 161–170. doi:10.1093/oxfordjournals.jmicro.a050301.

[56] Lajaunie, L., Pardanaud, C., Martin, C., Puech, P., Hu, C., Biggs, M.J., Arenal, R., 2017. Advanced spectroscopic analyses on a:C-H materials: Revisiting the EELS characterization and its coupling with multi-wavelength Raman spectroscopy. Carbon 112, 149–161. doi:10.1016/j.carbon.2016.10.092.

[57] Leuthner, G.T., Hummel, S., Mangler, C., Pennycook, T.J., Susi, T., Meyer, J.C., Kotakoski, J., 2019. Scanning transmission electron microscopy under controlled low-pressure atmospheres. Ultramicroscopy 203, 76–81. doi:10.1016/j.ultramic.2019.02.002.

[58] Li, C., Pedrazo Tardajos, A., Wang, D., Choukroun, D., Van Daele, K., Breugelmans, T., Bals, S., 2021. A simple method to clean ligand contamination on TEM grids.

Ultramicroscopy 221, 113195. doi:10.1016/j.ultramic.2020.113195.

[59] Lias, S.G., Liebman, J.F., Levin, R.D., 1984. Evaluated Gas Phase Basicities and Proton Affinities of Molecules; Heats of Formation of Protonated Molecules. Journal of Physical and Chemical Reference Data 13, 695–808. doi:10.1063/1.555719.

[60] Lin, Y., Zhou, M., Tai, X., Li, H., Han, X., Yu, J., 2021. Analytical transmission electron microscopy for emerging advanced materials. Matter 4, 2309–2339. doi:10.1016/j.matt.2021.05.005.

[61] Liu, A.C.Y., Arenal, R., Miller, D.J., Chen, X., Johnson, J.A., Eryilmaz, O.L., Erdemir, A., Woodford, J.B., 2007. Structural order in near-frictionless hydrogenated diamondlike carbon films probed at three length scales via transmission electron microscopy. Physical Review B - Condensed Matter and Materials Physics 75, 1–13. doi:10.1103/PhysRevB.75.205402.

[62] Malis, T., Cheng, S.C., Egerton, R.F., 1988. EELS log-ratio technique for specimen-thickness measurement in the TEM. Journal of Electron Microscopy Technique 8, 193–200. doi:10.1002/jemt.1060080206.

[63] Maurice, L., Duval, P., Gorinas, G., 1979. Oil Backstreaming in Turbomolecular and Oil Diffusion Pumps. Journal of Vacuum Science and Technology 16, 741–745. doi:10.1116/1.570073.

[64] McGilvery, C.M., Goode, A.E., Shaffer, M.S.P., McComb, D.W., 2012. Contamination of holey/lacey carbon films in STEM. Micron 43, 450–455. doi:10.1016/j.micron.2011.10.026.

[65] Mitchell, D.R.G., 2006. Determination of mean free path for energy loss and surface oxide film thickness using convergent beam electron diffraction and thickness mapping: A case study using Si and P91 steel. Journal of Microscopy 224, 187–196. doi:10.1111/j.1365-2818.2006.01690.x.

[66] Mitchell, D.R.G., 2015. Contamination mitigation strategies for scanning transmission electron microscopy. Micron 73, 36–46. doi:10.1016/j.micron.2015.03.013.

[67] Noakes, T.C.Q., Valizadeh, R., Hannah, A.N., Jones, L.B., Militsyn, B.L., Mistry,

S., Cropper, M.D., Rossall, A., Van den Berg, J.A., 2022. Oxygen plasma cleaning of copper for photocathode applications: A MEIS and XPS study. Vacuum 205, 111424. doi:10.1016/j.vacuum.2022.111424.

[68] O'Kane, D.F., Mittal, K.L., 1974. Plasma Cleaning of Metal Surfaces. J Vac Sci Technol 11, 567–569. doi:10.1116/1.1318069.

[69] Power, B.D., Crawley, D.J., 1954. Sources, measurement and control of backstreaming. in oil vapour vacuum pumps. Vacuum 4, 415–437. doi:10.1016/0042-207X(54)90003-2.

[70] Reimer, L., 1993. Transmission Electron Microscopy Physics of Image Formation and Microanalysis. 3rd ed., Springer Berlin Heidelberg, Berlin, Heidelberg. doi:10.1007/978-3-662-21556-2.

[71] Reimer, L., Wächter, M., 1978. Contribution to the contamination problem in transmission electron microscopy. Ultramicroscopy 3, 169–174. doi:10.1016/S0304-3991(78)80023-0.

[72] Rengshausen, S., Etscheidt, F., Großkurth, J., Luska, K.L., Bordet, A., Leitner, W., 2019. Catalytic Hydrogenolysis of Substituted Diaryl Ethers by Using Ruthenium Nanoparticles on an Acidic Supported Ionic Liquid Phase (Ru@SILP-SO 3 H). Synlett 30, 405–412. doi:10.1055/s-0037-1611678.

[73] Robertson, J., 2002. Diamond-like amorphous carbon. Materials Science and Engineering: R: Reports 37, 129–281. doi:10.1016/s0927-796x(02)00005-0.

[74] Rykaczewski, K., Marshall, A., White, W.B., Fedorov, A.G., 2008. Dynamic growth of carbon nanopillars and microrings in electron beam induced dissociation of residual hydrocarbons. Ultramicroscopy 108, 989–992. doi:10.1016/j.ultramic.2008.04.006.

[75] Schindler, N., Wilfert, S., 2004. Surface analysis of contamination layers in cold-cathode gauges. Applied Physics A: Materials Science and Processing 78, 691–694. doi:10.1007/s00339-003-2283-5.

[76] Schissel, S.M., Lapin, S.C., Jessop, J.L.P., 2017. Characterization and prediction of

monomer-based dose rate effects in electron-beam polymerization. Radiation Physics and Chemistry 141, 41–49. doi:10.1016/j.radphyschem.2017.05.028.

[77] Soong, C., Woo, P., Hoyle, D., 2012. Contamination Cleaning of TEM/SEM Samples with the ZONE Cleaner. Microscopy Today 20, 44–48. doi:10.1017/s1551929512000752.

[78] Su, D., Zhu, Y., 2010. Scanning moiré fringe imaging by scanning transmission electron microscopy. Ultramicroscopy 110, 229–233. doi:10.1016/j.ultramic.2009.11.015.

[79] Su, D.S., Wang, H.F., Zeitler, E., 1995. The influence of plural scattering on EELS elemental analysis. Ultramicroscopy 59, 181–190. doi:10.1016/0304-3991(95)00027-X.

[80] Tan, H., Verbeeck, J., Abakumov, A., Van Tendeloo, G., 2012. Oxidation state and chemical shift investigation in transition metal oxides by EELS. Ultramicroscopy 116, 24–33. doi:10.1016/j.ultramic.2012.03.002.

[81] Tolbert, B.M., Krinks, M.H., 1960. Chemical Effects of Ionizing Radiation on Pure Organic Compounds. Radiation Research Supplement 2, 586–607. doi:10.2307/3583620.

[82] Tolbert, B.M., Lemmon, R.M., 1955. Radiation Decomposition of Pure Organic Compounds. Radiation Research 3, 52–67. doi:10.2307/3570272.

[83] Tripathi, M., Mittelberger, A., Mustonen, K., Mangler, C., Kotakoski, J., Meyer, J.C., Susi, T., 2017. Cleaning graphene: Comparing heat treatments in air and in vacuum. Physica Status Solidi - Rapid Research Letters 11. doi:10.1002/pssr.201700124.

[84] Vig, J., Le Bus, J., 1976. UV / Ozone of Surfaces. IEEE Transactions on Parts, Hybrids, and Packaging 12, 365–370. doi:10.1116/1.573115.

[85] Wilfert, S., 2003. The contamination effect of cold cathode gauges. Shinku/Journal of the Vacuum Society of Japan 46, 31–37. doi:10.3131/jvsj.46.31.

[86] Wilfert, S., Edelmann, C., 2007. Inverted magnetron manometer with enhanced

operating time. Vacuum 82, 412–419. doi:10.1016/j.vacuum.2007.07.045.

[87] Wilfert, S., Schindler, N., 2004. Investigations of the long-term measuring stability of cold-cathode gauges. Applied Physics A: Materials Science and Processing 78, 663–666. doi:10.1007/s00339-003-2277-3.

[88] Williams, D.B., Carter, C.B., 2009. Transmission Electron Microscopy. 2nd ed., Springer US. doi:10.1007/978-0-387-76501-3.

[89] Wilson, J.A., Craven, A.J., 2003. Improving the analysis of small precipitates in HSLA steels using a plasma cleaner and ELNES. Ultramicroscopy 94, 197–207. doi:10.1016/S0304-3991(02)00265-6.

[90] Yücelen, E., Lazić, I., Bosch, E.G.T., 2018. Phase contrast scanning transmission electron microscopy imaging of light and heavy atoms at the limit of contrast and resolution. Scientific Reports 8, 1–10. doi:10.1038/s41598-018-20377-2.

[91] Zenser, L.P., Gruehn, R., Liebscher, B.H., 2001. Decomposition of MgF2 in the transmission electron microscope. Journal of Solid State Chemistry 157, 30–39. doi:10.1006/jssc.2000.9033.

[92] Zhang, Z., Su, D., 2009. Behaviour of TEM metal grids during in-situ heating experiments. Ultramicroscopy 109, 766–774. doi:10.1016/j.ultramic.2009.01.015.

2 Contamination analysis of the gas composition in environmental transmission electron microscopy

2.1 Abstract

Transmission electron microscopy (TEM) is a fundamental tool for many research fields like catalysis or material research. Many experiments require measurements under environmental TEM (ETEM) conditions, in which an atmosphere of a selected gas is in the close environment of the sample, resulting in a much enhanced pressure in the octagon of the microscope. However, the comparably high pressure in the octagon also influences how long volatile organic components (VOCs), which are often part of the sample itself, remain in the sample environment and can result in carbon contamination during TEM experiments. In our studies, we have analyzed contamination in an ETEM octagon by investigating the impact that different organic solvents have on the sample preparation, but also how tedious the removal of VOCs is once these contaminants are present inside a microscope. With proton-transfer-reaction mass spectrometry (PTR MS), we have quantified the outgassing contamination of samples consisting of THF, toluene or mesitylene depending on their drying time under similar conditions as in an ETEM. We found that high amounts of contaminants adsorb on the inner surfaces of the octagon and we measured how well these VOCs desorb when, after removing the sample, pumping the octagon to typical TEM pressures. For persistent solvents or samples that were not sufficiently dried before insertion, contaminant removal is an extensive process that can be accelerated by plasma cleaning. We have studied the removal of adsorbed contaminants

by applying plasma cleaning to the octagon. Our investigation of residual solvents under ETEM conditions suggests that changes in the sample preparation can improve the residual gas composition in the sample environment.

2.2 Introduction

In-situ TEM experiments are a frequently utilized tool for characterizing a variety of specimens in areas of current research interest like, e.g., catalysis, energy storage materials or life science. Specialized techniques can be used to investigate specimens under conditions met in typical applications. These include offering the possibility to characterize specimens in a well-defined gaseous environment. ETEM allows for the investigation of samples in the presence of a reactive atmosphere down to the atomic scale for a broad range of different applications[37].

One obstacle microscopists are confronted with is the formation of carbon contamination on the sample surface while investigating specimens in electron microscopy. Irradiating the sample with the electron probe may reduce VOCs present in the sample environment. This leads to the deposition of amorphous carbon on the surface, resulting in a loss of image quality and degraded spectroscopic information. In the early days of electron microscopy, vacuum techniques were not advanced enough to prevent the backflow of pumping oils to the microscope, leading to a high concentration of carbon species in the vacuum system[6,7,15]. Nowadays, modern vacuum pumping systems and established cleaning protocols for vacuum chambers allow for a clean vacuum environment[3,11,28]. Nevertheless, due to the limited accessibility of the inner surfaces of an electron microscope, it is especially important to ensure that these surfaces are as clean as possible, as many widely used cleaning techniques are not suitable for TEM. Despite improvements in vacuum engineering, issues with contamination during TEM investigations still occur, though nowadays contamination is often linked to the sample itself[20], e.g., in the form of organic ligands or residual solvents from the synthesis. The sample preparation[18,23]

or the used equipment, e.g., the sample holder [8] or TEM grids [14,27], can also result in outgassing of gaseous molecules and water that impair the vacuum quality.

There are several methods for the mitigation of the contamination caused by these volatile organic molecules, yet many of these strategies are only suitable for robust samples, because the removal of contaminants often requires harsh conditions that can lead to oxidation or decomposition. In addition, equipment like the sample holder or tweezers used in the preparation may need to be cleaned as well. Applicable solutions for the removal of carbonaceous molecules include heating or cooling the sample, beam showering [29], plasma cleaning [9,22,36] and cleaning by ultraviolet radiation [19,33,35]. Many of these aggressive methods are not suitable for specimens that contain a high amount of carbon, e.g., as ligands or stabilizers.

In ETEM, additional issues may arise due to the controlled gas environment in the direct vicinity of the sample [17]. For such experiments, the pressure in the octagon can be adjusted in the range between a normal TEM vacuum (10^{-7} mbar) and ETEM conditions (up to 100 mbar) [24]. Volatile organic components (VOCs) can accumulate in the reaction chamber because the controlled gas atmosphere at relatively high pressures hinders their removal. In contrast, in standard TEM experiments, the pressure is many orders of magnitude lower in the close vicinity of the sample. Also, the composition of reaction gases in the ETEM can be altered by high doses of VOCs, which can result in undesired side reactions of the sample.

Samples of interest for TEM investigation can be prepared by a broad range of methods [34]. For samples prepared in solution, e.g., nanoparticles dispersed in a solvent, it is suitable to apply the sample as a droplet directly on the TEM grid. In this work, we have prepared samples by employing selected solvents commonly used in chemical synthesis and investigated the effect of the solvent on the controlled vacuum environment of an ETEM instrument. The impact of outgassing solvent residues, the persistence of these solvents in a TEM and the approach of VOC removal by plasma cleaning was studied

by performing mass spectrometry, which allowed investigations of the composition of the atmosphere surrounding the sample in a decomissioned ETEM octagon.

Our octagon model system differs in a few important points from the measurement environment inside of an ETEM instrument. While even the smallest organic traces can be investigated, it is impossible to quantify the impact of the electron beam. When illuminating the sample with the probe, volatile contaminants get reduced to amorphous carbon deposited on the specimen's surface. As these molecules are not contributing to the ETEM gas composition, the measured contaminant ion count rate would differ if an electron beam were present. Using contamination analysis by proton-transfer-reaction (PTR) mass spectrometry (MS), we are able to investigate a broad range of hydrocarbon molecules. These contaminants must have a proton affinity that is higher than that of water, whose protonated form is used for the ionization process during the analysis. While a broad range of organic components are well-suited candidates for this method, some solvents do not fulfill this requirement, e.g., n-alkane hydrocarbons.

2.3 Methods

In order to investigate the carbon contamination in ETEM under working conditions, all experiments were performed with a decommissioned Thermo Fisher Scientific ETEM octagon. Volatile carbon compounds contributing to contamination are investigated by PTR MS with a Ionicon PTR-TOF 1000 device.

The octagon, which comprises the encasement of the pole pieces of the microscope and also includes the sample, is named after the eight ports that are distributed evenly across the outer encasement. These are typically used for the airlock, the octagon pumping, the EDX system, but also for the stage controlling unit or, in case of an ETEM, for adjusting the pressure with the gas of choice to be used for the experiments. The distribution of the different components for our setup in shown in fig. 2.1.

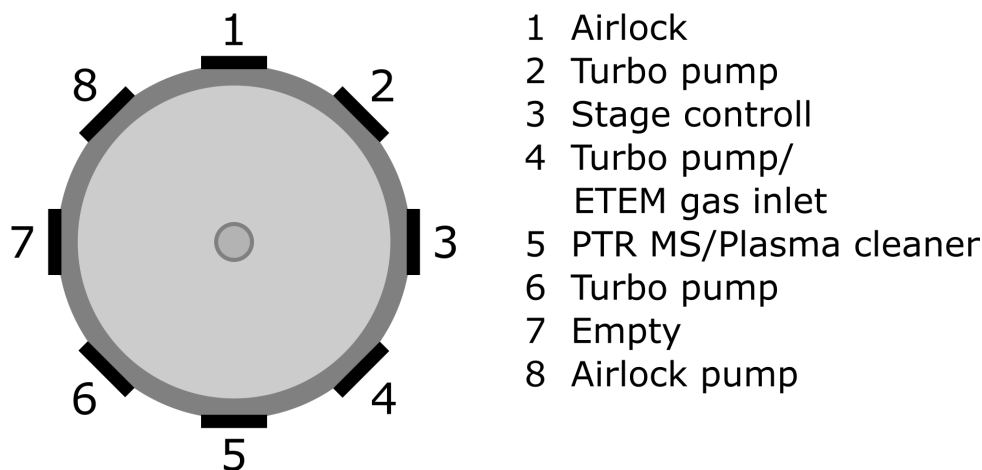

Figure 2.1: Distribution of different setup components across the eight octagon ports (top-down view).

For simulating the vacuum conditions as close as possible to the setup in a real ETEM, a differential vacuum system is used, which allows adjusting the ETEM pressure in the octagon, while maintaining a good vacuum in the other parts. The octagon was connected to the pumps by corrugated flexible hoses that could be heated to prevent adsorption of contaminants, which could impair the quality of the measurements.

In fig. 2.2 a photo of the octagon and its ports is shown, while a photo of the whole setup and its pumping system is shown in fig. 2.3. Depending on the pressure range that the experiments require, different settings of the valves attached to the ports are chosen: When pumping the setup to TEM pressure, three different turbo pumps are in use. Each of these has a pumping speed of approximately 70 L/s for nitrogen, and they pump either from the top of the setup (TP2), from the bottom (TP1) or from three sides of the setup, namely ports 2, 4 and 6 (TP3). Scroll pump SP1 was used as a backing pump for the turbo pumps exclusively, while SP2 was not in use.

During PTR analysis, the pressure was adjusted to a value in the ETEM range. Therefore, the gas entered the setup through ports 2 and 4, while the octagon was pumped by a scroll pump (SP2) using port 6. During the measurements, port 5 was used for connecting

the octagon to the PTR mass spectrometer. During plasma cleaning of the octagon, the pressure was reduced by pumping with SP2 as well, while the plasma cleaner was attached to port 5. For inserting the sample holder, the airlock attached to port 1 was used.

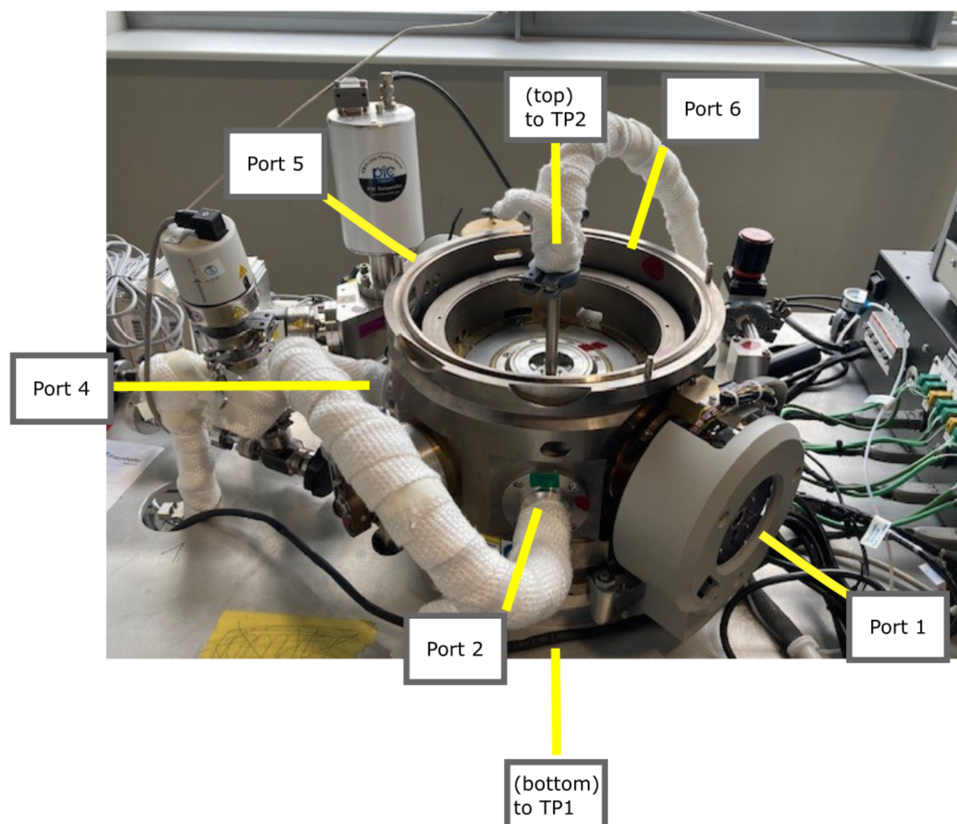

Figure 2.2: Photo of octagon with its different ports.

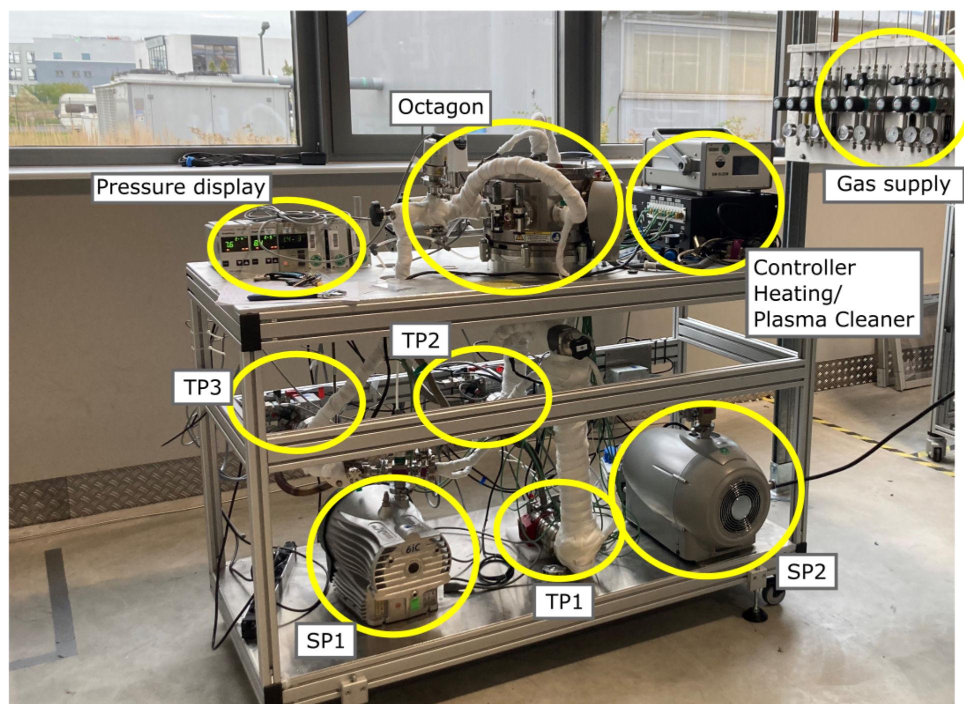

Figure 2.3: Photo of octagon setup and its main components, including the turbo pumps (TP) and scroll pumps (SP).

PTR MS allows for the characterization of molecules by ionization, employing protonated water molecules (H_3O^+) as primary ions, from which positive charges in the form of a proton are transferred to the organic reactants. The protonated reactants are then separated and analyzed in the detection unit with a time-of-flight MS system[4]. The advantages of this method are a fast time response, a low detection limit and low fragmentation of the reactants, making PTR MS the method of choice for the investigation of organic contamination. The ionization process is restricted by the proton affinity of water and only proceeds for compounds with a proton affinity greater than 165 kcal/mol, resulting in barely any ionization of air constituents[12].

In order to compare the signal intensities attained by the PTR MS, the data was corrected for the instrumental transmission and normalized to the primary ion intensity, so that the ion count rate is normalized to a primary ion signal of 10^6 counts per second. The signal

of an investigated protonated hydrocarbon species [HC] is therefore given by eq. (2.1).

$$[\mathrm{HC}]_{ncps} = \frac{[\mathrm{HC}^{+}_{corr}]}{[\mathrm{H}_3^{18}\mathrm{O}^{+}_{corr}]} \cdot 10^6 \tag{2.1}$$

The PTR MS device used for this work had a limit of quantification (LOQ) of 10 ncps, making interpretation of data below this threshold not possible, even if the acquired data reading is above the limit of detection (LOD) of 1 ncps, as otherwise an external calibration would be necessary for further quantification. Based on the low LOD and LOQ of PTR MS, it can be assumed that the octagon is virtually clean when the detected contaminant signal is below the LOQ and residual VOCs would not interfere with TEM measurements. All data was processed with the Ionicon PTR-MS Viewer (3.2.12) software.

While the proton affinity of a molecule, here that of the hydrocarbons THF, toluene and mesitylene, determines whether a proton transfer to the molecule is thermodynamically possible, the collisional rate constant k controls the reaction rate of the protonation. The value of k can be calculated as a function of the molecular mass, the polarizability α, the electric dipole moment μ of the molecule as well as PTR MS measurement parameters, such as the drift tube temperature, the drift tube voltage and the drift tube pressure. The values for k presented in table 2.1 were calculated based on the model suggested by Chesnavich *et al.*[5] by employing the collision rate calculator provided by Ionicon.

Solvent	$\alpha/\text{Å}^3$	μ/D	k / 10^{-9} cm^3 s^{-1}
THF	7.9[25]	1.63[25]	2.670
Toluene	11.8[16]	0.279[2]	2.091
Mesitylene	15.5[16]	0.178[2]	2.313

Table 2.1: Calculated reaction rate constant based on a method suggested by Chesnavich *et al.*[5] for THF, toluene and mesitylene.

Using eq. (2.2), the number density of a contaminant in the drift tube, N_{1/cm^3}, can be determined from the corrected signal intensities of the protonated hydrocarbon compound

$[HC^{+}_{corr}]$ and the primary proton donor ion $[H_3O^{+}_{corr}]$, the reaction rate constant, k, and the duration a molecule remains in the drift tube, t [21].

$$N_{1/cm^3} = \frac{[HC^{+}_{corr}]}{[H_3O^{+}_{corr}]} \cdot \frac{1}{kt} \tag{2.2}$$

Under consideration of the number of nitrogen molecules in the drift tube, $N_{\text{Nitrogen},1/cm^3}$, the concentration of the contaminant in parts per billion (ppb) can be determined according to eq. (2.3) [21].

$$C_{ppb} = 10^9 \cdot \frac{N_{1/cm^3}}{N_{\text{Nitrogen},1/cm^3}} \tag{2.3}$$

Overall, PTR MS is a semi-quantitative method with inaccuracies in the obtained data to with different factors contribute. The determined number densities are assumed to have an uncertainty of approximately 30%, with the collision rate being the main factor contributing to this uncertainty with around 20% [13]. Moreover, these calculations are made under the assumption that the sample gas enters the PTR mass spectrometer at atmospheric pressure, yet in our experimental setup the pressure was lower. Therefore, the discussed data is shown in units of normalized counts per second, while the data determining the concentration is included in the supporting information.

The investigated solvents tetrahydrofuran (THF), toluene (TOL) and mesitylene (MES) were dried by a molecular sieve and distilled before performing the experiments. For all measurements, the samples were prepared on commercially available TEM grids (Cu grids with lacey carbon, 400 mesh) purchased from Plano-EM. The samples were prepared by applying 1 µL of solvent on the grids and letting them dry for either 10 min or 30 min, respectively. As mesitylene is the least volatile solvent investigated and the grid was not dry after 10 min, an additional sample was investigated after a drying time of 60 min. For all measurements, the pressure in the octagon was adjusted to a value of 300 mbar of an N_2 (5.0 purity) atmosphere, as this pressure range is the lowest possible for stable

PTR MS measurements. The sample was kept at room temperature.

Each sample was subjected to three different measurement sets. In a long-term measurement, the outgassing solvent molecules were measured continuously over a period of 14 h. In these measurements, residual contamination desorbing from the octagon surfaces was investigated after the removal of the sample holder, and pumping the octagon with a vacuum system similar to one in a TEM. The gas composition was measured every hour for a total time of 5 h and after continuous pumping of the octagon overnight. Before each PTR MS measurement, the octagon pressure was adjusted and stabilized to the aforementioned conditions. As a third experiment, a plasma cleaning procedure was used for the removal of hydrocarbon contamination. Carbonaceous species were removed by an EM Kleen plasma cleaner (PIE Scientific LLC) operated at a chamber pressure of 250 mbar with an acceleration power of 75 W using synthetic air (80% N_2, 20% O_2) as a cleaning agent in intervals of 20 min with 10 min of vacuum pumping in between. The octagon was treated with plasma for a total time of 20 min, 2 h, 4 h and 16 h. After each of these intervals, the octagon gas composition ar ETEM pressure was measured.

2.4 Results

2.4.1 Long-term measurements under ETEM conditions

For the investigation of long-term outgassing of organic solvents, all measurements were started as soon as the sample holder was inserted in the octagon and PTR MS data was acquired for 14 h. The drying times of the samples were selected based on visual inspection, checking whether the grids were neither shiny nor sticky. Based on this, it was assumed that for the small solvent volume of 1 µL the drying time should be sufficient for TEM experiments. After the sample holder was inserted in the octagon, the mass spectrometer's internal measurement parameters were readjusted to maintain a stable primary ion signal despite the high hydrocarbon concentration in the sample inlet. Data

is therefore only shown starting from the point at which quantification of the hydrocarbons was possible.

The upper detection limit of the ion count rate is approximately 10^5 normalized counts per second (ncps), so that for the mesitylene samples an initial oversaturation of the detector was observed and this solvent could only be quantified after the PTR MS parameters had stabilized and the signal was below this threshold.

In fig. 2.4, data from mesitylene samples dried for 30 min (MES30) and 60 min (MES60) before insertion to the octagon is shown. Both measurements led to unstable PTR MS device parameters at the beginning of the measurements.

It was not possible to determine the maximum of the ion count rate of the contaminant signal for the MES30 and MES60 samples, although its steady decrease with time can be observed. The longer drying time of the MES60 sample resulted in a lower signal intensity than for the MES30 sample. For a drying time of 10 min (MES10), the concentration of mesitylene in the PTR MS was too high for the detectors to process in a reliable manner. Though the MES10 measurement was performed as described above in order to accumulate the contamination in the octagon for the given period, the data is not included in fig. 2.4.

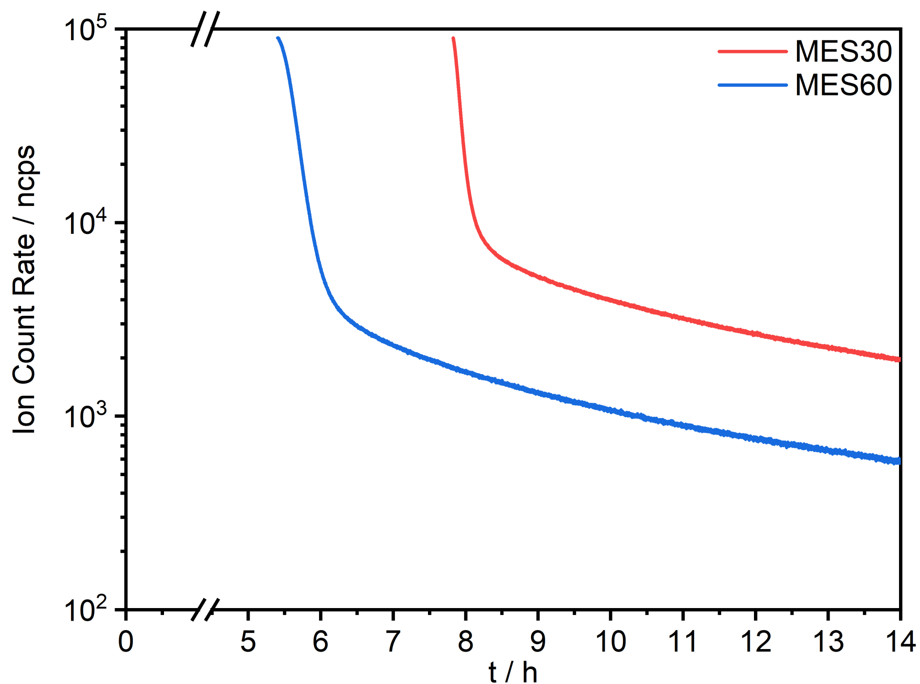

Figure 2.4: Long-term measurements of mesitylene contamination resulting from samples dried for 30 min (MES30, red) and 60 min (MES60, blue), respectively.

When investigating toluene as a solvent, a high ion count rate above the detection limits was observed at the beginning of the long-term measurements for both samples, for that dried for 10 min (TOL10) and for that dried for 30 min (TOL30). The long-term measurements shown in fig. 2.5 display the data that was measured after a initial detector oversaturation. A steady decrease of the ion count rate for both samples was observed. After 14 hours at ETEM working conditions, the ion count rate of TOL10 was 10 times higher than that of TOL30.

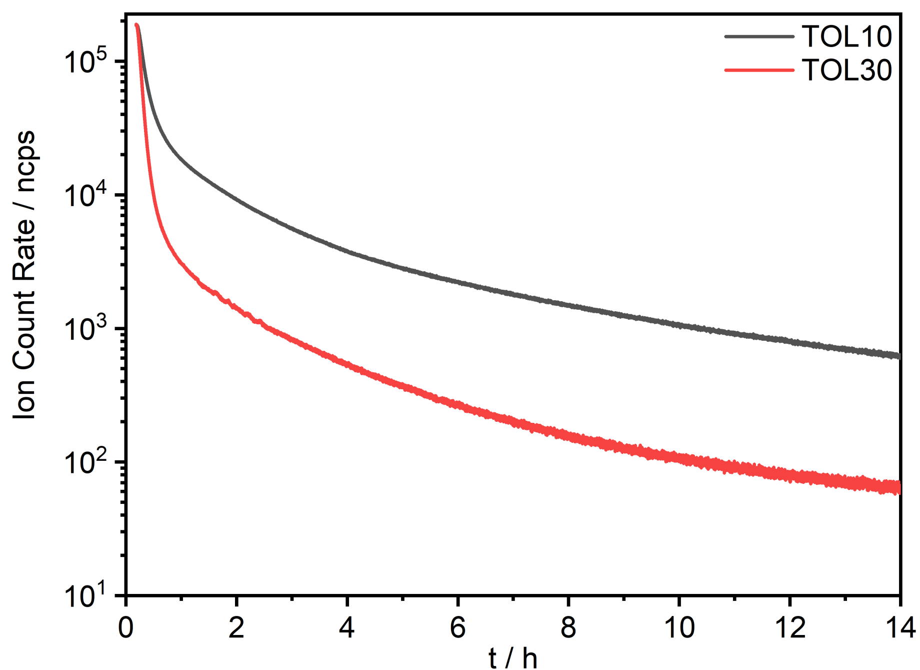

Figure 2.5: Long-term measurement of toluene samples dried for 10 min (TOL10, black) and 30 min (TOL30, red) before inserting the samples in the octagon.

As shown in fig. 2.6, the ion count rate of a THF sample dried for 10 min (THF10) decreased steadily during the time the sample was inserted in the octagon. For the THF sample that was dried for 30 min (THF30) before the measurement, the ion count rate decreased below the LOQ after 2 h.

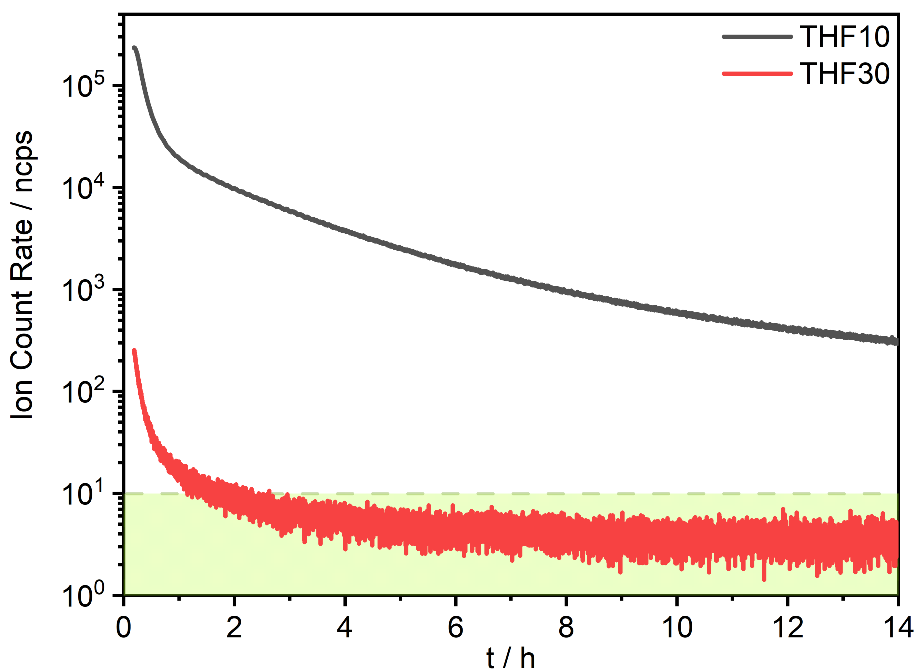

Figure 2.6: Long-term measurement of THF samples dried for 10 min (THF10, black) and 30 min (THF30, red) before inserting the samples in the octagon. Here and in analogous figures, ion count rates below the LOQ have a green background.

2.4.2 Removal of solvent molecules by vacuum

After accumulating solvent molecules under ETEM working conditions in the aforementioned long-term measurements for 14 h, the sample holder was removed from the octagon in order to investigate the contamination of the surfaces inside of the ETEM. The average ion count rate was determined immediately after the sample holder was removed from the octagon, subsequently in hourly intervals for 5 hours and after pumping the system overnight. For comparison, a background signal of the contaminant was measured before the sample holder was inserted for long-term measurements (see section 2.4.1), which indicates that before the experiments were started, the contaminant signal was below the LOQ for all solvents. This suggests that in a clean octagon, no traces of mesitylene, toluene or THF should be detectable. The displayed values show the average ion count

rate in normalized counts per second when measuring the PTR MS signal for 30 min with the standard deviation as the error bars.

As shown in fig. 2.7, already after 1 h of vacuum, far less mesitylene was measured, and with longer pumping times, a steady decrease could be observed. However, even after pumping over night (∼ 14 hours), the ion count rate remained higher than the background signal measured for a clean octagon before initially inserting the sample holder. The ion count rate for all three mesitylene measurements indicates the need to take further steps for contamination removal to ensure a clean octagon measurement environment after the investigation of the samples.

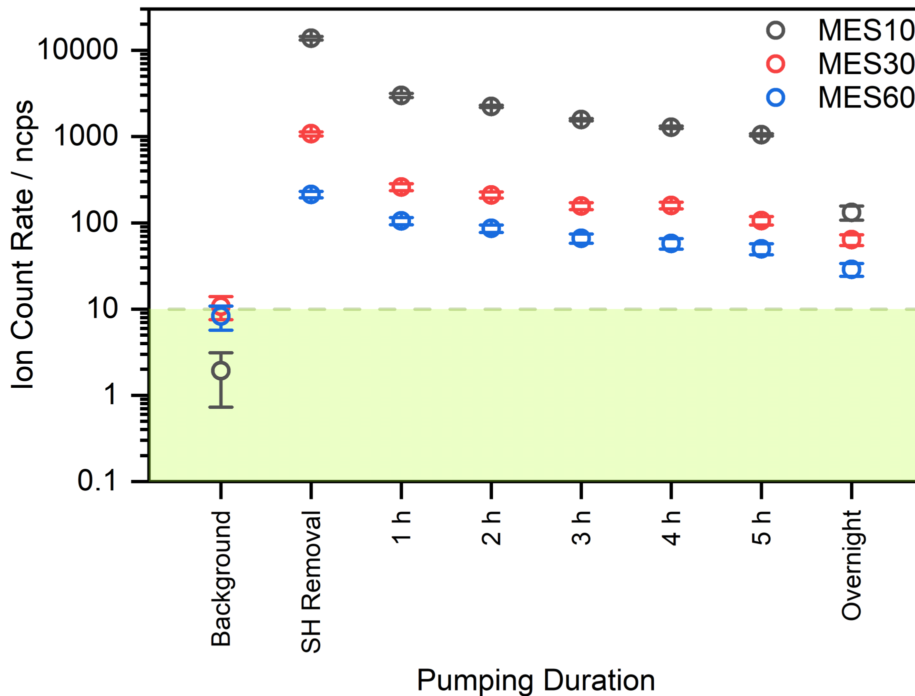

Figure 2.7: Ion count rate of MES10 (black), MES30 (red) and MES60 (blue) depending on the vacuum pumping duration.

The signal intensities for TOL10 and TOL30, shown in fig. 2.8, were higher than the background signals measured before sample insertion by a factor of ∼ 100 and 10, respectively. For TOL10, the pumping duration intervals between 1 and 5 hours lead to a slow

decrease compared to the signal after the sample holder removal, though all values were in a similar range. Extended overnight pumping resulted in a slightly lower ion count rate, although it was still higher than before sample insertion. Here, further cleaning procedures are required in order to remove additional toluene molecules. For TOL30, the ion count rate decreases steadily with longer pumping duration. After 2 h of pumping, the signal intensity was already below the LOQ.

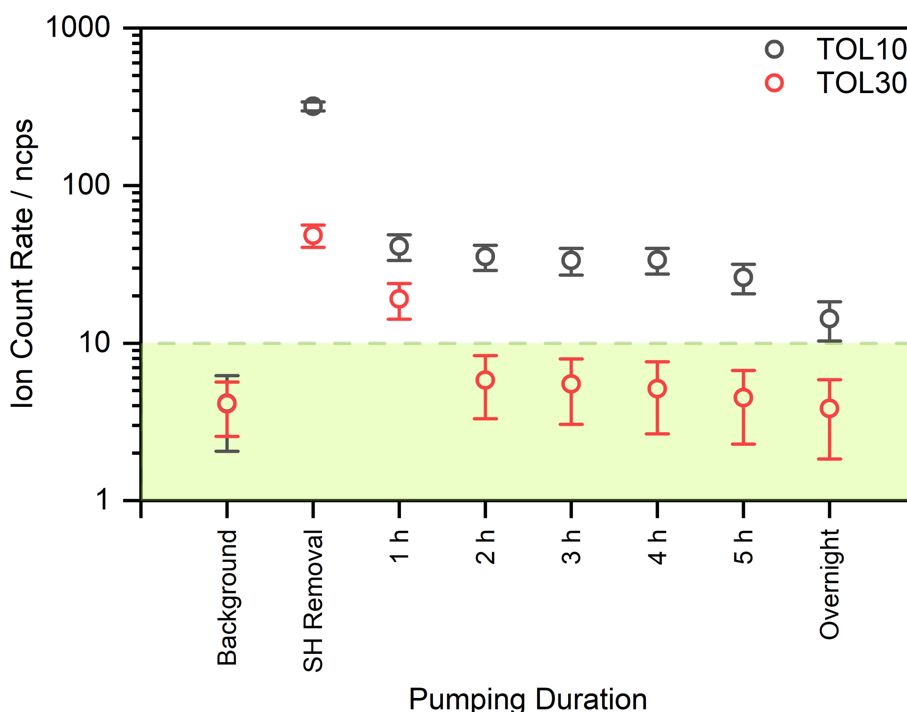

Figure 2.8: Ion count rate of TOL10 (black) and TOL30 (red) depending on the vacuum pumping duration.

After the removal of the sample holder with THF samples (fig. 2.9), the signal from the THF10 sample was more than 10 times higher than the background signal measured before sample holder insertion. When pumping the octagon with the ETEM vacuum system, after 1 h a drop in the signal intensity could already be observed. After 2 h of pumping, the THF10 signal fell below the LOQ, making further quantification not possible due to the low ion count rate. This also applied for the THF30 signal, which fell below the LOQ

after the long-term measurement.

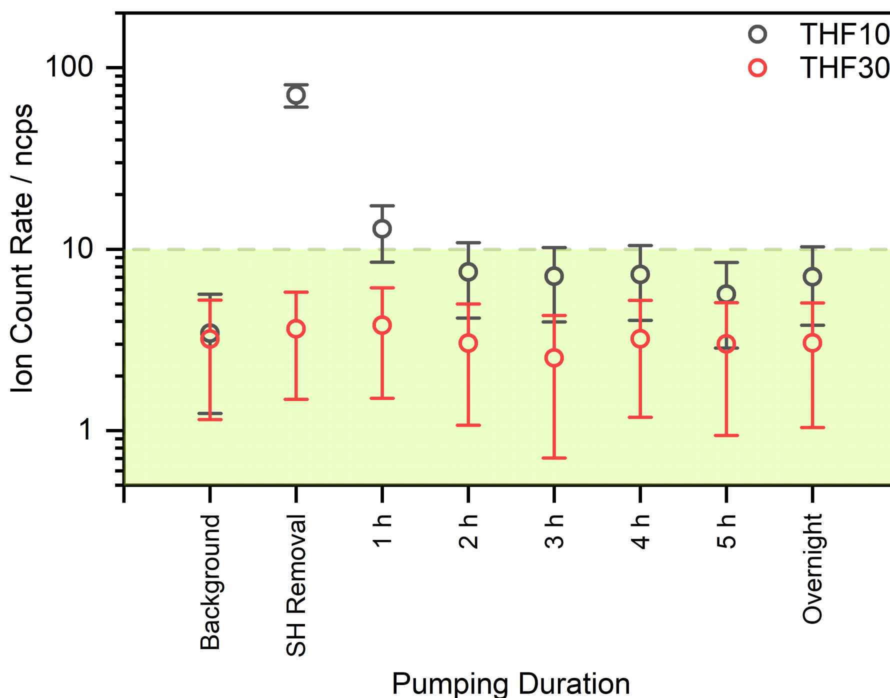

Figure 2.9: Ion count rate of THF10 (black) and THF30 (red) depending on the vacuum pumping duration.

2.4.3 Plasma cleaning of the octagon

As the previous experiments have shown, an increased hydrocarbon concentration accumulates in the ETEM atmosphere even after extensive pumping. Therefore, further cleaning procedures are required to remove remaining solvents from the octagon. By plasma cleaning the octagon in different intervals, insight on the cleaning properties of this method were gained.

For the case of MES10, a plasma cleaning duration of 20 min did not lead to much of an improvement, while for MES30 even an increase was observed after this duration (fig. 2.10). For both of these samples, longer plasma cleaning intervals lead to a steady decrease of the mesitylene signal, though only after 16 h the octagon returned to its

original state. In the case of MES60, already a short plasma application of 20 min resulted in a remarkable improvement of the octagon status. However, also for this sample, extended plasma cleaning of 4 h was necessary to reach the same level of cleanliness as before sample insertion.

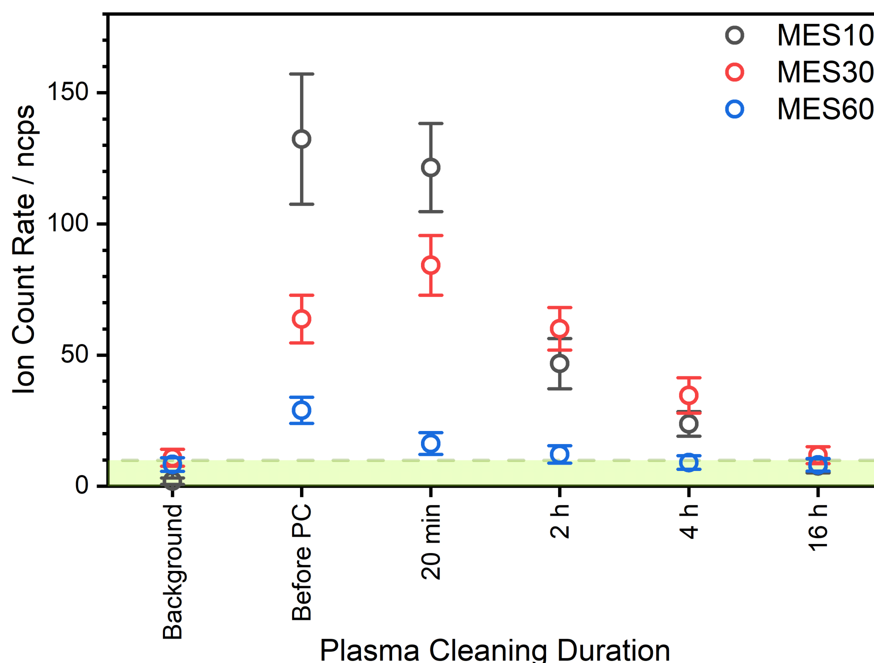

Figure 2.10: Ion count rate of MES10 (black), MES30 (red) and MES60 (blue) after plasma cleaning for different time intervals.

Also for toluene (fig. 2.11), additional plasma treatment was required to remove remaining molecules from the setup for TOL10, as not all of the solvent contaminants could be successfully removed by vacuum in the investigated time frame. After 20 minutes of plasma cleaning, no improvement was observed, though longer cleaning durations led to a consistent decrease of the ion count rate to values below the LOQ. As previously shown, for TOL30, already extended pumping was sufficient for contaminant removal (fig. 2.8), and all measured ion count rates were below the LOQ.

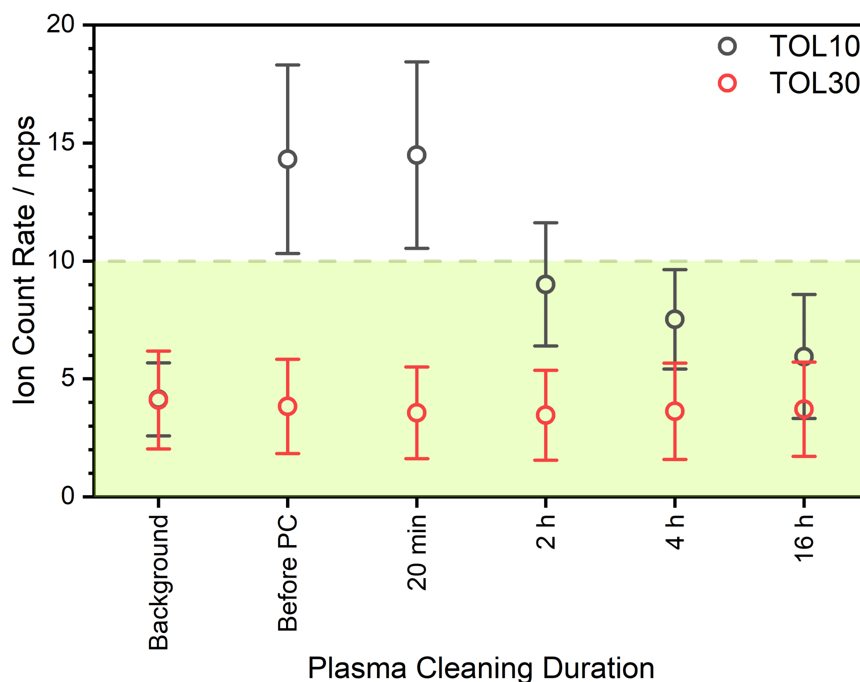

Figure 2.11: Ion count rate of TOL10 (black) and TOL30 (red) after plasma cleaning for different time intervals.

For the two THF measurements THF10 and THF30, most contaminating solvent molecules were already removed by establishing a vacuum (fig. 2.9). Therefore, plasma treatment of the octagon chamber did not influence the detected THF concentration (fig. 2.12), as the average ion count rate was below the LOQ.

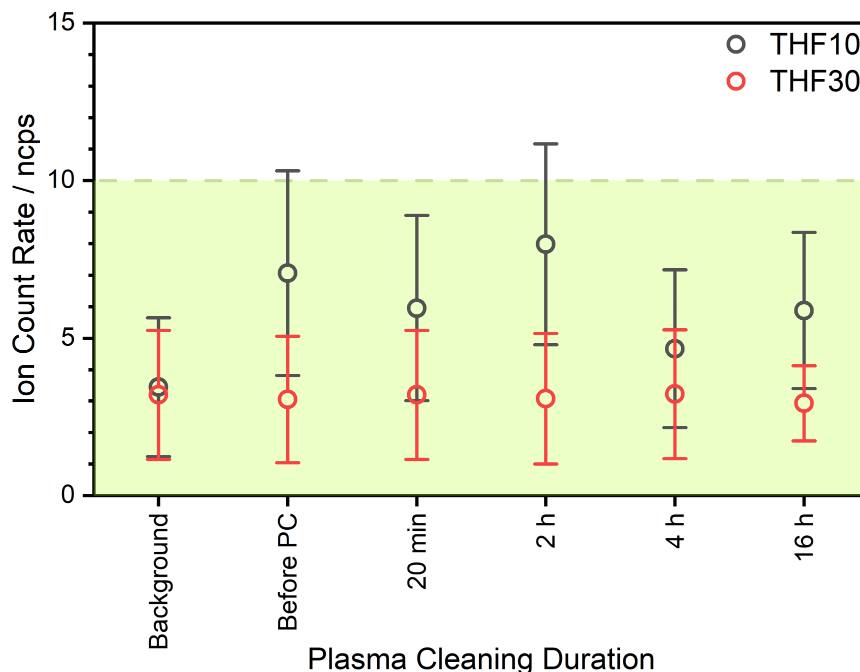

Figure 2.12: Ion count rate of THF10 (black) and THF30 (red) after plasma cleaning for different time intervals.

2.4.4 Residual gas composition and fragmentation products

In addition to the analysis of contaminants introduced by the sample itself, other components were traced by the PTR MS measurements as well. The signals of these either varied in their intensity, indicating that they are either parasitic ions produced during the measurements or fragmentation products, or remained in a similar range. When the observed ion count rate remained mostly constant during a measurement, it was assumed that the signals could be linked to PTR MS device artefacts. These are in depth discussed by Salazar Goméz *et al.*[31,32] for the device used for the measurements of this work.

During the measurements, the formation of water clusters (H_2O-H_3O^+) with m/z 37.027 could be observed. This signal is linked to the sample humidity, and in our case most likely to adsorbed water molecules, as the sample holder was stored in ambient air. It is safe to

assume that molecules detected by the PTR mass spectrometer had been introduced to the octagon environment by the sample holder.

In addition to the formation of water clusters, high signal intensities of different so-called parasitic species were observed. These molecules can be formed in side reactions in the drift tube and are linked to back diffusion processes of air, though another possible source might be fluctuations in the nitrogen purity due to the gas supply system or adsorption of air to the sample holder. The parasitic ions giving rise to high intensities and their masses are listed in table 2.2.

Molecular composition	m/z
NH_3^+	17.026
NH_4^+	18.034
N_2H^+	29.013
NO^+	29.997
O_2^+	31.989
$H_2O\text{-}H_3O^+$	37.027

Table 2.2: Molecular composition of the most important parasitic ions observed during PTR MS measurements.

The formation of these compounds can be linked to reactions of the nitrogen used for regulating the pressure in the octagon[1,30] or, for oxygen-containing species, to proton transfer reactions from protonated water or direct protonation of molecules diffusing in the detection system[12].

In fig. 2.13, we show and compare the ion count rates of water clusters (left side) and the two parasitic ions NO^+ and O_2^+ (right side) of the background measurement before the sample holder was inserted, after removal of the sample holder, after pumping the setup overnight and after plasma cleaning.For most measurements of water clusters, it was observed that, compared to the other measurements, the ion count rate increased after

the sample holder was removed. This indicates that high amounts of water molecules were adsorbed to the holder when it was not in use for the long-term measurements. The ion count rate of water clusters decreased afterwards to a value comparable to the background measurement with further removal of molecules either by extended vacuum pumping or plasma cleaning. For comparison, the ion count rate of the parasitic ions fluctuated, though they mostly remained in a similar range and could therefore not be attributed to the experimental setup. The data for other parasitic ions with a high count rate, i.e., NH_3^+, NH_4^+ and N_2H^+, are included in the supporting information. Additional parasitic ions with a high ion count rate were in particular protonated FeOOH and $Fe(OH)_2$ molecules, which are artefacts prevalent in the used device[31].

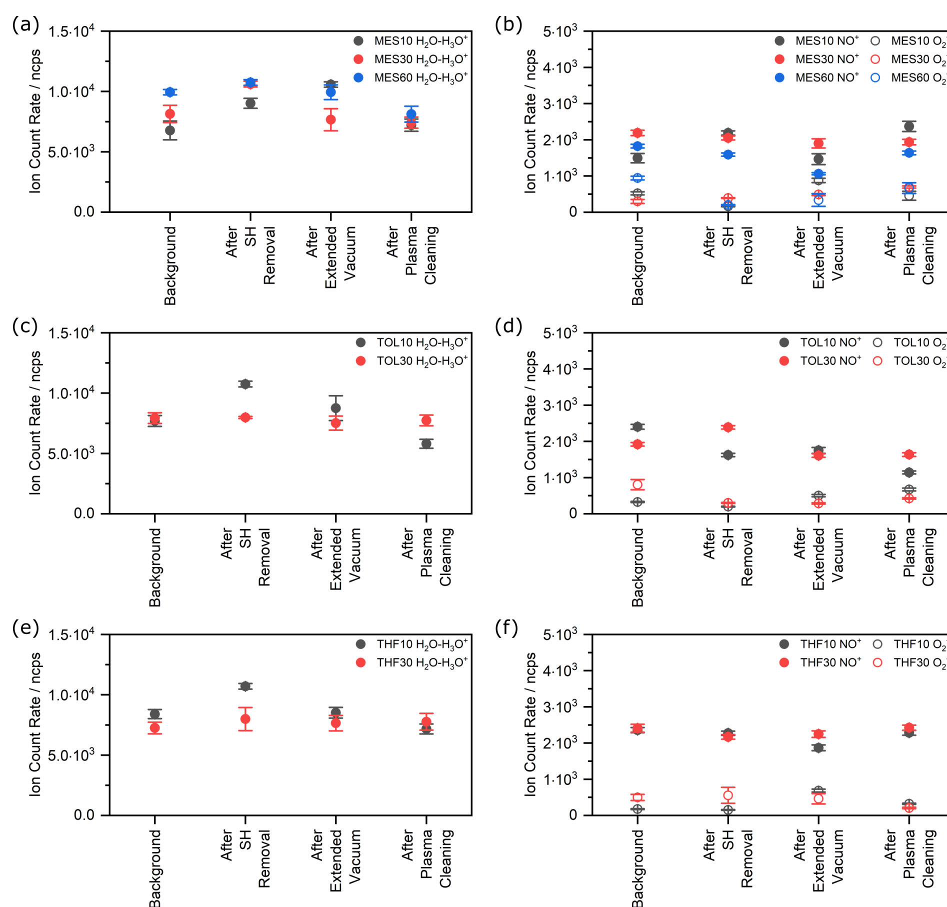

Figure 2.13: Ion count rate of H_2O-H_3O^+ clusters (left side) and the parasitic ions NO^+ and O_2^+ (right side) in measurements of samples containing mesitylene, toluene and THF.

Aside from the parasitic molecules and artefacts, signals from other species that can be linked to the samples themselves were measured. Though the fragmentation strongly depends on the E/N ratio, the three investigated solvents were investigated for possible fragmentation products. The E/N value is given by the ratio of the electric field strength to the number of neutral particles in the drift tube, and depends on parameters of the drift tube, i.e., the pressure, the temperature and the applied electric field strength [21]. For all measurements, a E/N value of 133 Td was chosen, at which the formation of water clusters is limited, though the probability of fragmentation processes increases due to the increased ion collision energies. For THF, possible fragmentation patterns suggested in the literature include a proton-bound dimer (m/z 145.122) and a fragment after loss of a water molecule (m/z 55.054); neither of these fragments or any other were observed in our studies [26]. In the case of toluene, no fragmentation patterns were observed, which is in agreement with the literature [10]. For mesitylene, we found fragmentation products at m/z 93.070 and m/z 105.070, which correspond to the loss of C_2H_4 and CH_4 fragments, respectively. The ratio of the mesitylene fragments is listed in table 2.3 and remained the same percentage during all measurements. Though these fragmentation products were only reported for dimethylbenzene, we could determine them for mesitylene samples as well [26].

Molecular composition	m/z	% Yield
$C_9H_{13}^+$	121.101	98.8
$C_8H_9^+$	105.070	1.0
$C_7H_9^+$	93.070	0.2

Table 2.3: Fragmentation products of mesitylene found in PTR MS analysis.

In addition to detecting signals corresponding to the investigated solvents, evidence other organic fragments could be observed. While some parasitic ions or artefacts are linked to the PTR MS device, some fragments can also originate from the octagon setup and the solvents. In fig. 2.14, a spectrum of the raw data of a PTR measurement is shown. Here,

the gas supply system was directly connected to the PTR MS device without passing through the octagon. Each peak can be assigned to a component, and all of them can be linked to the gas supply itself or to the PTR MS device; they therefore do not result from any solvents or the octagon[31,32].

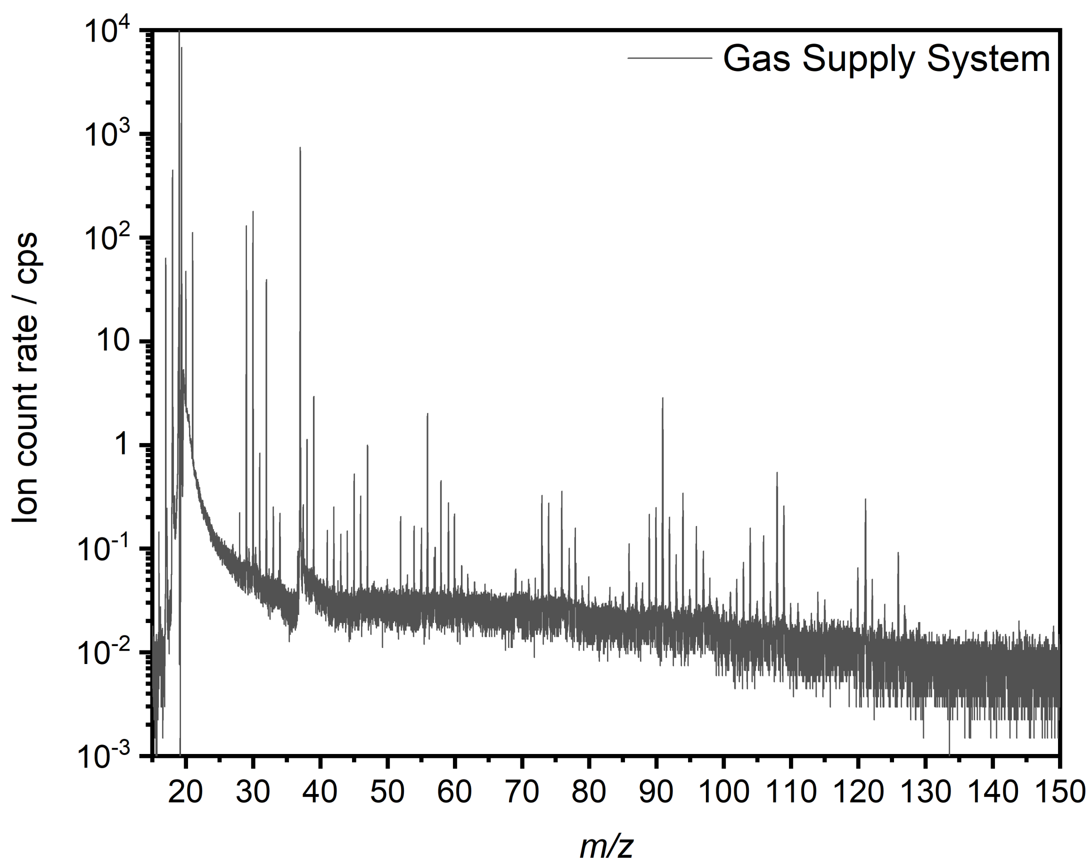

Figure 2.14: Spectrum of the raw data taken by measuring the nitrogen gas supply.

When comparing the data measured by observing solely the gas supply system with the data taken while the octagon was connected to the measurement system, the obtained signal intensities might vary: In fig. 2.15, the raw data from the gas supply only (black) is compared to that measured when passing the nitrogen through the empty, clean octagon.

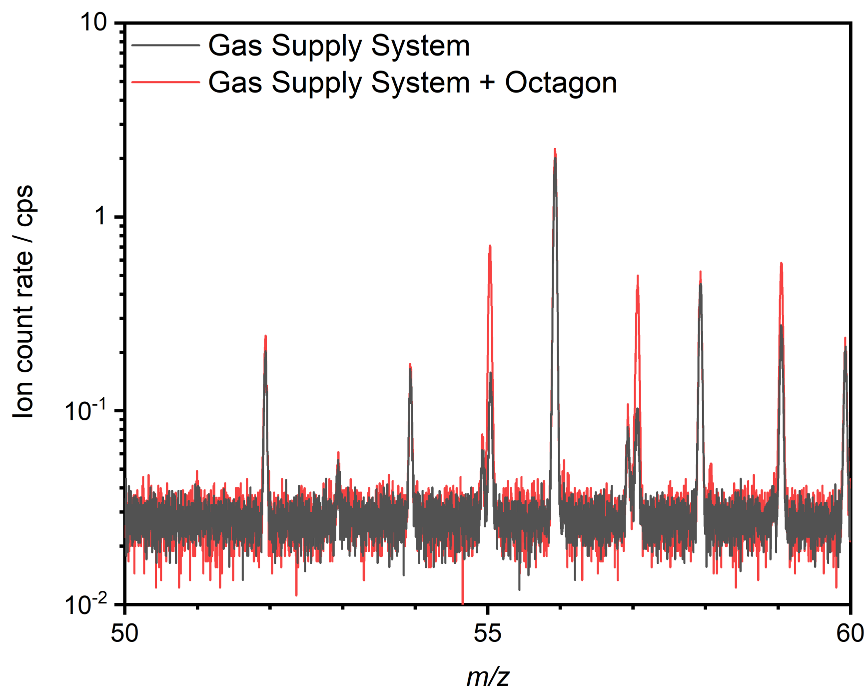

Figure 2.15: Raw data in a range between m/z 50 and m/z 60 of the nitrogen gas supply only (black) and the nitrogen gas supply passing through the octagon (red).

The detected components and their masses are listed in table 2.4. While for the metallic components, the intensity remained the same when comparing the two measurements, differences in the ion count rate could be observed for compounds with the chemical compositions $(C_4H_6)H^+$, $(C_4H_8)H^+$ and $(C_3H_6O)H^+$ when the nitrogen used for the measurements is lead trough the octagon. The first two compounds are most likely linked to either the O-ring sealings used for connecting the parts of the setup or to ionization fragments of desorbed hydrocarbons caused by the pressure gauge. The small change of the ion count rate for $(C_3H_6O)H^+$ can be linked to acetone, which might diffuse through possible leaks in the setup. A complete list of signals linked exclusively to the octagon that do not appear in the measurement of the gas supply system only, is presented in table 2.5 sorted by the m/z range. The corresponding spectra are included in the supporting information.

m/z	Molecular composition
51.9411	Cr^+
53.9396	$^{54}Fe^+$
55.0548	$(C_4H_6)H^+$
55.9349	$^{56}Fe^+$
56.9353	$^{57}Fe^+$
57.0704	$(C_4H_8)H^+$
57.9361	Ni^+
59.0491	$(C_3H_6O)H^+$

Table 2.4: Compounds found in PTR MS analysis in the range between m/z 50 and m/z 60.

m/z range	Molecular composition (corresponding m/z)
40 - 50	$(C_3H_4)H^+$(41.0391); $(C_3H_6)H^+$(43.0296); $(H_3OSi)H^+$(48.0031)
50 - 60	$(C_4H_6)H^+$(55.0548); $(C_4H_8)H^+$(57.0704); $(C_3H_6O)H^+$(59.0491)
60 - 70	$(C_3H_8O)H^+$(61.0653); $(C_5H_8)H^+$(69.0704)
70 - 80	$(C_4H_6O)H^+$(71.0497); $(C_4H_{10}O)H^+$(75.0810)
80 - 90	$(C_6H_8)H^+$(81,0704); $(C_6H_{10})H^+$(83.0861); $(C_5H_8O)H^+$(85.0653)
	$(C_5H_{10}O)H^+$(87.0922)
90 - 100	$(C_6H_{10}O)H^+$(99.0810)
100 - 110	N/A
110 - 120	$(C_7H_{10}O)H^+$(111.0922); $(C_7H_{12}O)H^+$(113.0966);
	$(C_7H_{10}O)H^+$(115.1123)
120 - 130	$(C_8H_{10}O)H^+$(127.1123); $(C_{10}H_8)H^+$(129.1279)
130 - 140	N/A
140 - 150	$(C_{11}H_{10})H^+$(143.0861)

Table 2.5: Compounds found in PTR MS analysis of the empty octagon up to m/z 150.

These compounds were measured in the octagon after plasma cleaning with synthetic air before any solvents were inserted. Overall, the intensity of these signals is far below the LOQ. It should be noted that the observed compounds all contained carbon and hydrogen and some, in addition, oxygen. This implies that these molecules are removed from the surfaces or O-ring sealings due to the oxidizing properties of the synthetic air plasma. It can also not be ruled out that some hydrocarbon compounds are formed in the pressure gauges, as discussed in section 1.3. When comparing the gas composition to that measured after plasma cleaning aimed at the removal of solvent residues as discussed in section 2.4.3, only very minor changes can be observed without any trend regarding the solvent that was investigated beforehand.

When the gas composition was contaminated by solvent molecules, e.g., during long-term measurements, some changes could also be observed: For mesitylene, in addition to the aforementioned fragments $(C_7H_8)H^+$ (m/z 93.0704) and $(C_8H_8)H^+$ (m/z 105.0704), signals corresponding to $(C_4H_6)H^+$ (m/z 55.0548) and $C_9H_{10}H^+$ (m/z 119.0861) were measured. These two signals fluctuated in their intensity and could not be related to the mesitylene concentration observed in the mass spectrometer, though the components were only observed when high amounts of mesitylene were detected. For toluene, an increased signal intensity for $(C_5H_8)H^+$ (m/z 69.0704) was observed, which can be linked to isoprene units. It seems likely that these are fragments of toluene, but as the fragmentation ratio between toluene and isoprene strongly fluctuated, they might also be linked to the O-ring material in the setup which can be dissolved by toluene vapor. When investigating THF, increased signal intensities were measured for $(C_3H_4)H^+$ (m/z 41.0391), $(C_3H_6)H^+$ (m/z 43.0296) and $(C_4H_6O)H^+$ (m/z 71.0497). These signals trace THF fragments, though they do not appear in a defined ratio to the THF signal. The detected species and the solvent they are linked to are summed up in table 2.6.

Solvent	Additional fragments
Mesitylene	$(C_4H_6)H^+$ (m/z 55.0548); $C_9H_{10}H^+$ (m/z 119.0861)
Toluene	$(C_5H_8)H^+$ (m/z 69.0704)
THF	$(C_3H_4)H^+$ (m/z 41.0391); $(C_3H_6)H^+$ (m/z 43.0296)
	$(C_4H_6O)H^+$ (m/z 71.0497)

Table 2.6: Overview of fragments found in traces with a fluctuating signal intensity in the presence of a solvent.

Overall, all of these fragments observed during the measurements appeared in very small fractions, i.e, less than 0.1% of the solvent molecule with strong fluctuations in the intensity of their signals. These fluctuations are probably linked to ionization processes of solvent molecules in the pressure gauge, in which hydrocarbon compounds can get fragmented during the measurement process. The partial pressure of the solvent molecules can be assumed to be nearly proportional to the concentration of ionized hydrocarbon species.

2.5 Discussion

The long-term measurements allow an assessment of the development of contaminant molecules accumulated on the surfaces inside a TEM octagon after sample insertion. It is important to note that outgassing solvent molecules do not exclusively accumulate in the gas environment, but also get attached to the surfaces in the immediate environment of the sample location, e.g., the objective lenses and the apertures. The measured ion count rate is determined based on the current ETEM gas composition and does not represent the total contaminant quantity induced by the sample, as the adsorbed hydrocarbon species cannot be probed. Our long-term studies give insight on the order of magnitude of contamination in the presence of a sample and its residues after sample holder removal and provide information about organic impurities in the ETEM gas.

The long-term measurements are limited by the upper detection limit of the PTR MS device. When the detectors are oversaturated, a certain amount of time needs to pass until the signal stabilizes and reliable measurements can be resumed.As the procedure is identical for all measurements, even though no information about the maximum ion count rate can be obtained, the accumulated contamination was collected over the same time period and therefore can be compared to that determined in the course of other experiments. The mesitylene samples have shown the highest ion count rates in long-term experiments, are we find a decreasing trend over toluene to THF. The high ion count rates indicate that the sample solvents at the chosen drying time were still outgassing and, based on their volatility, still had not dried enough to allow experiments under a defined controlled gas atmosphere. Only the ion count rate of THF30 decreased below the LOQ, allowing for the assumption that at this point the solvent had no impact on the ETEM gas composition anymore. For all other measurements, the ion count rate was significantly increased compared to the signal intensity before the sample holder insertion, which was below 10 ncps for all measurements. The data of the long-term measurements shows that a longer drying time leads to a lower ion count rate, indicating fewer volatile solvent molecules and therefore a cleaner sample environment during measurements. The development of the PTR MS signals corresponds well to the vapor pressures of these solvents, which are given at 25 °C with 0.33 kPa (mesitylene), 3.79 kPa (toluene), and 21.6 kPa (THF), respectively[16].

Measurements probing the removal of accumulated solvent contamination give insight in how long traces of a not sufficiently dried sample remain in the microscope system. The octagon was pumped with a typical TEM pumping setup to a high vacuum ($<10^{-6}$ mbar) between the different PTR MS measurements which were performed at conditions near the ETEM range (300 mbar). Therefore, it can be assumed that the development of the traces over time can also be compared to the accumulation of solvent contamination in typical transmission electron microscopes. For the case of mesitylene, a steady decrease of the signal intensities was observed with longer pumping times, yet the signal intensities for

all different drying times were much higher than before sample insertion. As mesitylene remains in the octagon even after evacuating for extended amounts of time, it is safe to assume that the selected sample preparation is not suitable for sensitive vacuum systems, which rely on an overall clean environment. Additional contaminant removal steps are needed to ensure a clean sample environment when this solvent is used. Toluene also accumulated in the octagon gas, as the measurements after sample holder removal showed. Though solvent removal by vacuum was not very efficient for a sample dried for 10 minutes, the remaining toluene for the TOL30 sample could be removed by vacuum quite well with extended pumping. After several hours, the signal was in the same range as before sample insertion. This leads to the conclusion that with a sufficient drying time, toluene will not contribute to the gas composition under ETEM conditions anymore. THF was the candidate with the highest vapor pressure, and could be removed by vacuum quite well, though it is worth mentioning that also here a longer drying time led to a decrease below the LOQ much faster. The ion count rates measured after the sample holder was removed indicate that a sufficient drying time of a sample can reduce the contamination in a microscope octagon to a level at which it has no impact on experiments in the ETEM pressure range.

Plasma cleaning was chosen for contamination removal in the octagon and has been proven to be a method with which the surfaces in the inner of the octagon can be cleaned in an efficient manner by breaking the carbonaceous molecules down to gaseous fragments. Overall, though plasma cleaning works well for our decommissioned octagon, this procedure is not suitable for cleaning an octagon inside of a microscope still in use due to its aggressive properties, which can harm components, e.g., EDX detectors, and also because of extended downtimes of the microscope during the cleaning process. Mesitylene contamination was still measurable in the octagon after extended pumping for all three drying times. The contaminants could successfully be removed by a synthetic air plasma, though quite long cleaning times were necessary in order to remove most mesitylene contamination. For the shorter dried samples MES10 and MES30, after 20 min of

plasma cleaning only a small difference in the ion count rate could be observed: While for MES10, a small decrease was observed, the signal intensity for MES30 increased. Due to the selected plasma cleaning intervals, it was impossible to assess if the amount of mesitylene initially increased in MES10 as well, though this appears plausible, as the plasma is quite efficient in removing VOCs and desorbing the species from the surfaces before breaking them down, as it happened in the case of MES30. This also applies for TOL10, where again a slightly increased ion count rate could be observed after 20 min of plasma cleaning. While longer cleaning times resulted in a decrease of the signal intensity, after 2 h the value was found to be below the LOQ, indicating that toluene no longer impacted the gas composition in the octagon. For TOL30, THF10 and THF30 the ion count rate was already before plasma cleaning below the LOQ. There was no signal increase detected for these samples, so it stands to reason that the octagon was mostly free from contaminants beforehand. It can be assumed that in this case the outgassing molecules were completely removed by vacuum and plasma cleaning is not required for the removal of these molecules. It is important to notice, that the plasma breaks down the contaminants to molecule fragments, which do not meet the requirement for quantification by PTR MS.

The experiments give insight on how to improve the sample preparation in order to reduce contamination without changing the properties of the sample. While the removal of volatile organic molecules can be supported by extended vacuum application quite well, outgassing in the microscope is not recommendable as it is tedious to remove VOCs from the octagon. Though plasma cleaning our decommissioned octagon worked well, cleaning a microscope by this method is a complex procedure and is not suitable to be performed on a regular basis. We found that preventing contamination by elaborate sample preparation is the central starting point for improving the cleanliness of the octagon environment in a TEM.

2.6 Conclusion

Our experiments on outgassing solvent molecules of TEM samples give insight into the importance of careful sample preparation when using samples dispersed in solvent. It is crucial to let the specimen dry long enough before inserting it into the microscope in order to keep the ETEM sufficiently clean. In the ETEM pressure range, only the THF30 sample was dried sufficiently and had only little impact on the gas environment.

Extended durations under TEM octagon vacuum conditions (approximately 10^{-7} mbar) were helpful for reducing the contaminant concentration regardless of the used solvent. THF and toluene could be removed well by the vacuum, indicated by significant decreases of their signals, though TOL10 could not be removed completely. For all three mesitylene samples, the contamination could not be removed below the LOQ by vacuum and required intensive cleaning treatment. In our experiments, the contamination could only be completely removed by extended air plasma cleaning, making mesitylene a solvent that should be avoided in TEM sample preparation. As the behaviour of the three investigated solvents followed a trend following their vapor pressures and boiling points, our knowledge can be expanded to other solvent as well. Based on the solvent properties, drying parameters can be adjusted, e.g., by heating the sample or expanding the drying time for removing most volatile molecules and preventing contaminants from influencing the gas composition in the volume surrounding the sample.

Though we have investigated contamination for the example of a decommissioned octagon under ETEM conditions, the problem of contamination also appears in TEM experiments at low pressure. Considering how long the contaminants were detectable even after pumping the octagon to TEM pressure, it can be assumed that for low-pressure TEM experiments, the sample environment contains a high contaminant concentration especially in the first hours after the sample holder was inserted. The vacuum removal of contaminants also takes time, so even measurements made later in time might be affected by contamination resulting from previous samples that were not sufficiently cleaned. The

outcomes of the experiments on THF, toluene and mesitylene samples prepared for TEM experiments need to be seen as a call for caution when preparing samples that are to be investigated with high resolution.

2.7 Supporting information

Contaminant concentration of solvents

In addition to signal intensities in normalized counts per second, which are shown in section 2.4, the concentrations of all contaminants in the sample gas are shown here. The results of long-term experiments (section 2.4.1) of the three solvents are shown in fig. 2.16, fig. 2.17 and fig. 2.18, experiments investigating the different pumping durations to TEM vacuum (section 2.4.2) are shown in fig. 2.19, fig. 2.20 and fig. 2.21, while data collected during plasma cleaning experiments (section 2.4.3) is shown in fig. 2.22, fig. 2.23 and fig. 2.24.

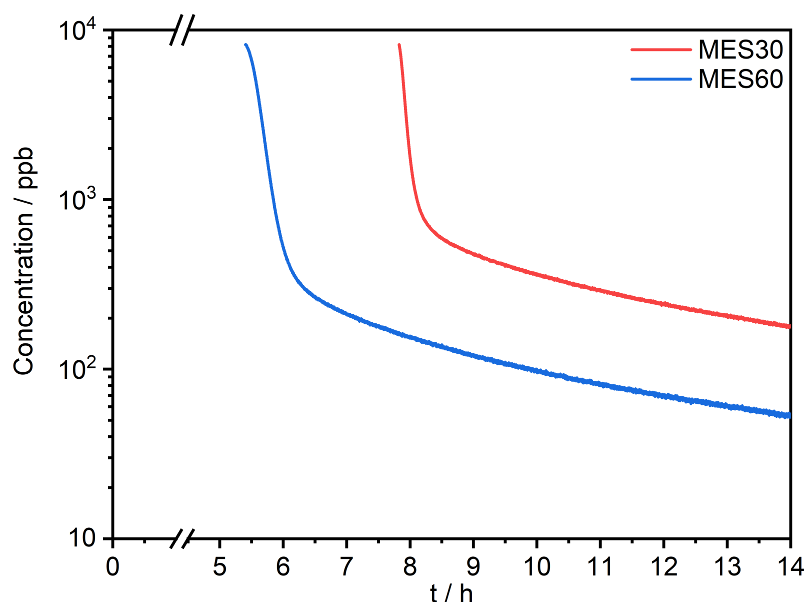

Figure 2.16: Concentration of MES30 (red) and MES60 (blue) determined in long-term measurements while the sample holder is inserted in the octagon.

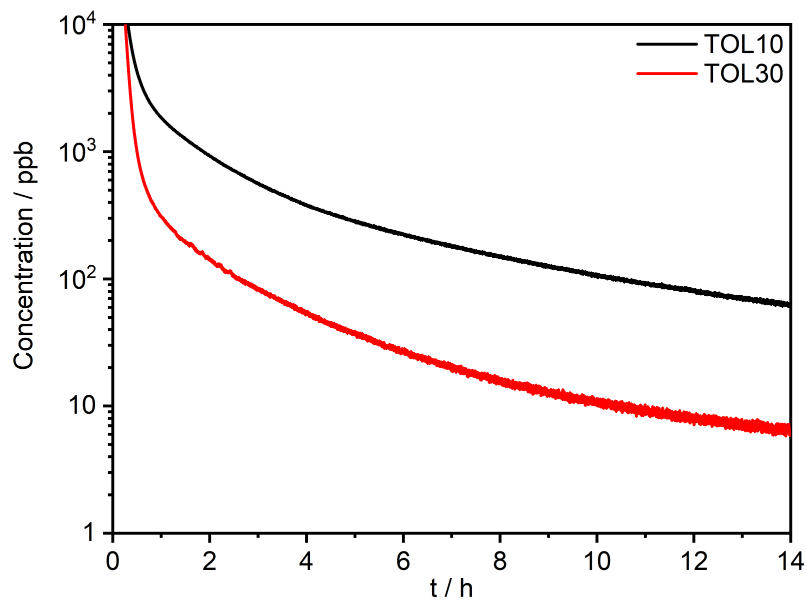

Figure 2.17: Concentration of TOL10 (black) and TOL30 (red) determined in long-term measurements while the sample holder is inserted in the octagon.

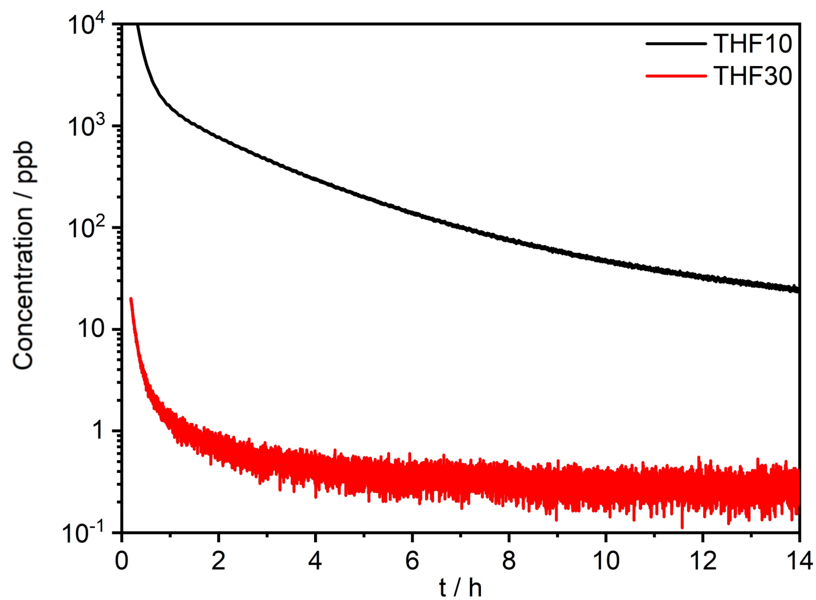

Figure 2.18: Concentration of THF10 (black) and THF30 (red) determined in long-term measurements while the sample holder is inserted in the octagon.

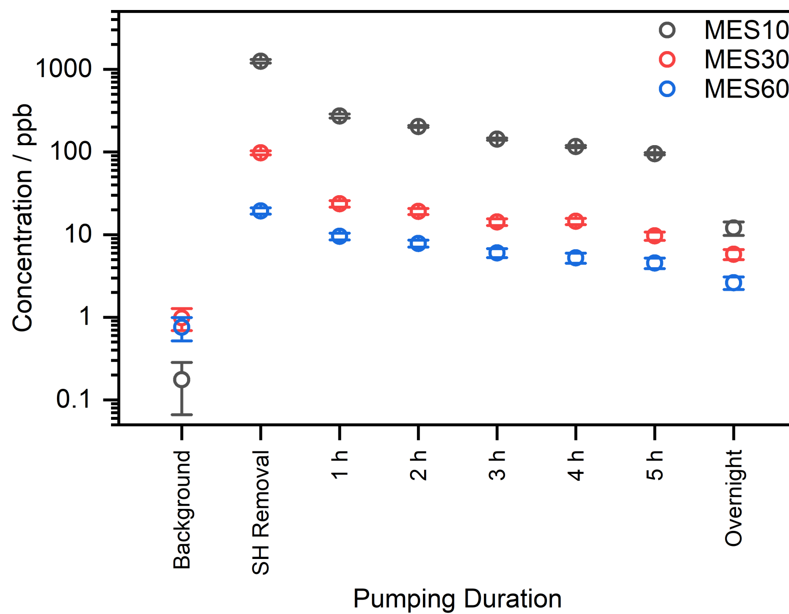

Figure 2.19: Concentration of MES10 (black), MES30 (red) and MES60 (blue) after pumping the octagon to TEM pressure for different durations.

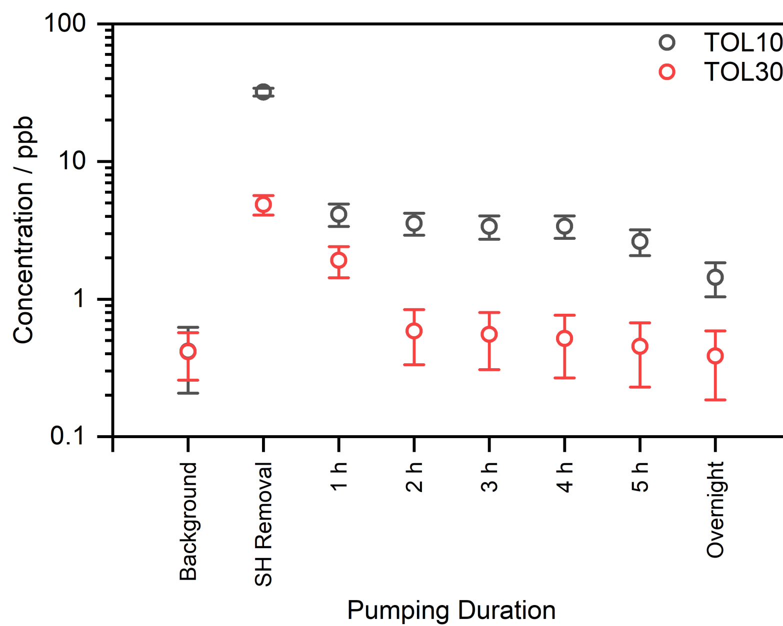

Figure 2.20: Concentration of TOL10 (black) and TOL30 (red) after pumping the octagon to TEM pressure for different durations.

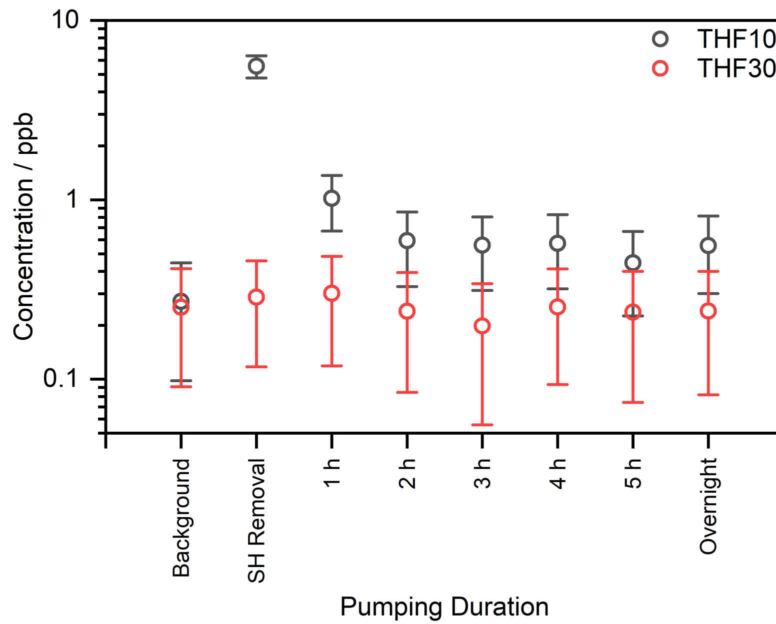

Figure 2.21: Concentration of THF10 (black) and THF30 (red) after pumping the octagon to TEM pressure for different durations.

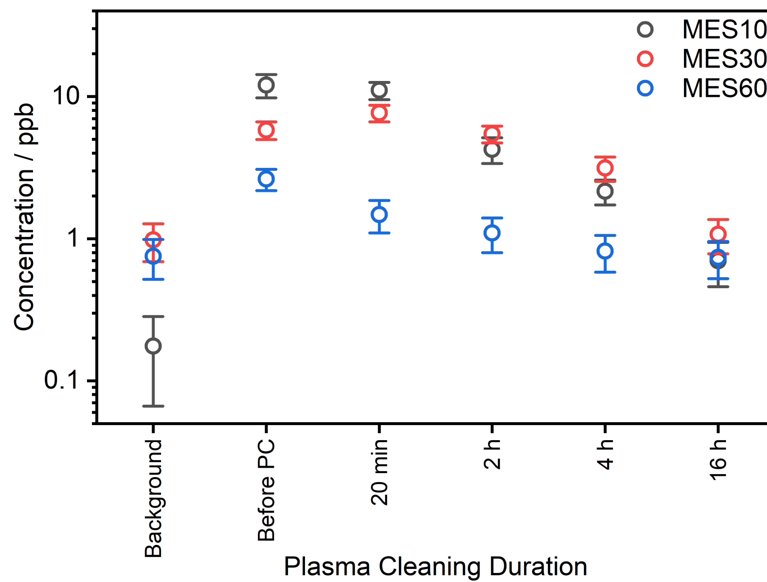

Figure 2.22: Concentration of MES10 (black), MES30 (red) and MES60 (blue) after different plasma cleaning intervals.

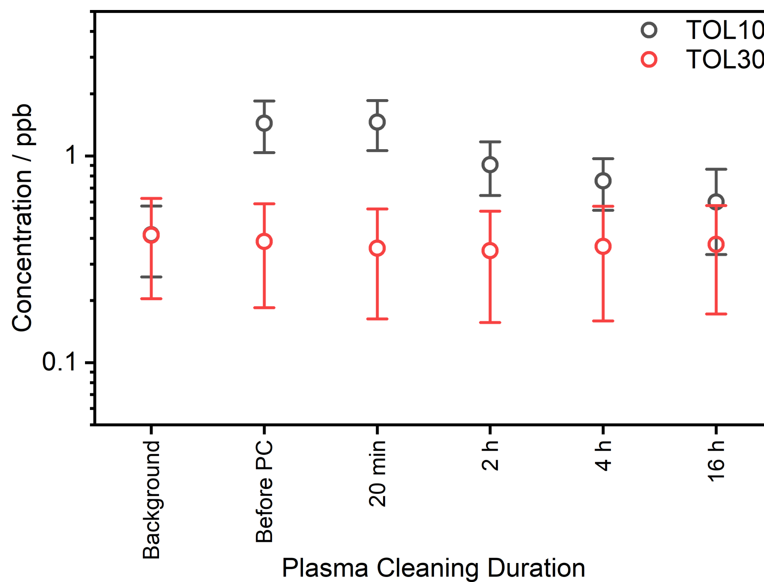

Figure 2.23: Concentration of TOL10 (black) and TOL30 (red) after different plasma cleaning intervals.

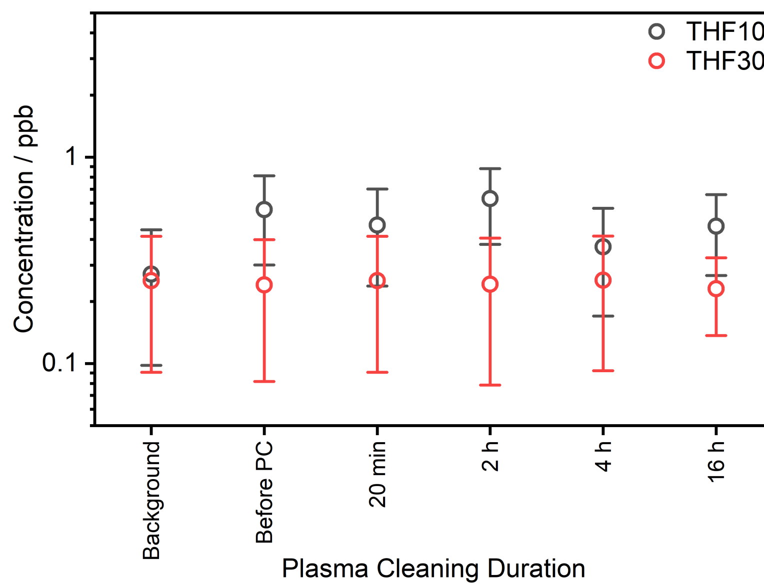

Figure 2.24: Concentration of THF10 (black) and THF30 (red) after different plasma cleaning intervals.

Additional parasitic ions

In addition to the parasitic ions discussed in section 2.4.4, other parasitic ions, namely NH_3^+, NH_4^+ and N_2H^+ had high ion count rates as well. The data for these ions with different solvents is shown in fig. 2.25, fig. 2.26 and fig. 2.27, respectively.

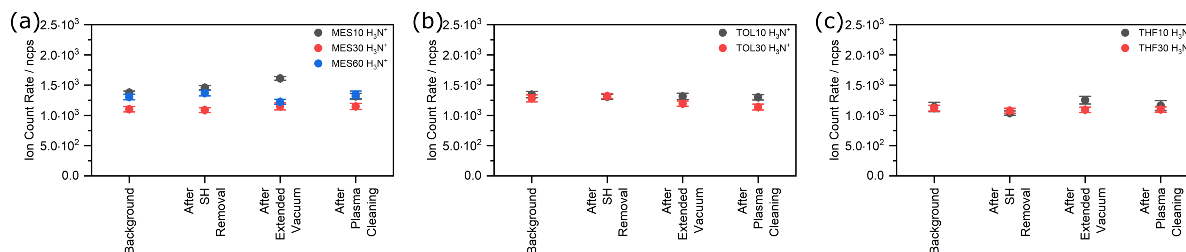

Figure 2.25: Ion count rate of NH_3^+ ions during PTR MS experiments with mesitylene (a), toluene (b) and THF (c).

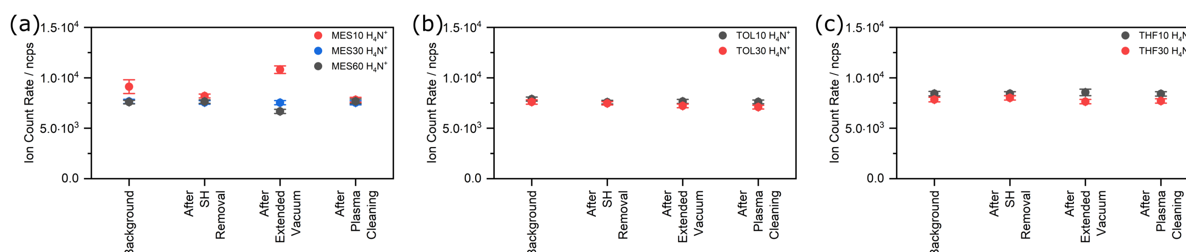

Figure 2.26: Ion count rate of NH_4^+ ions during PTR MS experiments with mesitylene (a), toluene (b) and THF (c).

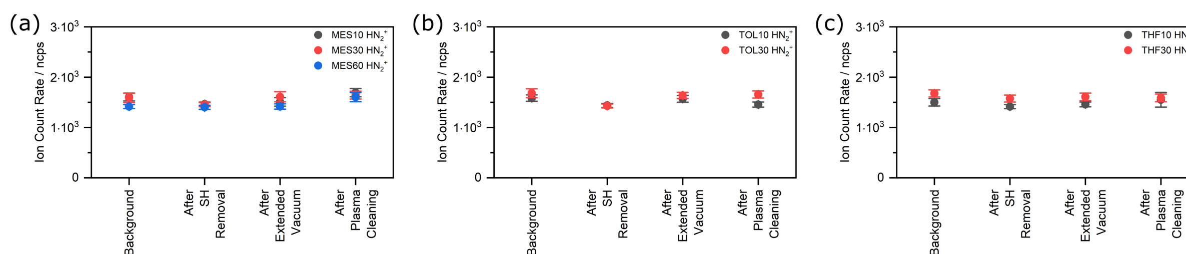

Figure 2.27: Ion count rate of N_2H^+ ions during PTR MS experiments with mesitylene (a), toluene (b) and THF (c).

Raw data of the nitrogen gas supply and the octagon setup

The raw data comparing traces resulting from the nitrogen supply system and PTR MS artefacts to traces that originate from the octagon setup are compared in fig. 2.28 and fig. 2.29.

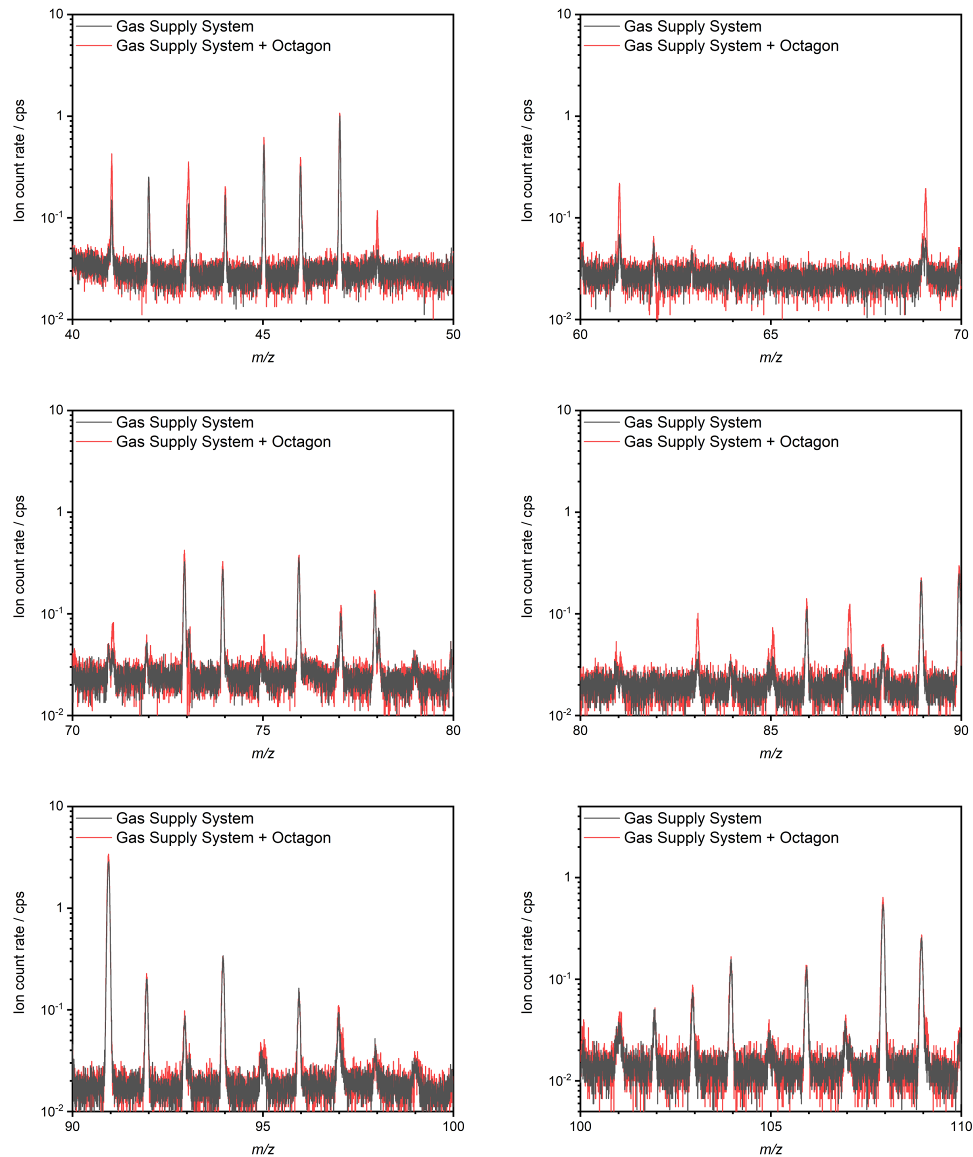

Figure 2.28: Raw data of the nitrogen gas supply only (black) and the nitrogen gas supply passing through the octagon (red)in m/z 10 wide ranges centered on m/z 45 and 65 (top row), m/z 75 and 85 (middle row) and 95 and 105 (bottom row). 50 and m/z 60 and m/z 110.

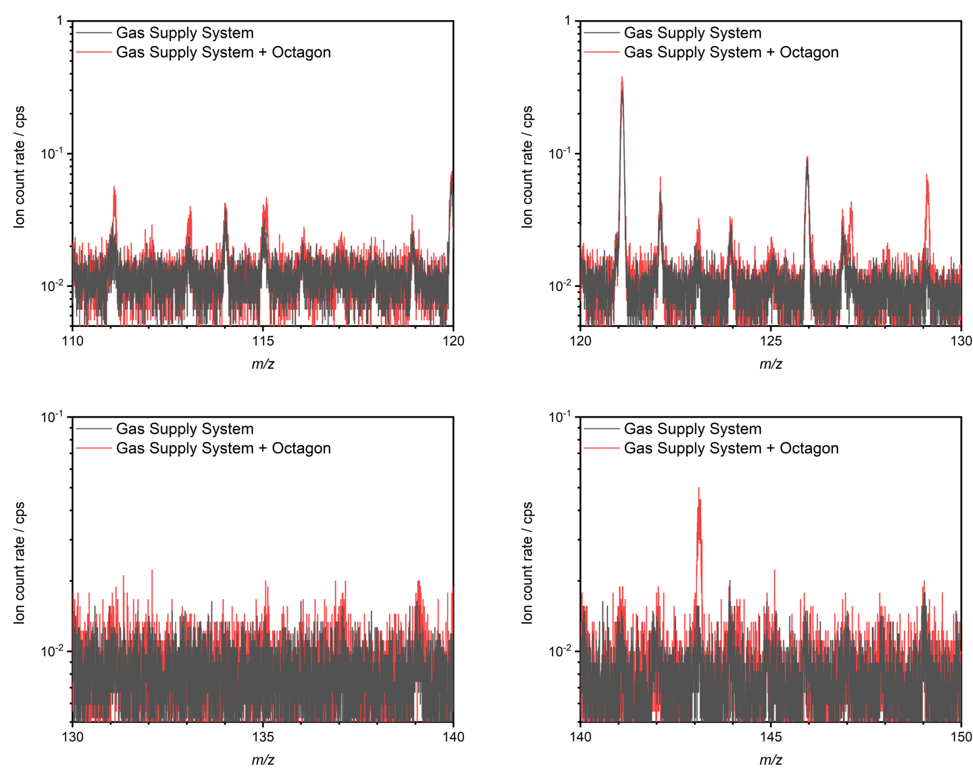

Figure 2.29: Raw data of the nitrogen gas supply only (black) and the nitrogen gas supply passing through the octagon (red) for the m/z 110–120 and 120–130 ranges (top row) and the m/z 130–140 and 140–150 ranges (bottom row).

References

[1] Adams, N.G., Smith, D., Paulson, J.F., 1980. An experimental survey of the reactions of NH_n^+ ions (n = 0 to 4) with several diatomic and polyatomic molecules at 300 K. The Journal of Chemical Physics 72, 288–297. doi:10.1063/1.438893.

[2] Aroney, M.J., Pratten, S.J., 1984. Electric birefringences and molecular anisotropic polarisabilities of benzene and of nine methylbenzenes and t-butylbenzenes. Journal of the Chemical Society, Faraday Transactions 1: Physical Chemistry in Condensed Phases 80, 1201–1204. doi:10.1039/F19848001201.

[3] Benvenuti, C., Canil, G., Chiggiato, P., Collin, P., Cosso, R., Guérin, J., Ilie, S., Latorre, D., Neil, K., 1999. Surface cleaning efficiency measurements for UHV applications. Vacuum 53, 317–320. doi:10.1016/S0042-207X(98)00364-9.

[4] Cappellin, L., Biasioli, F., Fabris, A., Schuhfried, E., Soukoulis, C., Märk, T.D., Gasperi, F., 2010. Improved mass accuracy in PTR-TOF-MS: Another step towards better compound identification in PTR-MS. International Journal of Mass Spectrometry 290, 60–63. doi:10.1016/j.ijms.2009.11.007.

[5] Chesnavich, W.J., Su, T., Bowers, M., 1980. Collisions in a noncentral field: A variational and trajectory investigation of ion-dipole capture. The Journal of Chemical Physics 72, 2641–2655. doi:10.1063/1.439409.

[6] Ennos, A.E., 1953. The origin of specimen contamination in the electron microscope. British Journal of Applied Physics 4, 101–106. doi:10.1088/0508-3443/4/4/302.

[7] Ennos, A.E., 1954. The sources of electron-induced contamination in kinetic vacuum systems. British Journal of Applied Physics 5, 27–31. doi:10.1088/0508-3443/5/1/307.

[8] Goh, Y.M., Schwartz, J., Rennich, E., Ma, T., Kerns, B., Hovden, R., 2020. Contamination of TEM Holders Quantified and Mitigated with the Open-Hardware, High-Vacuum Bakeout System. Microscopy and Microanalysis 26, 906–912. doi:10.1017/S1431927620001762.

[9] Griffiths, A.J.V., Walther, T., 2010. Quantification of carbon contamination under

electron beam irradiation in a scanning transmission electron microscope and its suppression by plasma cleaning. Journal of Physics: Conference Series 241, 3–7. doi:10.1088/1742-6596/241/1/012017.

[10] Gueneron, M., Erickson, M.H., Vanderschelden, G.S., Jobson, B.T., 2015. PTR-MS fragmentation patterns of gasoline hydrocarbons. International Journal of Mass Spectrometry 379, 97–109. doi:10.1016/j.ijms.2015.01.001.

[11] Hahn, U., Hesse, M., Remde, H., Zapfe, K., 2004. A new cleaning facility for particle-free UHV-components. Vacuum 73, 231–235. doi:10.1016/j.vacuum.2003.12.020.

[12] Hansel, A., Jordan, A., Holzinger, R., Prazeller, P., Vogel, W., Lindinger, W., 1995. Proton transfer reaction mass spectrometry: on-line trace gas analysis at the ppb level. International Journal of Mass Spectrometry and Ion Processes 149/150, 609–619. doi:10.1016/0168-1176(95)04294-U.

[13] Hansel, A., Jordan, A., Warneke, C., Holzinger, R., Wisthaler, A., Lindinger, W., 1999. Proton-transfer-reaction mass spectrometry (PTR-MS): On-line monitoring of volatile organic compounds at volume mixing ratios of a few pptv. Plasma Sources Science and Technology 8, 332–336. doi:10.1088/0963-0252/8/2/314.

[14] Harris, P.J.F., 2001. Carbonaceous contaminants on support films for transmission electron microscopy. Carbon 39, 909–913. doi:10.1016/S0008-6223(00)00195-0.

[15] Hart, R.K., Kassner, T.F., Maurin, J.K., 1970. The contamination of surfaces during high-energy electron irradiation. Philosophical Magazine 21, 453–467. doi:10.1080/14786437008238431.

[16] Haynes, W. M., E., 2017. CRC Handbook of Chemistry and Physics. 97th ed., CRC Press/Taylor Francis, Boca Raton, FL. doi:10.1201/9781315380476.

[17] Heide, H.G., 1962. Electron Microscopic Observation of Specimens under Controlled Gas Pressure. The Journal of Cell Biology 13, 147–152. doi:10.1083/jcb.13.1.147.

[18] Höflich, K., Yang, R.B., Berger, A., Leuchs, G., Christiansen, S., 2011. The direct writing of plasmonic gold nanostructures by electron-beam- induced deposition. Advanced Materials 23, 2657–2661. doi:10.1002/adma.201004114.

[19] Hoyle, D., Malac, M., Trudeau, M., Woo, P., 2011. UV Treatment of TEM/STEM Samples for Reduced Hydrocarbon Contamination. Microscopy and Microanalysis 17, 1026–1027. doi:10.1017/s1431927611006003.

[20] Hren, J.J., 1978. Specimen Contamination in Analytical Electron Microscopy: Sources and Solutions. Ultramicroscopy 3, 375–380. doi:10.1016/S0304-3991(78)80057-6.

[21] Ionicon Analytics GmbH, 2019. Ionicon User Manual PTR-MS: Hands-on.

[22] Isabell, T.C., Fischione, P.E., O'Keefe, C., Guruz, M.U., Dravid, V.P., 1999. Plasma cleaning and its applications for electron microscopy. Microscopy and Microanalysis 5, 126–135. doi:10.1017/S1431927699000094.

[23] Khan, M.H., Casillas, G., Mitchell, D.R., Liu, H.K., Jiang, L., Huang, Z., 2016. Carbon- and crack-free growth of hexagonal boron nitride nanosheets and their uncommon stacking order. Nanoscale 8, 15926–15933. doi:10.1039/c6nr04734c.

[24] Konings, S.J.P., Kujawa, S., Trompenaars, P.H.F., 2017. Method of studying a sample in an ETEM , Patent No. US 9,658,246 B2.

[25] Lee, J.Y., Yun, T.S., Santamarina, J.C., Ruppel, C., 2007. Observations related to tetrahydrofuran and methane hydrates for laboratory studies of hydrate-bearing sediments. Geochemistry, Geophysics, Geosystems 8, 1–10. doi:10.1029/2006GC001531.

[26] Maleknia, S.D., Bell, T.L., Adams, M.A., 2007. PTR-MS analysis of reference and plant-emitted volatile organic compounds. International Journal of Mass Spectrometry 262, 203–210. doi:10.1016/j.ijms.2006.11.010.

[27] McGilvery, C.M., Goode, A.E., Shaffer, M.S.P., McComb, D.W., 2012. Contamination of holey/lacey carbon films in STEM. Micron 43, 450–455. doi:10.1016/j.micron.2011.10.026.

[28] Middleman, K.J., Herbert, J.D., Reid, R.J., 2007. Cleaning stainless steel for use in accelerators-Phase 1. Vacuum 81, 793–798. doi:10.1016/j.vacuum.2005.11.057.

[29] Mitchell, D.R.G., 2015. Contamination mitigation strategies for scanning transmission electron microscopy. Micron 73, 36–46. doi:10.1016/j.micron.2015.03.013.

[30] Norman, M., Hansel, A., Wisthaler, A., 2007. O2+ as reagent ion in the PTR-MS instrument: Detection of gas-phase ammonia. International Journal of Mass Spectrometry 265, 382–387. doi:10.1016/j.ijms.2007.06.010.

[31] Salazar Gómez, J.I., Klucken, C., Sojka, M., Masliuk, L., Lunkenbein, T., Schlögl, R., Ruland, H., 2019. Elucidation of artefacts in proton transfer reaction time-of-flight mass spectrometers. Journal of Mass Spectrometry 54, 987–1002. doi:10.1002/jms.4479.

[32] Salazar Gómez, J.I., Sojka, M., Klucken, C., Schlögl, R., Ruland, H., 2021. Determination of trace compounds and artifacts in nitrogen background measurements by proton transfer reaction time-of-flight mass spectrometry under dry and humid conditions. Journal of Mass Spectrometry 56, 1–22. doi:10.1002/jms.4777.

[33] Soong, C., Woo, P., Hoyle, D., 2012. Contamination Cleaning of TEM/SEM Samples with the ZONE Cleaner. Microscopy Today 20, 44–48. doi:10.1017/s1551929512000752.

[34] van Tendeloo, G., Dyck, D., Pennycook, S., 2012. Sample preparation techniques for transmission electron microscopy, in: van Tendeloo, G. (Ed.), Handbook of Nanoscopy. Viley-VCH, Weinheim, pp. 473–498. doi:10.1007/978-1-4939-8935-5_33.

[35] Vig, J., Le Bus, J., 1976. UV / Ozone of Surfaces. IEEE Transactions on Parts, Hybrids, and Packaging 12, 365–370. doi:10.1116/1.573115.

[36] Was, G.S., Taller, S., Jiao, Z., Monterrosa, A.M., Woodley, D., Jennings, D., Kubley, T., Naab, F., Toader, O., Uberseder, E., 2017. Resolution of the carbon contamination problem in ion irradiation experiments. Nuclear Instruments and Methods in Physics Research, Section B: Beam Interactions with Materials and Atoms 412, 58–65. doi:10.1016/j.nimb.2017.08.039.

[37] Wu, J., Shan, H., Chen, W., Gu, X., Tao, P., Song, C., Shang, W., Deng, T., 2016. In Situ Environmental TEM in Imaging Gas and Liquid Phase Chemical Reactions for Materials Research. Advanced Materials 28, 9686–9712. doi:10.1002/adma.

201602519.

3 Carbon contamination in TEM caused by organic solvents utilized for sample preparation

3.1 Abstract

In the field of transmission electron microscopy (TEM), one crucial requirement for achieving high-quality measurements is the cleanliness of the sample. As many samples either are prepared in organic solvents or need to be dispersed in such for applying them on the sample grids, solvent residues might get reduced by the electron beam, resulting in carbon contamination accumulated on the specimen's surface. However, microscopists are often limited in their choice of solvent, which needs to be compatible with the sample itself, and therefore the sample preparation needs to be customized based on the specimen's properties.

Here we show how contamination in TEM is influenced by the type of solvent, the drying time of the sample and the time that the sample remains in the microscope for solvents commonly used either in chemical synthesis or TEM sample preparation. Using thickness measurements by electron energy loss spectroscopy (EELS), we were able to quantify carbon contamination resulting from different solvents. Depending on properties of the solvents, e.g., the vapor pressure, a trend regarding the accumulated contamination could be observed. The specimen's drying time before sample insertion and the impact of outgassing in the low-pressure environment within the microscope on residual contaminants were investigated and compared. Our study allows us to carefully reassess the cleanliness of a sample based on its preparation parameters and gives us guidance on the choice of

solvents for achieving clean TEM data with low amounts of contamination.

3.2 Introduction

TEM has become an indispensable tool in the characterization of a wide variety of samples, providing insight into the composition of a sample down to the atomic scale. Despite being able to achieve a good resolution [24,37], there are various obstacles that make the investigation of specimens challenging [6,7,8,21]. One of these is the formation of carbon contamination. Already in the early stages of electron microscopy, the accumulation of amorphous carbon on sample surfaces was documented [9,10,17,19], often linked to oil-diffusion pumping systems [15,27,32]. Though vacuum techniques have been improved, issues with carbon contamination are still common nowadays and a well-documented problem in current research areas like material science [43,44] or in life science [11,13]. Also, advanced TEM techniques, e.g., methods used for in-situ characterization like environmental TEM [31,41] or liquid cell approaches [42], are impaired by contamination affecting the experiments.

The vacuum in the microscope is highly sensitive to outgassing contaminants, e.g., of water or carbonaceous molecules, because these can impair the vacuum quality and result effectively in a decrease of resolution due to interactions between the electron beam and the volatile organic components (VOCs). On the TEM grid, these VOCs can be reduced by the electron beam, leading to the formation of a layer of amorphous carbon on the surface of the investigated sample. The deposition of carbon on the sample increases the thickness of the sample environment and results in a degradation of the quality of the obtained image and of the spectroscopic information [2,4]. Different potential sources can lead to contamination: While the sample itself is the main contributor due to organic ligands or solvent residues from synthesis [23], the used equipment (e.g., tweezers, grids, sample holders) might also decrease the vacuum quality [12,28].

Adding solvent to a sample can be necessary for several different reasons: For example,

samples consisting of nanoparticles can form agglomerates that are too large for TEM investigation, so the preparation relies on dispersing the sample in an organic solvent for sonication, which can separate these agglomerates, resulting in a good dispersion of the particles on the TEM grid [3,33,34]. Other applications of solvents for sample preparation are utilized for adhering fine particles that otherwise do not stick to the carbon film of the grid, or for preparing samples for in-situ experiments if a closed-cell approach for is chosen. For dispersing the particles, a suitable solvent can be used that is compatible with the sample's properties [1,39].

For attaining high-quality data, it is necessary to optimally remove the solvent to prevent contamination of the areas of interest and keep the microscope environment as clean as possible by mitigating outgassing. For this reason, thoughtful selection of the solvent and careful planning of preparation parameters form an integral part of TEM investigations. Though there are several established mitigation techniques that can either prevent contamination or remove it once it has formed [14,19,35], measures taken during the sample preparation itself have been rarely discussed.

In this work, we focus on how to improve the preparation of TEM samples that employ organic solvents. We compared the accumulated carbon contamination accompanying the use of different organic solvents for the sample preparation. Also, the impact of the drying time of samples and the duration a sample spent inside the microscope on the carbon contamination was investigated. In addition, it is discussed how the purity regarding the water content of solvents affects the contamination in TEM experiments, as some solvents show hygroscopic properties. The amount of accumulated contamination was quantitatively analyzed using EELS for determining the local thickness of the samples. The results of our experiments can be applied to the preparation of TEM samples dispersed in solution with the goal to achieve clean, high quality data despite using organic solvents and to mitigate carbon contamination and solvent outgassing in the microscope.

3.3 Methods

All experiments were performed using a Thermo Scientific Talos F200X operated in STEM mode with an acceleration voltage of 200 kV. The scanned area in which contamination built up had 500×500 pixel^2, which corresponds to a size of 173×173 nm^2 and each pixel was exposed with a dwell time of 2 µs with a beam current of approximately 200 pA. To increase the beam exposure duration, for each set of measurements, ten different exposure times in the range between 5 s and 480 s were chosen consecutively. All experiments were performed on commercially available holey carbon grids (Cu, 400 mesh, Plano-EM) with a carbon film thickness of approximately 22 nm. For preparing a sample, 1 µL of solvent was applied to a grid and dried at ambient pressure before insertion into the TEM. The drying times between application of the solvent on the grid and insertion of the sample holder into the TEM were 10 and 30 min, respectively. All solvents were dried by a molecular sieve and distilled before the measurements, unless stated otherwise. In this work, we compare the impact of different solvents regarding the contamination accumulated when exposed to an electron beam. On the one hand, we studied solvents used in synthesis, namely tetrahydrofuran (THF) and toluene, while on the other hand the alcohols methanol (MeOH), ethanol (EtOH) and isopropanol (iPrOH) were examined, which are often used as solvents of choice by electron microscopists. For all contamination measurements, the thickness of the carbon film in the close vicinity of the sample was subtracted from the total thickness as the background. This allows us to take into account that the carbon film may vary in thickness and morphology across the grid.

The thickness of the contaminated area was measured by EELS with a Gatan Continuum S spectrometer. EELS data analysis is based on the log-ratio technique discussed in the literature[26] and based on eq. (3.1) with d being the local thickness, λ the inelastic mean free path, I_t the total area and I_0 the zero-loss area under the electron energy loss spectrum.

$$d = \lambda \ln \frac{I_t}{I_0} \tag{3.1}$$

While I_t and I_0 can be determined from the measured EELS spectra, λ is estimated based on microscope parameters, i.e., the acceleration voltage and the collection angle, and the mean atomic number of the local sample composition.

In general, these calculations are limited to thin specimens, as otherwise electron-specimen interactions lead to plural scattering energy loss interactions and result in a diminishing intensity of the zero-loss peak. In order to calculate the thickness of a sample, the inelastic mean free path, which depends on the atomic composition of the sample, has to be determined. Based on energy-dispersive X-ray spectroscopy, we found that for all areas the contamination consisted of at least 95% carbon along with small traces mostly consisting of oxygen and nitrogen. When considering 5% of these other elements in the inelastic mean free path calculations, the value deviates by less than 1% from the value obtained for pure carbon. Therefore, as an approximation, it was assumed for thickness calculations that the contamination only contained carbon and we did not take into account the chemical composition of the solvents before these were reduced by the electron beam. Thickness calculations were based on the GMS DigitalMicrograph plugin "Mean Free Path Estimator" developed by Dave Mitchell[29]. As the inelastic mean free path of the contamination is calculated based on approximations[26], the errors for all EELS thickness calculations were assumed to be of order 10%[5].

Due to the scanning properties of the microscope in STEM mode, contamination does not only accumulate in the scanned area, but also as a result of the electron beam movement pattern outside of the scanned area, as shown in fig. 3.1 for the example of a grid contaminated with iPrOH.

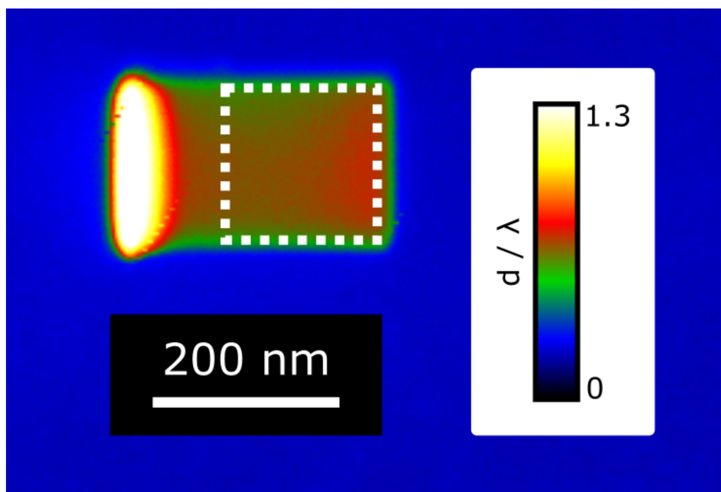

Figure 3.1: Carbon contamination of a grid prepared with 1 µL iPrOH and dried for 30 min before insertion into the microscope. The scanned area (white dashed square) was exposed to the electron beam for 300 s before EELS data acquisition.

For all thickness measurements, all of the contamination built up on the grid during electron beam exposure is considered in the evaluation, i.e., also the contamination outside of the scanned area is included. As solvent molecules diffuse towards the electron beam with an increasing beam exposure duration, the accumulated contamination, d, follows a parabolic rate law described by eq. (3.2)[30].

$$d = K_p\sqrt{t} + c \tag{3.2}$$

While the carbon film is exposed to the electron beam, the amount of contamination, d, grows proportional to the square root of the time t where K_p is the parabolic rate constant and c a measurement-specific constant. Contamination growth has been described as a diffusion-driven process, in which VOCs slowly move towards the exposed area[18,36,38], although contradictory observations have also been reported[22].

This behaviour seems to be induced by solvent molecules, as this trend was not observed for contamination accumulated on the carbon film of otherwise empty TEM grids[20].

When the data is fitted by eq. (3.2), the fit function intersects with the abscissa at a time at which diffusion effects start to contaminate the area, while at earlier times mostly only contaminants already present in the exposed area get reduced. As we determine the total contamination volume in nm^3, instead of just the local thickness, the value of K_p is given in $\frac{nm^3}{\sqrt{t}}$ and c is given in nm^3. Fit parameters and fit functions of all data are included in the supporting information.

3.4 Results and discussion

In the following sections, we discuss the contamination caused by different solvents with a focus on the drying time of the sample and the impact of the sample's duration in the TEM. Furthermore, we analyse the impact of the solvent's purity regarding its water content, as some solvents show hygroscopic behaviour.

3.4.1 Carbon contamination depending on the solvent

For investigating the contamination resulting from different solvents, the grids were prepared and dried for 30 min before inserting them into the TEM and exposing them to the electron beam. While for all samples a higher exposure time lead to more contamination, the overall duration varies depending on the solvent (fig. 3.2). For the sample prepared with THF, the least amount of contamination was observed. Slightly more contamination was observed for the alcohols: Contamination of grids prepared with methanol and ethanol was very similar and less than the contamination by isopropanol. Toluene lead by far to the most contamination, with the amount of deposited carbon being orders of magnitude higher than for the other solvent samples.

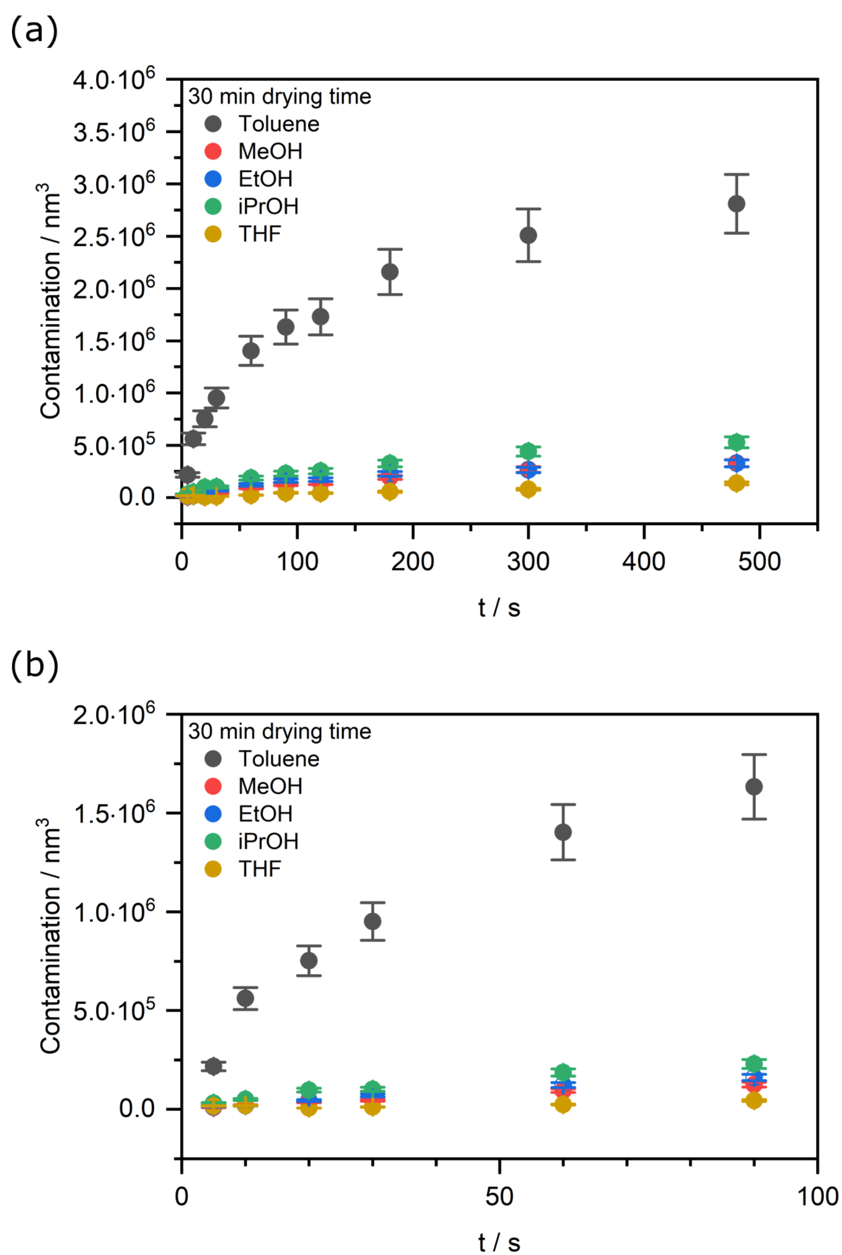

Figure 3.2: Carbon contamination accumulated by electron beam exposure of different solvents. All samples were dried for 30 min before inserting the specimens into the microscope. The whole range of exposure times in shown in (a), with the exposure times up to 100 s shown enlarged in (b).

The different physical properties of the solvents contribute to the differences in the amount

of accumulated carbon following their deposition. Comparing the solvents, higher contamination amounts were observed with a decreasing vapor pressure and an increasing boiling point, values for which are listed in table 3.1 for 25 °C and 101.325 kPa, respectively. It must be taken into account that the conditions in the TEM strongly deviate from standard conditions, i.e., the pressure in the TEM is significantly lower and electron beam exposure results in sample heating[8]. Despite these differences under experimental conditions, we observe that the amount of accumulated contamination for the different solvents is in agreement with the trend of the parameters of the solvents described above, as a contaminant molecule's lower volatility makes is less mobile so that it remains longer on the TEM grid.

Solvent	Vapor pressure/kPa	Boiling point/°C
THF	21.6	66
MeOH	16.9	65.4
EtOH	7.87	78.24
iPrOH	6.02	82.21
Toluene	3.79	110.6

Table 3.1: Vapor Pressure at 25 °C and boiling point at 101.325 kPa of the solvents used in the experiments[16].

For all solvents, longer electron beam exposure times result in more contamination, following a parabolic rate behaviour, which is in agreement with previous studies[30] and supports other observations of diffusion-driven contamination growth[18,36,38]. This applies even though we compare the total contamination volume instead of the thickness in the inner part of an area contaminated by the electron beam, as investigated by Mitchell[30]. The fitted data and fit parameters for each measurement are given in the supporting information in fig. 3.9, fig. 3.10 and fig. 3.11, and in table 3.2.

3.4.2 Comparing different drying times before sample insertion

When preparing a liquid TEM sample, e.g., a sample dispersed in solvent, it is crucial to let the sample dry before inserting it into the microscope in order to keep the vacuum environment clean. In fig. 3.3 the accumulated contamination of different solvents for samples dried for 30 min (filled circles) and 10 min (open circles), respectively, are compared. For toluene, only the data for the sample dried for 30 min is shown because after 10 min the grid was not yet dry enough for mounting the sample in the sample holder.

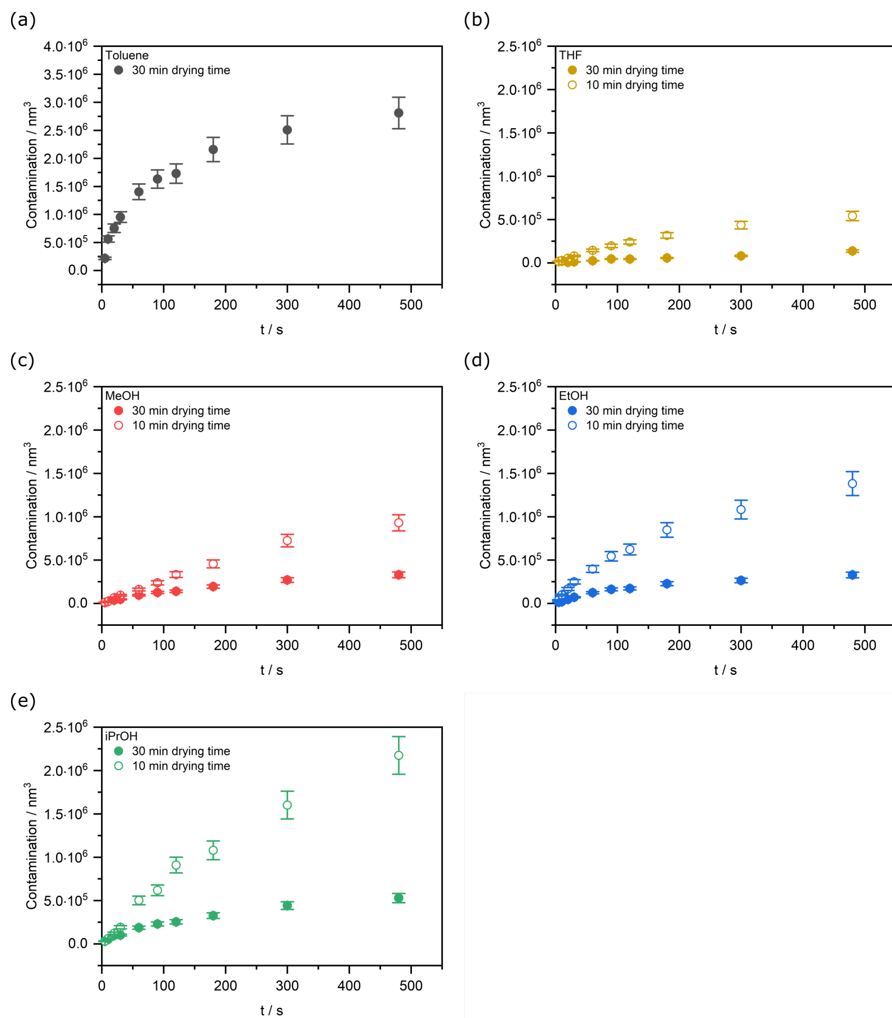

Figure 3.3: Comparison of contamination accumulated by solvent samples dried for 10 min (open circles) and 30 min (filled circles), respectively.

For all solvents, significantly more contamination was observed when the samples were dried only for 10 min instead of 30 min. When comparing the amount of carbon contamination emerging between 60 s and 480 s of exposure time, i.e., in the time range, during which diffusion of solvent molecules has a relevant impact on the amount of contamination, the contamination was between 2.2 times (MeOH) and 5.1 times (THF) higher for a drying time of 10 min compared to 30 min. Our measurements indicate that for mitigating contamination, a longer drying time of the specimens prepared with organic solvents results in reduced carbon contamination.

3.4.3 Long-term outgassing of samples in the TEM

While the results discussed in section 3.4.2 show the impact of the drying time outside of the microscope, the impact of sample outgassing within the microscope is discussed here. As the differences in accumulated contamination depending on the solvent indicate, there are still contaminants adsorbed on the grid surface after 30 min of drying time. How much contamination was accumulated immediately after sample insertion into the TEM and after the sample remained for 30 min in the microscope is illustrated by fig. 3.4. The pressure in the TEM octagon is of the order of 10^{-7} mbar, which generally should allow for fast VOC removal.

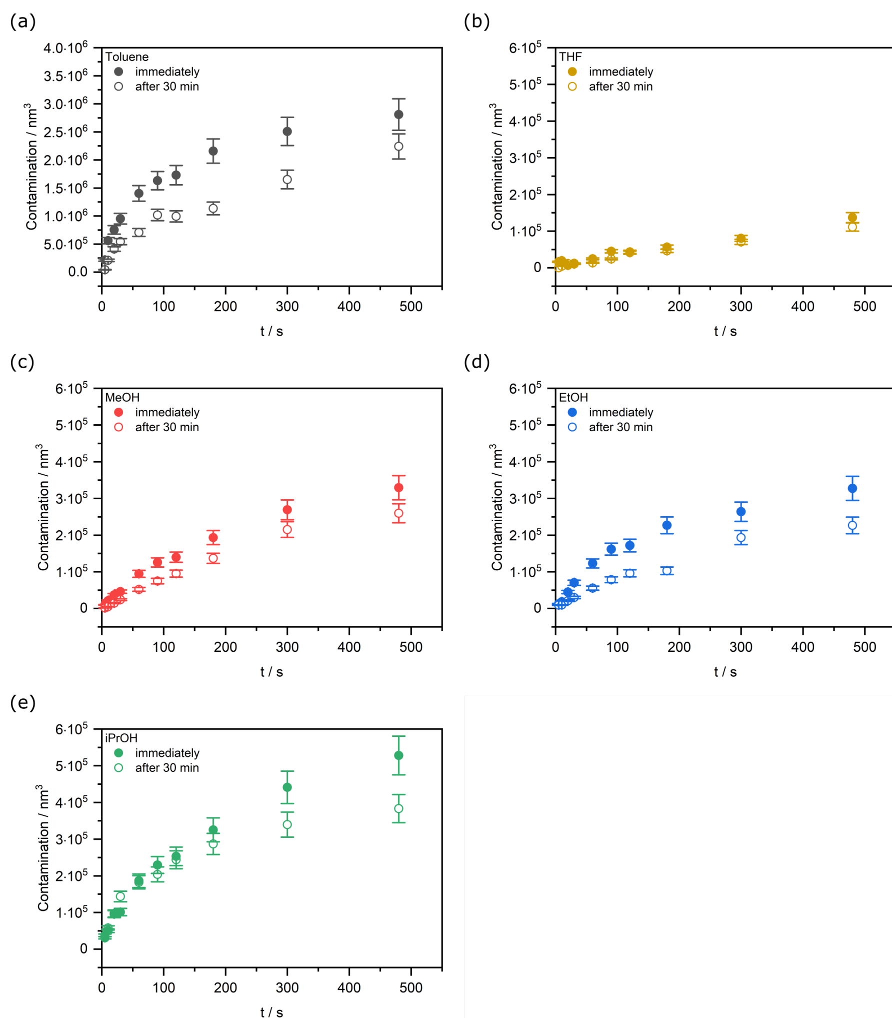

Figure 3.4: Contamination resulting from solvent samples dried for 30 min before TEM investigation immediately after sample insertion (filled circles) and 30 min later (empty circles).

For all samples, less contamination was found for specimens that remained for a longer time in the microscope environment. However, the impact of 30 min TEM vacuum on the amount of contamination appears to be quite small, considering the low pressure in the TEM octagon. The restricted spatial setup dimensions, e.g., the small pole piece gap or the apertures, slow pumping of the VOCs down and, instead, the outgassing contaminants remain in the direct environment of the TEM grid.

In order to compare contaminant removal by the TEM vacuum on the one hand and by

drying the samples beforehand outside of the microscope on the other hand, a comparison of the accumulated contamination is shown for the example of MeOH in fig. 3.5. The data for the other solvents and figures displaying the first 100 s of exposure time enlarged are included in the supporting information in fig. 3.12 and fig. 3.13.

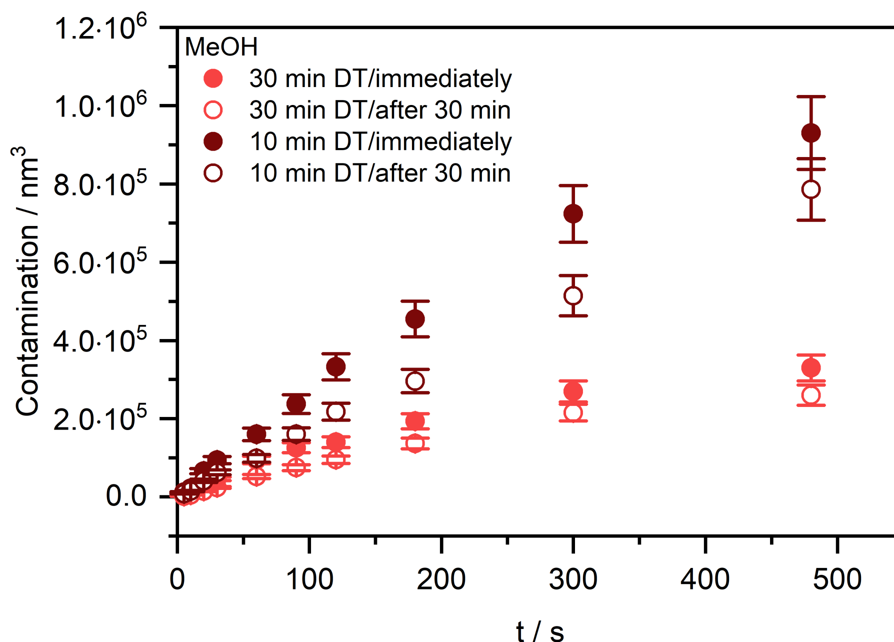

Figure 3.5: Contamination of MeOH samples dried for either 10 min or 30 min at ambient pressure immediately and 30 min after inserting the sample into the TEM.

The time elapsed between the sample dried for 10 min and measured after 30 min in the TEM (dark red open circles) and the sample dried for 30 min and measured immediately after insertion (light red filled circles) is in a comparable range. Despite the similar time passed since the solvent was applied, the contamination of the sample dried for 10 min was more than twice higher. The same trend was observed for the other solvents as well, as shown in the supporting information in fig. 3.13.

Based on the parabolic rate fit, the time at the abscissa intersect can be interpreted as the incubation period, after which stable thermodynamic conditions are achieved that

initiate the diffusion processes[30]. For all measurements, the onset of solvent diffusion commenced earlier than 20 s, so beam exposure times of 5 s and 10 s are excluded hereafter when comparing the average difference between measurements and only data for electron exposure times between 20 s and 480 s are taken into account. The results presented below compare contamination accumulated in different measurement sets. The displayed value is the mean value of all measurements comparing the contamination from equal exposure times.

When comparing the difference in accumulated concentration between a drying time of 10 min with that for 30 min, both at ambient pressure (fig. 3.6), a significant decrease between 52.7% and 80.7% can be observed for the solvents.

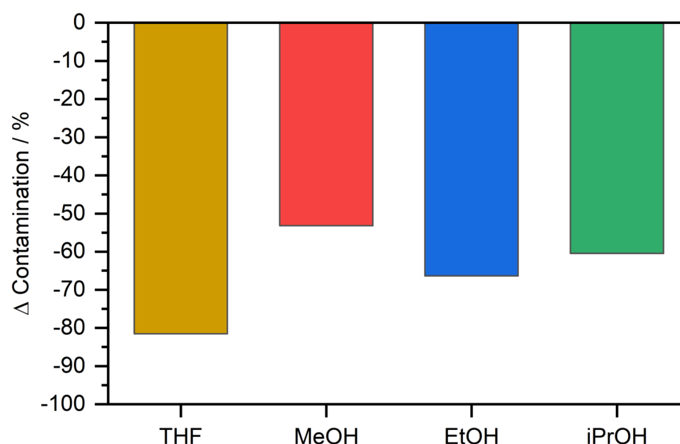

Figure 3.6: Difference in accumulated contamination when comparing a sample with a drying time of 30 min to a sample dried for 10 min.

The difference in accumulation for samples remaining for different times in the vacuum of the TEM is shown in fig. 3.7 for (a) 10 min and (b) 30 min drying time before sample insertion. Longer vacuum exposure leads to less contamination accumulated for all solvents.

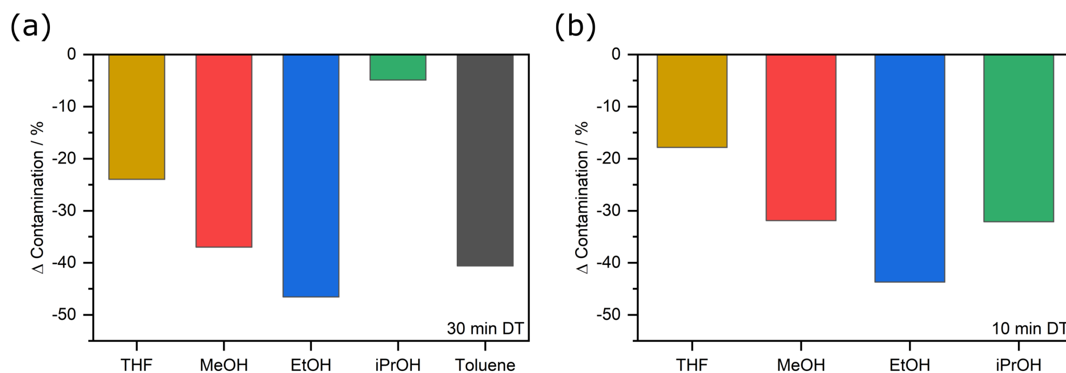

Figure 3.7: Difference in accumulated contamination between a sample remaining 30 min in the microscope and a sample measured immediately after insertion into the TEM. The drying times of the samples were either (a) 10 min or (b) 30 min, respectively, before insertion.

3.4.4 Wet Solvents

In this section, the impact of the water content of solvents is studied by investigating samples of MeOH and EtOH that were not dried by a molecular sieve before TEM experiments. According to the manufacturer's data sheets, the water content of MeOH was $\leq 0.1\%$ and of EtOH $\leq 0.2\%$, though both containers were already open for an extended time before the samples were analyzed, resulting in an increased water content due to the alcohols' hygroscopic properties. All samples were dried for 30 min before they were inserted into the TEM and exposed for different durations to the electron beam. The accumulated contamination is shown in fig. 3.8. For both wet solvents, the sample thickness was orders of magnitude higher than that of solvents dried beforehand, which made EELS with exposure times longer than 90 s (EtOH) and 120 s (MeOH), respectively, prohibitively.

Data comparing contamination for all exposure times is included in the supporting information in fig. 3.14. Though the atomic fraction of carbon is lower in an alcohol-water azeotrope compared to the pure associated alcohol, different sample properties were observed, which means that these mixed-phase droplets have an increased drying time[25,40].

We can conclude, that in TEM experiments, it is crucial that the solvent contains as little water as possible to, first, minimize the overall accumulated contamination and, second, to mitigate undesired interactions between water molecules and the sample itself.

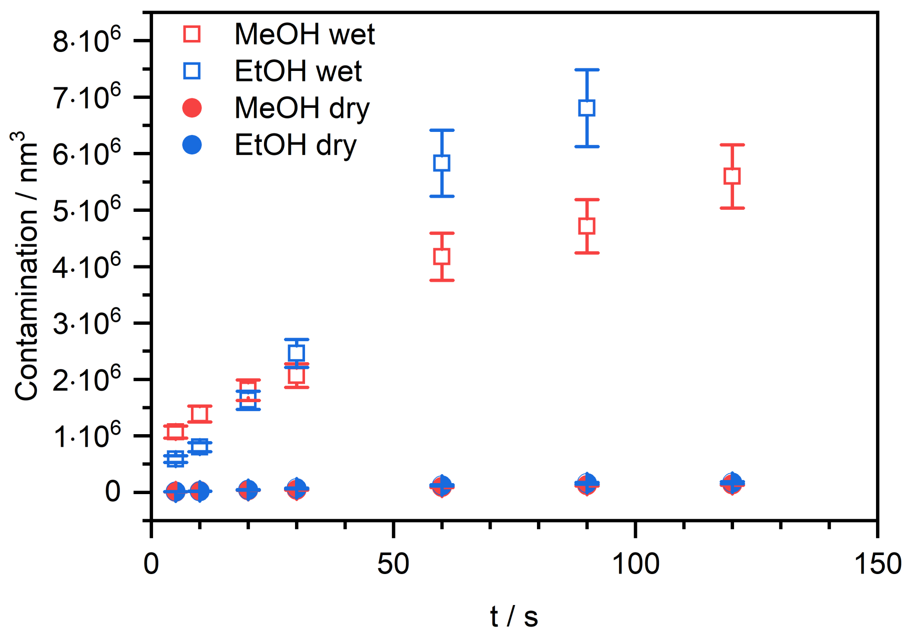

Figure 3.8: Accumulated contamination from wet (squares) and dry (dots) solvent samples of MeOH and EtOH dried for 30 min before sample insertion.

3.5 Conclusions

Carbon contamination in transmission electron microscopy can be caused by exposing residues of organic solvents to an electron beam. We have analyzed the amount of carbon contamination depending on the type of solvent used and could observe that more volatile solvents caused a lower degree of contamination. In addition, an increased drying time led to a reduced thickness of the contamination layer accumulated during the electron beam exposure. Though contaminants were also removed in the vacuum of the TEM while the sample was inserted into the microscope, the amount of contamination only decreased

slowly when the samples remained longer in the microscope. This indicates that the VOCs remained in the close neighborhood of the sample due to the spatial restrictions in the octagon. The quality of the solvent, i.e., its purity regarding water content, also has an influence on the accumulated contamination. Not only may the water included in the solvent interact with the sample, but it also decreases the evaporation speed of the solvent, requiring longer drying times to prevent contamination. Overall, it is crucial to carefully reassess the TEM specimen preparation if the sample requires to be dispersed in a solvent. The drying time should be long enough to assure that residual solvent molecules can evaporate before inserting the sample into the TEM, as the contaminants remain for a long time in the low-pressure environment. When comparing the solvents THF, MeOH, EtOH, iPrOH and toluene, the accumulated contamination increased with a higher boiling point and a lower vapor pressure. Based on our results, THF and MeOH are the most favourable solvents, considering our experimental conditions. In contrast, the use of toluene results in high amounts of contamination and requires a different sample preparation, e.g., a longer drying time. While we only investigated a small set of different solvents, we believe that these results can be applied to other solvents as well. Taking measures for minimizing contamination not only improves the measurement quality, but also benefits the status of the microscope by keeping it free from contaminants as well as possible.

3.6 Supporting Information

Parabolic rate fit parameters

For all measurements, the coefficient of determination R^2 regarding the parabolic rate behaviour of the accumulated contamination was determined (Table 3.2).

Solvent	Drying time	Time in microscope until measurement	$K_{p,V}$ / $\frac{nm^3}{\sqrt{t}}$	c_V / nm^3	R^2
THF	10 min	immediately	27939	-63769	0.9971
	10 min	30 min	23952	-60483	0.9954
	30 min	immediately	5910	-12719	0.9091
	30 min	30 min	5362	-12719	0.9565
MeOH	10 min	immediately	48363	-162101	0.9802
	10 min	30 min	38409	-149434	0.9489
	30 min	immediately	16925	-36242	0.9955
	30 min	30 min	13981	-46613	0.9845
EtOH	10 min	immediately	69692	-128148	0.9984
	10 min	30 min	47861	-89127	0.9927
	30 min	immediately	16672	-18334	0.9809
	30 min	30 min	11675	-30068	0.9759
iPrOH	10 min	immediately	111724	-345545	0.9899
	10 min	30 min	68250	-208292	0.9637
	30 min	immediately	25978	-25550	0.9957
	30 min	30 min	17942	24821	0.9640
Toluene	30 min	immediately	131079	211708	0.9593
	30 min	30 min	103864	-103367	0.9835

Table 3.2: Fit parameters $K_{p,V}$ and c_V as well as coefficient of determination R^2 for the fit of the contamination following a parabolic law behaviour of the different solvent samples.

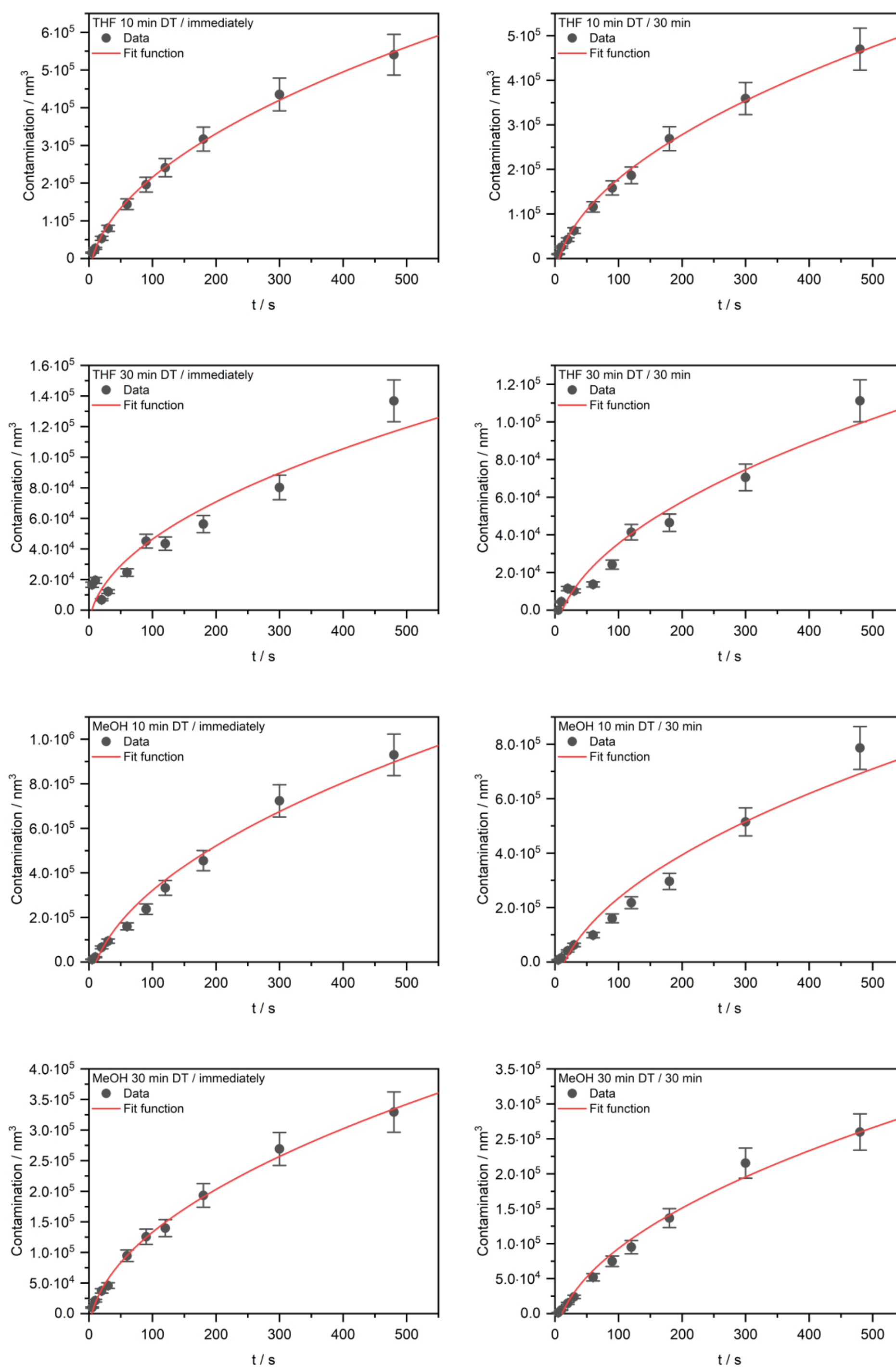

Figure 3.9: Data (dots) and parabolic rate fit (red line) of the solvents THF and MeOH for different drying times (DT) and times remaining in the microscope.

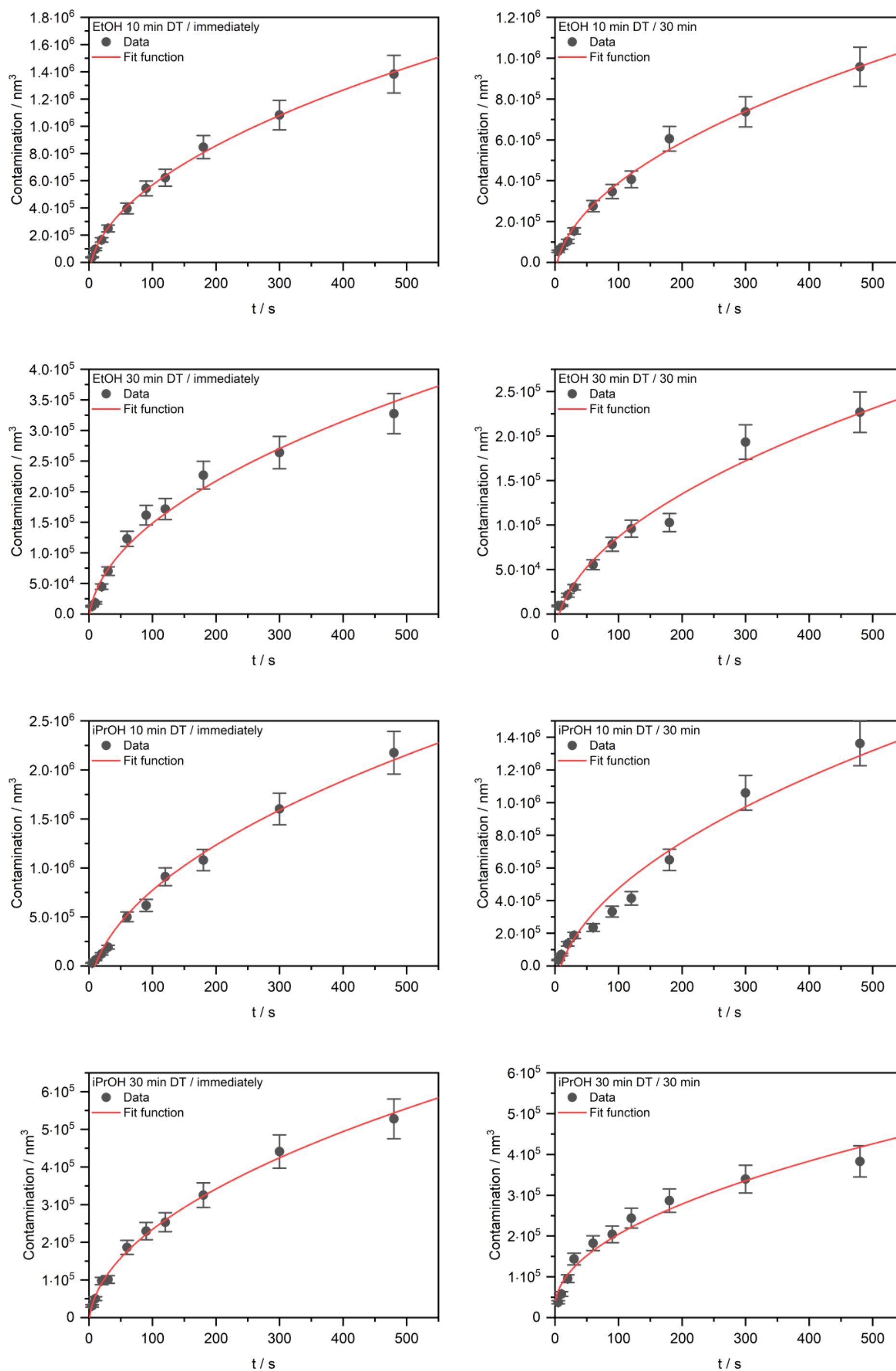

Figure 3.10: Data (dots) and parabolic rate fit (red line) of the solvents EtOH and iPrOH for different drying times (DT) and times remaining in the microscope.

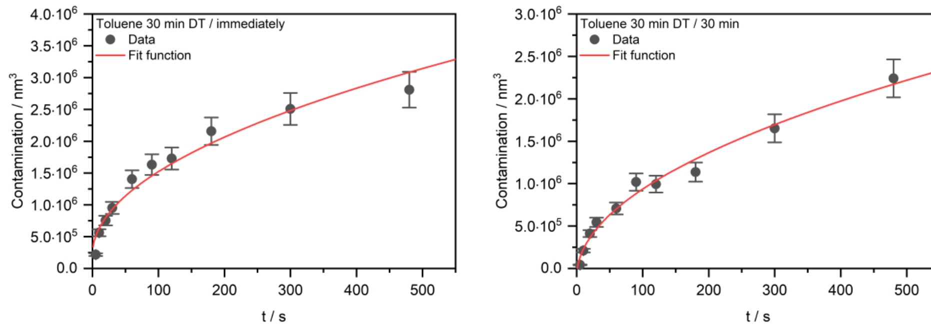

Figure 3.11: Data (dots) and parabolic rate fit (red line) of the solvent toluene for different times remaining in the microscope.

Overview of all measurements for each solvent

The data comparing measurements with different drying and dwell times in the microscope of the solvents are shown in fig. 3.12 and fig. 3.13. All collected data is shown on the left side in (a), while on the right side, the data of the first 100 s of exposure time is shown in (b).

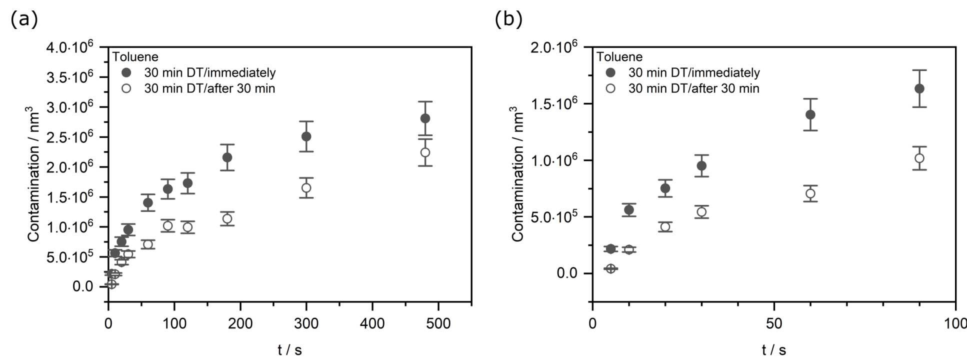

Figure 3.12: Data of all toluene measurements (a), with the first 100 s of beam exposure time shown enlarged in (b).

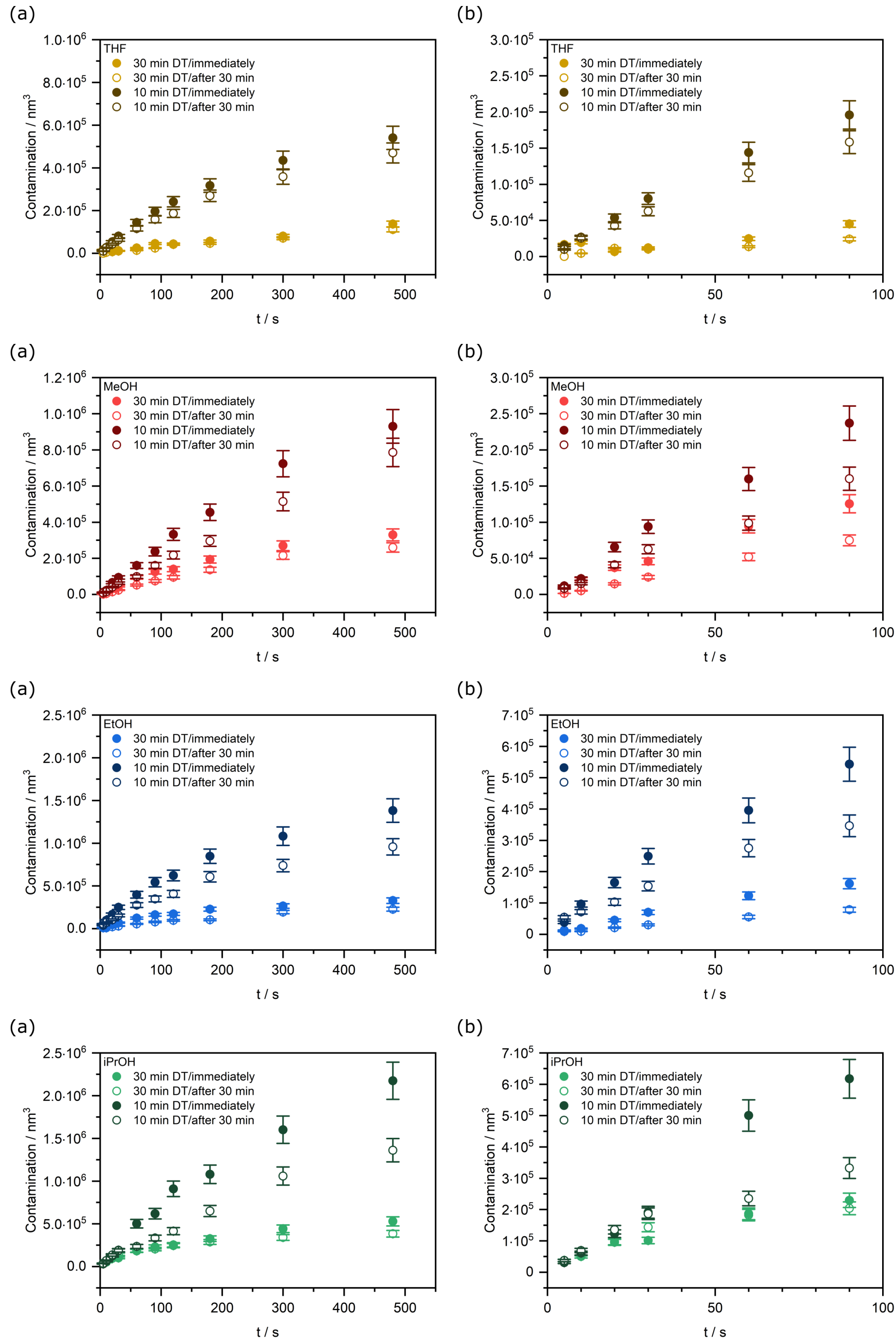

Figure 3.13: Data of all THF, MeOH, EtOH and iPrOH measurements (a), with the first 100 s of beam exposure time shown enlarged in (b).

Measurements of wet solvents

In fig. 3.14, all exposure times of the dry solvent are compared to the contamination accumulated for solvents containing water. No contamination volume could be determined for MeOH with exposure times longer than 120 s and for EtOH with exposure times longer than 90 s due to the high thickness.

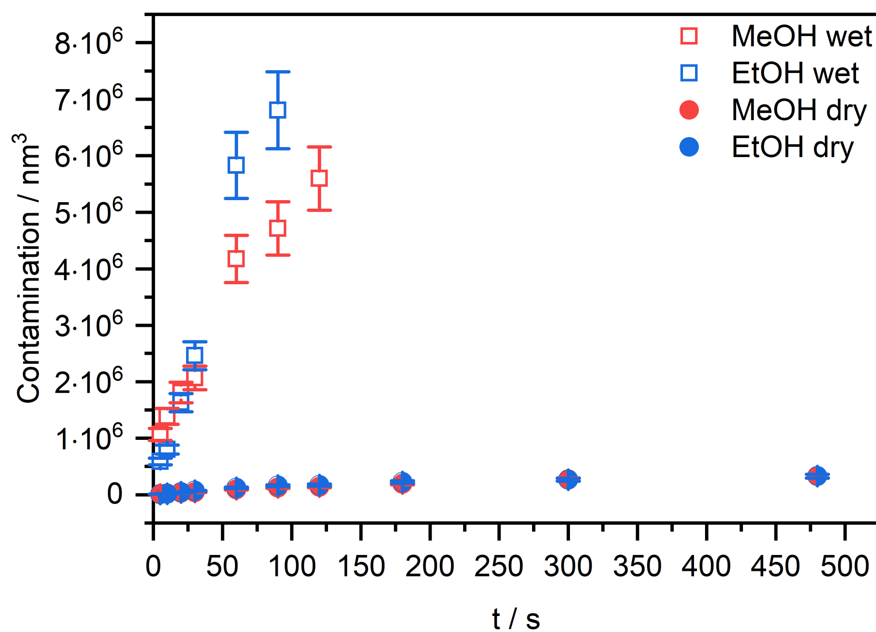

Figure 3.14: Accumulated contamination from wet (squares) and dry (dots) solvent samples of MeOH and EtOH dried for 30 min before sample insertion.

References

[1] Byrne, F.P., Jin, S., Paggiola, G., Petchey, T.H.M., Clark, J.H., Farmer, T.J., Hunt, A.J., McElroy, C.R., Sherwood, J., 2016. Tools and techniques for solvent selection: green solvent selection guides. Sustainable Chemical Processes 4, 1–24. doi:10.1186/s40508-016-0051-z.

[2] De Jonge, N., Verch, A., Demers, H., 2018. The Influence of Beam Broadening on the Spatial Resolution of Annular Dark Field Scanning Transmission Electron Microscopy. Microscopy and Microanalysis 24, 8–15. doi:10.1017/S1431927618000077.

[3] Dieringa, H., 2018. Processing of magnesium-based metal matrix nanocomposites by ultrasound-assisted particle dispersion: A review. Metals 8. doi:10.3390/met8060431.

[4] Drees, H., Müller, E., Dries, M., Gerthsen, D., 2018. Electron-beam broadening in amorphous carbon films in low-energy scanning transmission electron microscopy. Ultramicroscopy 185, 65–71. doi:10.1016/j.ultramic.2017.11.005.

[5] Egerton, R.F., 2011. Electron Energy-Loss Spectroscopy in the Electron Microscope. 3rd ed., Springer US, New York. doi:10.1007/978-1-4419-9583-4.

[6] Egerton, R.F., 2012. Mechanisms of radiation damage in beam-sensitive specimens, for TEM accelerating voltages between 10 and 300 kV. Microscopy Research and Technique 75, 1550–1556. doi:10.1002/jemt.22099.

[7] Egerton, R.F., 2013. Control of radiation damage in the TEM. Ultramicroscopy 127, 100–108. doi:10.1016/j.ultramic.2012.07.006.

[8] Egerton, R.F., Li, P., Malac, M., 2004. Radiation damage in the TEM and SEM. Micron 35, 399–409. doi:10.1016/j.micron.2004.02.003.

[9] Ennos, A.E., 1953. The origin of specimen contamination in the electron microscope. British Journal of Applied Physics 4, 101–106. doi:10.1088/0508-3443/4/4/302.

[10] Ennos, A.E., 1954. The sources of electron-induced contamination in kinetic vacuum systems. British Journal of Applied Physics 5, 27–31. doi:10.1088/0508-3443/5/1/307.

[11] Fernandez, J.J., Laugks, U., Schaffer, M., Bäuerlein, F.J.B., Khoshouei, M., Baumeister, W., Lucic, V., 2016. Removing Contamination-Induced Reconstruction Artifacts from Cryo-electron Tomograms. Biophysical Journal 110, 850–859. doi:10.1016/j.bpj.2015.10.043.

[12] Goh, Y.M., Schwartz, J., Rennich, E., Ma, T., Kerns, B., Hovden, R., 2020. Contamination of TEM Holders Quantified and Mitigated with the Open-Hardware, High-Vacuum Bakeout System. Microscopy and Microanalysis 26, 906–912. doi:10.1017/S1431927620001762.

[13] Grassucci, R.A., Taylor, D.J., Frank, J., 2007. Preparation of macromolecular complexes for cryo-electron microscopy. Nature Protocols 2, 3239–3246. doi:10.1038/nprot.2007.452.

[14] Griffiths, A.J.V., Walther, T., 2010. Quantification of carbon contamination under electron beam irradiation in a scanning transmission electron microscope and its suppression by plasma cleaning. Journal of Physics: Conference Series 241, 3–7. doi:10.1088/1742-6596/241/1/012017.

[15] Hart, R.K., Kassner, T.F., Maurin, J.K., 1970. The contamination of surfaces during high-energy electron irradiation. Philosophical Magazine 21, 453–467. doi:10.1080/14786437008238431.

[16] Haynes, W. M., E., 2017. CRC Handbook of Chemistry and Physics. 97th ed., CRC Press/Taylor Francis, Boca Raton, FL. doi:10.1201/9781315380476.

[17] Heide, H.G., 1960. Die Objektverschmutzung und ihre Verhütung, Springer Berlin Heidelberg. pp. 87–90. doi:10.1007/978-3-642-50195-1_28.

[18] Hirsch, P., Kässens, M., Püttmann, M., Reimer, L., 1994. Contamination in a scanning electron microscope and the influence of specimen cooling. Scanning 16, 101–110. doi:10.1002/sca.4950160207.

[19] Hren, J.J., 1978. Specimen Contamination in Analytical Electron Microscopy: Sources and Solutions. Ultramicroscopy 3, 375–380. doi:10.1016/S0304-3991(78)80057-6.

[20] Hugenschmidt, M., Adrion, K., Marx, A., Müller, E., Gerthsen, D., 2023. Electron-Beam-Induced Carbon Contamination in STEM-in-SEM: Quantification and Mitigation. Microscopy and Microanalysis 29, 219–234. doi:10.1093/micmic/ozac003.

[21] Jiang, N., 2015. Electron beam damage in oxides: A review. Reports on Progress in Physics 79. doi:10.1088/0034-4885/79/1/016501.

[22] Kumao, A., Hashimoto, H., Shiraishi, K., 1981. Studies on specimen contamination by transmission electron microscopy. Journal of Electron Microscopy 30, 161–170. doi:10.1093/oxfordjournals.jmicro.a050301.

[23] Li, C., Pedrazo Tardajos, A., Wang, D., Choukroun, D., Van Daele, K., Breugelmans, T., Bals, S., 2021. A simple method to clean ligand contamination on TEM grids. Ultramicroscopy 221, 113195. doi:10.1016/j.ultramic.2020.113195.

[24] Lin, F., Liu, Y., Zhong, X., Chen, J., 2010. An improved image alignment procedure for high-resolution transmission electron microscopy. Micron 41, 367–372. doi:10.1016/j.micron.2010.01.001.

[25] Liu, C., Bonaccurso, E., Butt, H.J., 2008. Evaporation of sessile water/ethanol drops in a controlled environment. Physical Chemistry Chemical Physics 10, 7150–7157. doi:10.1039/b808258h.

[26] Malis, T., Cheng, S.C., Egerton, R.F., 1988. EELS log-ratio technique for specimen-thickness measurement in the TEM. Journal of Electron Microscopy Technique 8, 193–200. doi:10.1002/jemt.1060080206.

[27] Maurice, L., Duval, P., Gorinas, G., 1979. Oil Backstreaming in Turbomolecular and Oil Diffusion Pumps. Journal of Vacuum Science and Technology 16, 741–745. doi:10.1116/1.570073.

[28] McGilvery, C.M., Goode, A.E., Shaffer, M.S.P., McComb, D.W., 2012. Contamination of holey/lacey carbon films in STEM. Micron 43, 450–455. doi:10.1016/j.micron.2011.10.026.

[29] Mitchell, D.R.G., 2006. Determination of mean free path for energy loss and surface oxide film thickness using convergent beam electron diffraction and thickness

mapping: A case study using Si and P91 steel. Journal of Microscopy 224, 187–196. doi:10.1111/j.1365-2818.2006.01690.x.

[30] Mitchell, D.R.G., 2015. Contamination mitigation strategies for scanning transmission electron microscopy. Micron 73, 36–46. doi:10.1016/j.micron.2015.03.013.

[31] Ozawa, M., Higuchi, K., Nakamura, K., Hattori, M., Ohara, S., Arai, S., 2021. In situ observation of catalytic CeO2-nanocube (100) surface with carbon contamination by environmental TEM: A model for soot combustion. Japanese Journal of Applied Physics 60. doi:10.35848/1347-4065/abba0e.

[32] Power, B.D., Crawley, D.J., 1954. Sources, measurement and control of backstreaming. in oil vapour vacuum pumps. Vacuum 4, 415–437. doi:10.1016/0042-207X(54)90003-2.

[33] Pradhan, S., Hedberg, J., Blomberg, E., Wold, S., Odnevall Wallinder, I., 2016. Effect of sonication on particle dispersion, administered dose and metal release of non-functionalized, non-inert metal nanoparticles. Journal of Nanoparticle Research 18, 1–14. doi:10.1007/s11051-016-3597-5.

[34] Priyadarshi, A., Khavari, M., Subroto, T., Prentice, P., Pericleous, K., Eskin, D., Durodola, J., Tzanakis, I., 2021. Ultrasonics Sonochemistry Mechanisms of ultrasonic de-agglomeration of oxides through in-situ high-speed observations and acoustic measurements. Ultrasonics Sonochemistry 79, 105792. doi:10.1016/j.ultsonch.2021.105792.

[35] Raiber, K., Terfort, A., Benndorf, C., Krings, N., Strehblow, H.H., 2005. Removal of self-assembled monolayers of alkanethiolates on gold by plasma cleaning. Surface Science 595, 56–63. doi:10.1016/j.susc.2005.07.038.

[36] Reimer, L., Wächter, M., 1978. Contribution to the contamination problem in transmission electron microscopy. Ultramicroscopy 3, 169–174. doi:10.1016/S0304-3991(78)80023-0.

[37] Rodenburg, J.M., 2004. Understanding Transmission Electron Microscope Alignment : A Tutorial. Microscopy and Analysis 18, 9–11 (UK).

[38] Rykaczewski, K., Marshall, A., White, W.B., Fedorov, A.G., 2008. Dynamic growth of carbon nanopillars and microrings in electron beam induced dissociation of residual hydrocarbons. Ultramicroscopy 108, 989–992. doi:10.1016/j.ultramic.2008.04.006.

[39] Sayah, E., Brouri, D., Wu, Y., Musi, A., Da Costa, P., Massiani, P., 2011. A TEM and UV-visible study of silver reduction by ethanol in Ag-alumina catalysts. Applied Catalysis A: General 406, 94–101. doi:10.1016/j.apcata.2011.08.016.

[40] Sefiane, K., David, S., Shanahan, M.E.R., 2008. Wetting and evaporation of binary mixture drops. Journal of Physical Chemistry B 112, 11317–11323. doi:10.1021/jp8030418.

[41] Tokunaga, T., Saito, K., Kuno, K., Higuchi, K., Yamamoto, Y., Yamamoto, T., 2019. Removal of carbon contamination in ETEM by introducing Ar during electron beam irradiation. Journal of Microscopy 273, 46–52. doi:10.1111/jmi.12759.

[42] Woehl, T.J., Jungjohann, K.L., Evans, J.E., Arslan, I., Ristenpart, W.D., Browning, N.D., 2013. Experimental procedures to mitigate electron beam induced artifacts during in situ fluid imaging of nanomaterials. Ultramicroscopy 127, 53–63. doi:10.1016/j.ultramic.2012.07.018.

[43] Ye, F., Xu, M., Dai, S., Tieu, P., Ren, X., Pan, X., 2020. In Situ TEM Studies of Catalysts Using Windowed Gas Cells. Catalysts 10, 779. doi:10.3390/catal10070779.

[44] Yuan, Y., Amine, K., Lu, J., Shahbazian-Yassar, R., 2017. Understanding materials challenges for rechargeable ion batteries with in situ transmission electron microscopy. Nature Communications 8, 1–14. doi:10.1038/ncomms15806.

4 Sample-specific preparation techniques for improved transmission electron microscopy measurements

4.1 Abstract

Transmission electron microscopy (TEM) is an important analytical technique for investigating samples with resolutions down to the atomic scale. One obstacle is the formation of hydrocarbon contamination on the sample surfaces, which needs to be removed or mitigated. For this purpose several different methods are commonly applied that, among others, include plasma cleaning, ozone cleaning, heating or cooling of the sample and beam showering. A downside of established cleaning methods is that they are often harsh on the sample, time consuming or not agreeable with all of the sample's characteristics. In this work, we applied the approach of vacuum removal of volatile contaminants to improve the cleanliness of the TEM specimens. For vacuum removal of hydrocarbons, a dedicated sample cleaning setup was built in which we can monitor the outgassing of contaminants based on the pressure, which allows us to establish sample-specific cleaning procedures. The cleanliness of these samples was quantified by thickness measurements with electron energy loss spectroscopy (EELS) in the microscope that determine the thickness of the contamination layer. We have prepared samples in our setup with toluene and THF, two solvents used in chemical synthesis. The contamination buildup after cleaning with our sample cleaning station (SCS) was compared with contamination accumulated on samples cleaned by other established methods. In our experiments, we also investigate the impact these cleaning treatments have on the carbon film of commercially available TEM

grids and on the accumulated contamination resulting from the sample preparation. We introduce here the approach of vacuum contamination removal as a gentle alternative to already established sample cleaning procedures.

4.2 Introduction

TEM offers the opportunity to investigate a large variety of specimens by obtaining imaging and spectroscopic data down to the atomic scale in many important research fields. One obstacle faced during TEM experiments is that the beam can cause hydrocarbon contamination by reducing volatile organic components (VOCs) to amorphous carbon on the specimen surface. The thus formed contamination increases the sample thickness and impedes high-quality investigations of samples. In the early days of electron microscopy, VOCs mostly stemmed from oil diffusion pumping systems, where the backflow of oil molecules lead to poor vacuum conditions in the microscope[4,5,14]. Though vacuum technology has improved since then, carbon contamination has remained to be a major problem. Contaminants may originate from the used equipment like tweezers, grids or the sample holder[7,22], but also from the sample itself. Many samples inherently contain carbon that can affect TEM experiments, e.g., as ligands or stabilizing agents for nanoparticles[12,20,33]. Carbon, naturally is also part of organic solvents, which are either utilized in synthesis, for dispersing the sample or de-agglomerizing sample particles[26,27].

There are several established approaches for mitigating or removing carbon contamination, though all of these have their respective advantages and disadvantages. These methods include plasma cleaning[8,15], ozone cleaning[10,31,32], heating[2,22] or cooling[3,18,19] of the sample, beam showering[2] or washing the specimen[20]. While each technique by itself has been proven to be efficient for the reduction of hydrocarbon contamination, a suitable method needs to be tailored to a sample's characteristics, as some approaches may impact the sample negatively. Plasma and ozone cleaning both are abrasive and only suitable for samples that are not altered under these processes' harsh conditions. Cooling the sample

can prevent contaminant diffusion towards the electron beam, yet it requires a designated sample holder and constant cooling is required, while at the same time thermal drift of the sample presents a challenge. The sample can either be heated in the microscope, again by using a special sample holder, or outside of the microscope, e.g., by a halogen lamp. Heating the sample always comes with the risk of altering its properties, e.g., by oxidation, phase transitions or reactions with other contaminants. In addition, heating within the microscope can lead to outgassing of contaminants in its octagon. Beam showering can be time consuming, is limited to a certain area of the TEM grid and needs to be repeated if features in other areas are to be investigated. Washing the specimen introduces a solvent as an additional source of contamination and has only found limited application so far. Some of these methods prevent contaminants from being transferred to the inner parts of the microscope, which is of advantage as maintaining the microscope in a clean condition is crucial for high-quality experiments. Strategies for the mitigation of contamination adsorbing to surfaces in ultra high vacuum (UHV) setups and improving the pressure have been established[9,23], though the associated cleaning protocols often require the disassembly of the setups, and are therefore not suitable for electron microscopy. Contamination removal studies for other UHV applications conclude that heating and extended pumping times seem to have a significant impact on partial pressure of hydrocarbons in UHV systems[9].

In this work we describe the approach of removing contaminants resulting from the sample preparation by establishing a vacuum. By extending the knowledge obtained from contaminant removal in other UHV applications, a self-built SCS enables a novel approach of vacuum removal of hydrocarbons as a mitigation strategy in TEM sample preparation.

4.3 Methods

4.3.1 TEM sample preparation

For all experiments, commercially available holey carbon grids (Cu, 400 mesh, Plano-EM) were used. For contamination measurements, 1 µL of sample was deposited on the grid before proceeding as described in section 4.3.3. The solvents THF and toluene used for the experiments were dried by a molecular sieve and distilled before the experiments. Nanoparticle samples, of which some were stabilized by supported ionic liquid phase [1], consisted of either CoP or MoP [30].

4.3.2 EELS thickness measurements

All samples were investigated in a Thermo Scientific Talos F200X transmission electron microscope with a Gatan Continuum S spectrometer. For determining the thickness of carbon contamination accumulated in our TEM studies, EELS experiments were conducted. EELS allows to quantify the sample thickness by comparing the quantity of electrons that experience elastic scattering processes when passing through the sample with that that do not. The local thickness of the samples is determined by the log-ratio-method [21] described by eq. (4.1), with d being the thickness, λ the inelastic mean free path and I_t and I_0 being the amount of electrons contributing to the total and the zero loss EEL spectra, respectively.

$$\frac{d}{\lambda} = \ln \frac{I_t}{I_0} \tag{4.1}$$

The inelastic mean free path is determined based on approximations determined with the GMS DigitalMicrograph plugin "Mean Free Path Estimator" by Dave Mitchell [24]. Our energy-dispersive X-ray (EDX) spectroscopy measurements indicate that the accumulated contamination consisted of at least 95% carbon with traces of nitrogen and oxygen. When calculating the inelastic mean free path, it was assumed that the contamination only

consists of carbon, as the traces of nitrogen and oxygen changed the value for λ less than 1%.

To determine the dependence of the accumulation of contamination on the beam exposure time, an area of 512×512 pixel^2 (approx. 173×173 nm^2) was exposed in scanning TEM (STEM) mode for different durations between 5 s and 480 s with a dwell time of 2 µs per pixel and a magnification of 583 kx.

4.3.3 Contaminant removal using techniques discussed in the literature

Established cleaning procedures suggested in the literature are compared in their efficiency regarding carbon removal and abrasiveness on the carbon film of the grid. For plasma cleaning, the samples were exposed to a synthetic air plasma (80% N_2 / 20% O_2) at a power of 40 W two times for 15 s each with a Gala Instumente PlasmaPrep5 plasma cleaner. Ozone cleaning was performed with a Hitachi ZONE-TEM Desktop Sample Cleaner with the setting recommended by the manufacturer. Each side of the grid was cleaned for 5 min at a pressure of 330 mbar. For cleaning by beam showering, the samples were showered immediately after inserting them into the TEM for 20 min by a wide-spread electron beam in TEM mode before measuring contamination buildup. Cleaning by heating was carried out by illuminating the freshly prepared TEM grid with a halogen lamp for 10 min. The temperature at the sample was 90 °C.

4.3.4 SCS working principle

For a customized pretreatment of the samples, we have designed and built an UHV cleaning setup (SCS) In fig. 4.1(a), the general working principle and the main components of the SCS are shown. At the top, the sample chamber is located, in which TEM grids and a TEM sample holder can be deployed. It can be additionally heated by a halogen

lamp. Below the sample chamber, a baffle cooler serves as a liquid nitrogen cooled cold trap for adsorbing contaminants from the vacuum. This setup is pumped with a turbo pump located at its bottom. Between the sample chamber and the cooler and between the cooler and the turbo pump, two pressure gauges (A and B) are inserted. The components between sample chamber and baffle cooler can also be heated with external heating wraps, which prevent condensation on the inner surfaces. A schematic representation of the assumed cleanliness of the SCS before (left) and after (right) pumping a specimen in the sample chamber is shown in fig. 4.1(b). In addition to cleaning the specimens by vacuum, different temperature zones can be established (fig. 4.1(c)) by heating the sample chamber with a halogen lamp to up to 120 °C.

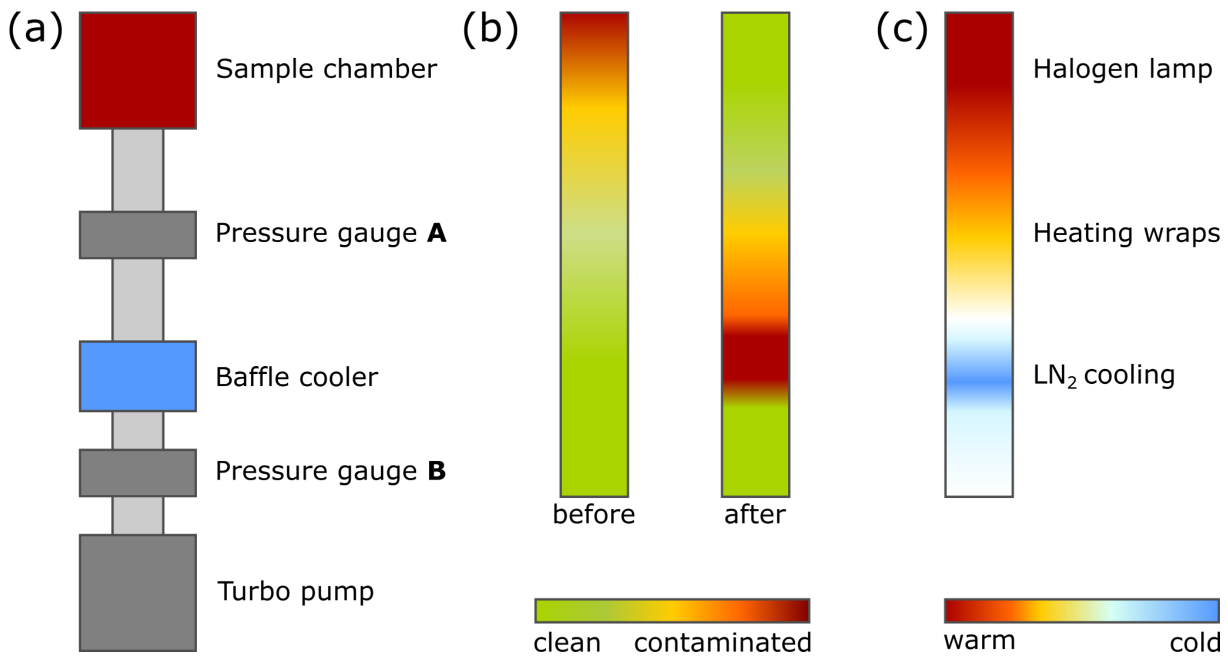

Figure 4.1: (a) Working principle of our SCS with its components. (b) The temperature zones result in a contamination gradient, which is different before and after the cleaning procedure.(c) Using heating and cooling devices, different temperature zones can be established.

When pumping the SCS, the pressure in the upper part of the setup at pressure gauge A is modified by outgassing contaminants, which desorb from samples in the setup chamber. These contaminants move in the setup and get adsorbed to the baffle cooler due to its

low temperature. The pressure below the cooler is lower than in the upper part of the setup. On the one hand, the upper part contains higher amounts of contaminants while, on the other hand, the lower part of the setup is not obstructed by the cooler, allowing a more efficient removal of gas molecules.

CAD drawings of the whole assembly and a close up of the sample chamber of the SCS are shown in fig. 4.2 and fig. 4.3, respectively. For safe operation of the setup, individual pumping of the different areas of the setup to prevent condensation of gases on the liquid nitrogen cooler is ensured and measures to prevent positive pressure are taken.

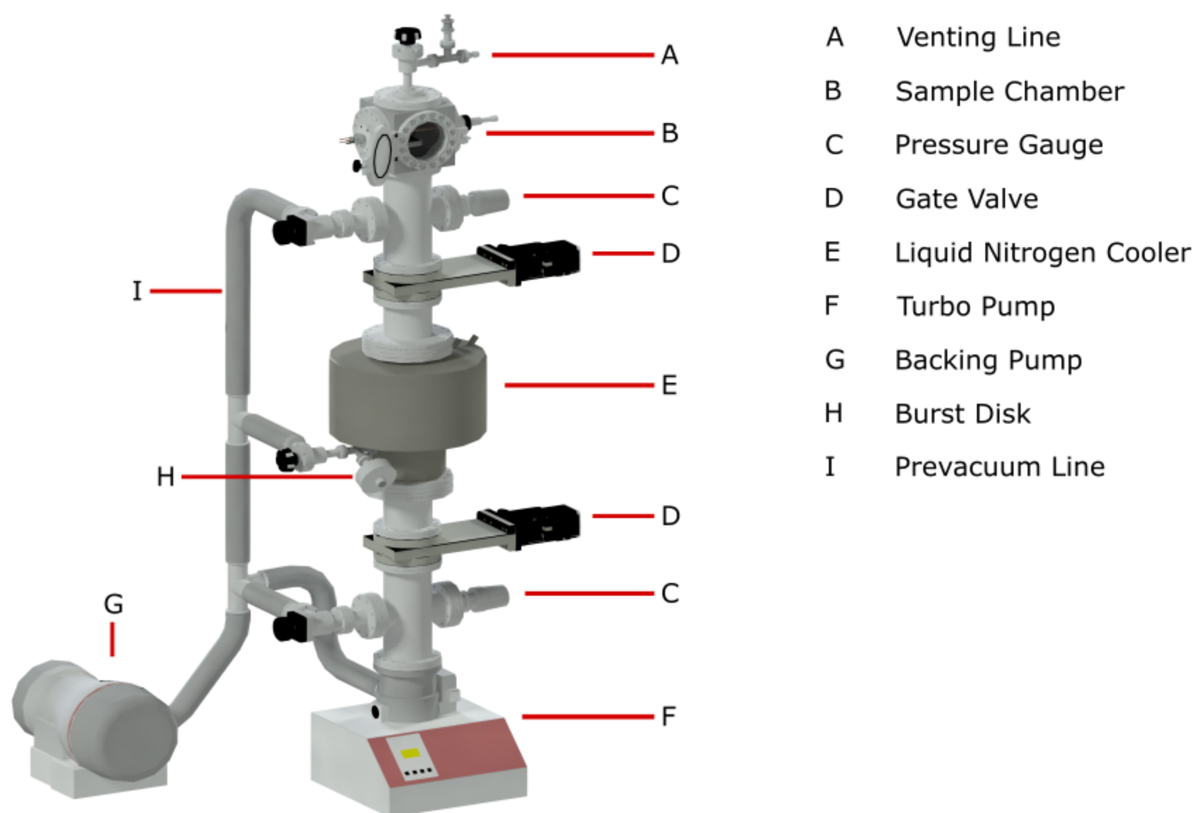

Figure 4.2: CAD drawing of the assembly of our SCS Setup with its most important components.

The close-up of the sample chamber shows the arrangement of different components. Samples can be either mounted in a sample holder or stored in the grid holder block. When heating with the halogen lamp, the temperature is distributed evenly in the sample

chamber due to the polished stainless steel surfaces and monitored by a thermocouple.

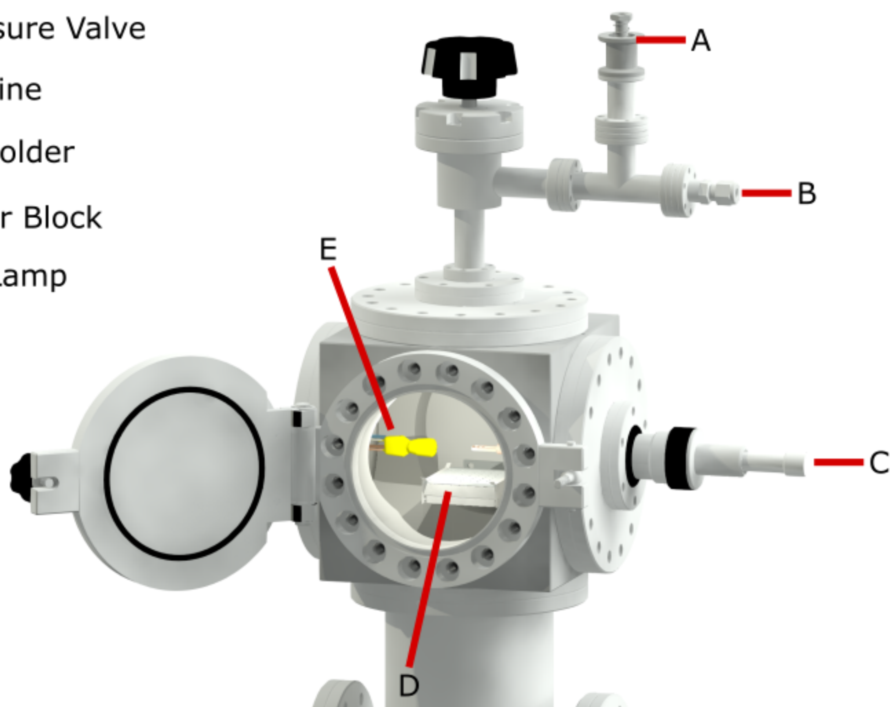

Figure 4.3: Close-up of the sample chamber of the SCS.

4.3.5 Data evaluation of the pressure measurements

For obtaining reproducible data and ensure that different data sets can be meaningfully compared which each other, we established a standardized operation procedure for our setup. It is applied for all measurements and includes a starting protocol. When starting the SCS, the same order of starting the pumps and changing valve positions is maintained for all measurements, resulting in the setup being exclusively pumped by the turbomolecular pump after 360 s.

When pumping a vacuum setup, residual molecules are removed in a certain order [6]. The initial gas volume is pumped first, which happens on a short timescale and only takes a few seconds. In the next step, adsorbed species are removed. While some species, e.g., air components, desorb fast, some hydrocarbons or water molecules take significantly

longer. After a few hours, the pressure decreases very slowly and is determined by diffusion processes. In our SCS, this point is reached 8 to 10 h after starting the pumping procedure. The lowest pressure that can be reached in a setup is determined by permeation and leakage processes.

For establishing sample-specific cleaning protocols, the pressure differences between reference measurements of empty TEM grids and sample measurements are investigated under the assumption that only desorption processes contribute to the cleanliness of samples in the SCS, while the final pressure barely affects the sample cleanliness, as contaminant desorption processes have finished at this point.

As contaminants need to desorb from the sample first before they adsorb to the baffle cooler, the pressure at gauge A decreases slower when outgassing increases the pressure. At the same time, it is assumed that the vacuum in the lower part of the setup is clean both during reference and sample measurements and that here the pressure decreases in a similar way for all measurements.

4.4 Results and discussion

4.4.1 Cleaning of TEM samples in the SCS

For evaluating necessary drying times of samples in our SCS, both THF and toluene samples were investigated. Therefore, six grids were prepared with 1 µL solvent each and distributed evenly across the sample holder block to achieve a detectable pressure difference despite the small sample volume. The duration a sample needs to remain in the SCS until it is clean can be determined by comparing the pressure of a sample measurement with that of a reference measurement. As a reference, the same number of empty TEM grids was measured under the assumption that here no relevant outgassing should impact the pressure in the SCS. As long as a pressure difference between the sample and reference measurements is detected in the upper part of the setup, where

outgassing processes impair the vacuum quality, it can be assumed that the sample is not clean enough for TEM experiments. The sample chamber was not heated during these experiments, while the connecting flanges between sample chamber and baffle cooler were kept at a constant 40 °C to prevent adsorption of contaminants.

The pressure gradient measured above the cooler is shown in fig. 4.4. When the setup is pumped, a difference in the pressure decrease between the solvents and the reference can be observed. After 30 min (THF, red) and 90 min (toluene, blue), respectively, the pressure of these samples is very similar to that determined for the reference (black). This indicates that no VOCs are outgassing from the sample anymore at these points in time and as a result the specimens are clean enough for TEM analysis. The vapor pressure and boiling point for THF and toluene at 25 °C and 101.325 kPa are given in table 4.1[11]. These values are consistent with the sample prepared with THF having a shorter drying time than the toluene sample.

Solvent	Vapor pressure / kPa	Boiling point / °C
THF	21.6	66
Toluene	3.79	110.6

Table 4.1: Vapor pressure and boiling point of THF and toluene at 20 °C and 101.325 kPa[11].

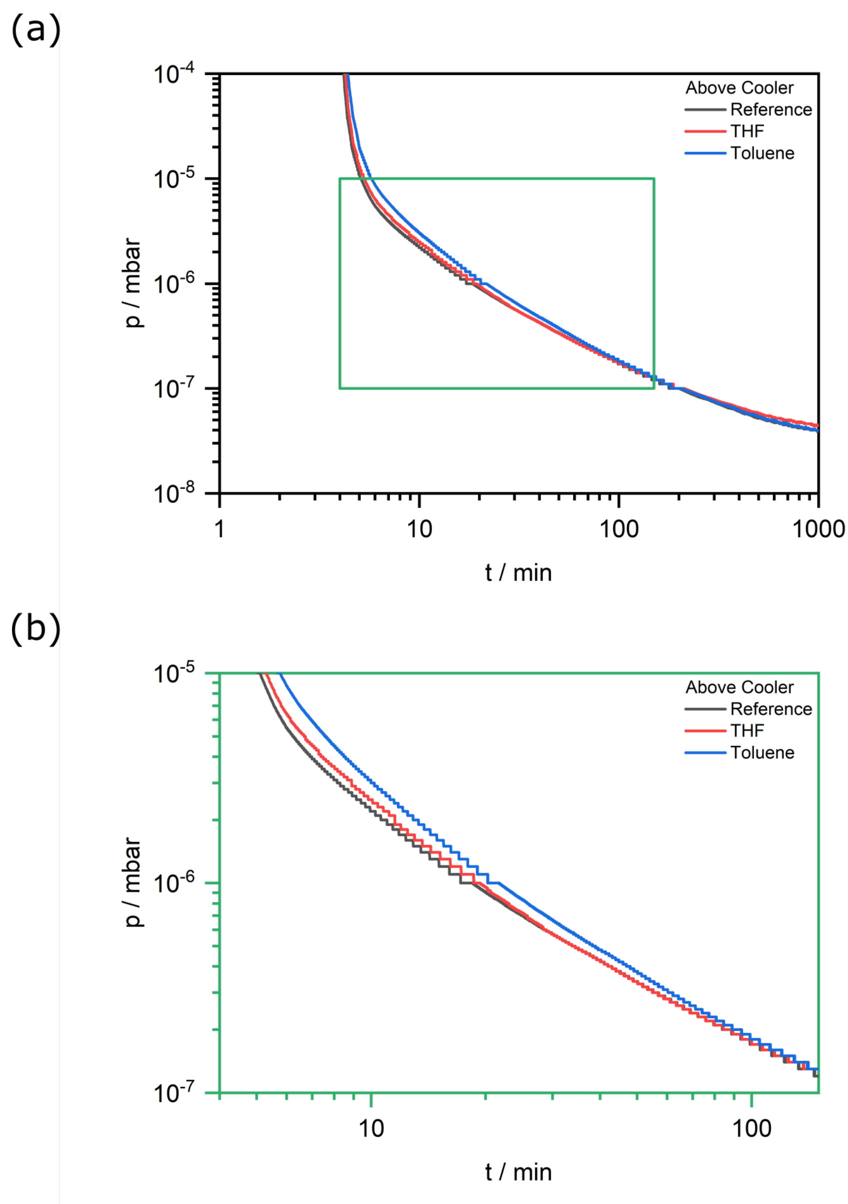

Figure 4.4: (a) Pressure of THF (red), toluene (blue) and the reference (black) measured above the cooler, with the data in the green box shown enlarged in (b).

When comparing the pressure measured below the cooler (fig. 4.5), the data obtained for both solvents and the reference are very similar. This suggests that only a small amount of contaminants is present below the cooler. After roughly 4 h, the pressure starts to fluctuate and increases for short times due to contaminants desorbing from the cooler,

which has become warmer in the mean time.

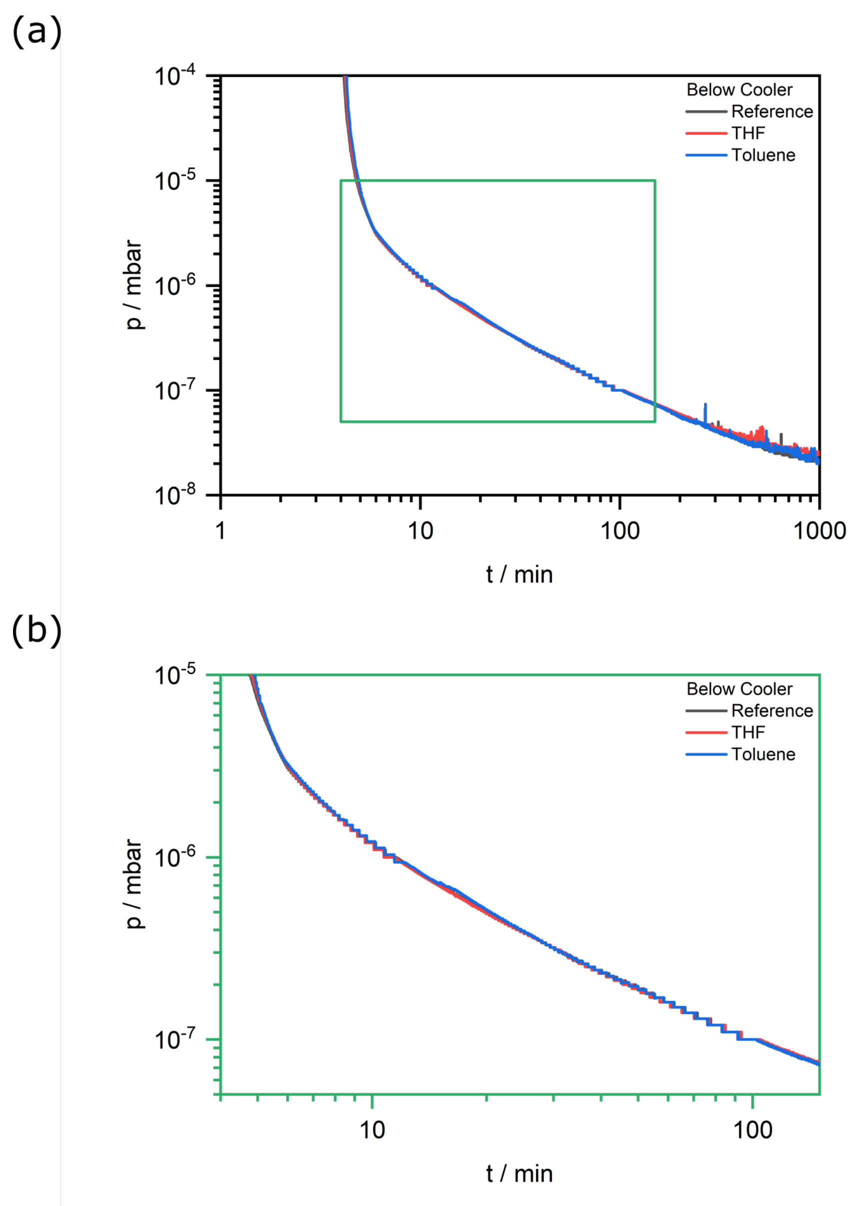

Figure 4.5: (a) Pressure of THF (red), toluene (blue) and the reference (black) measured below the cooler, with the data in the green box are shown enlarged in (b).

4.4.2 Assessment of the SCS parameters

When building a vacuum setup such as our SCS, the question may arise how important its physical dimensions are and if a down-scaled version with smaller component sizes would work just as well. We choose flange diameters along the main axis of the setup of at least 100 mm, and the overall height is approximately 1.8 m. Some thoughts on factors contributing to the functionality of the setup are discussed in this section.

When venting the setup with nitrogen, molecules adsorb to the inner surfaces of the SCS. The purity of the venting gas may impact adsorption to the setup surfaces and therefore impair the vacuum decrease when pumping the setup, though this should not be of relevance for the sample cleanliness. When assembling the sample holder block or inserting a TEM sample holder, a gas counter flow was utilized to mitigate backstreaming of air into the sample chamber. Due to the large size of our setup, the surface area is quite high. A smaller surface area would be advantageous when pumping the setup, as fewer molecules needed to be removed for improving the vacuum. Overall, the pressure would drop faster in a smaller setup, if other setup components (e.g., the pump) remained the same. In our setup, the surfaces are kept at a stable temperature to reduce surface adsorption in the contaminant-rich area of the setup.

At ambient pressure, the mean free path, $\bar{l}$, of molecules in the gas atmosphere is very small, as the high density of molecules results in multiple collisions. The mean free path is given by eq. (4.2), with k being the Boltzmann constant, T the temperature, d_m the diameter of a molecule and p the pressure[16].

$$\bar{l} = \frac{k \cdot T}{\sqrt{2} \cdot \pi \cdot d_m^2 \cdot p} \tag{4.2}$$

Considering a N_2 molecule with diameter of $374 \cdot 10^{-12}$ m[17], at 10^{-7} mbar, the mean free path $\bar{l}$ is approximately 662 m at a temperature of 25 °C.

The flow regime at which molecules are removed in the vacuum is quantified by the

Knudsen number K_n, given by eq. (4.3)

$$K_n = \frac{\bar{l}}{d_s} \tag{4.3}$$

where d_s is the setup diameter and $\bar{l}$ the mean free path of the gas molecules. For $K_n < 0.01$, the molecules are removed in a viscous flow in which molecule-molecule interactions are predominant. For $K_n > 0.5$, the molecules are in a state of free molecular flow and collide with the static setup surfaces while the probability of interactions with other gas molecules can be neglected. This applies for the aforementioned N_2 molecule, for which $K_n \approx 6620$. Under these free molecular flow conditions, the volumetric flow rate, q_{pV}, is described by eq. (4.4) and depends on the orifice area A between the sample chamber and the pump, the mean thermal velocity $\bar{c}$ of the molecules and the pressure difference Δp[16].

$$q_{pV} = A \cdot \frac{\bar{c}}{4} \cdot \Delta p \tag{4.4}$$

Here, an increased orifice cross-section (and therefore larger setup dimensions) are of advantage as a higher gas quantity can be removed under the setup's working conditions. This also applies to the process of contaminant removal in TEM specimen under vacuum, which also profits from larger setup dimensions. Therefore we assume that a setup with larger dimensions is preferable for cleaning TEM specimens.

In vacuum applications, other parameters like diffusion through vacuum seals, permeation through vacuum components and leakage all have an influence on the vacuum. For our SCS, the contribution of these factors is assumed to be small enough to have no relevant impact on the vacuum when pumping the setup for cleaning TEM specimens.

Overall, when considering the setup dimensions, larger sample chamber volumes and flange diameters are advantageous, as they promote the removal of VOCs. A larger sample chamber provides a larger surface on which contaminants can adsorb, though this can be prevented by heating the setup. On the other hand, smaller setup dimensions can

hinder the contaminant removal, and are therefore not recommended.

4.4.3 Contamination of TEM grids

In this section, the performance of our SCS for addressing contamination accumulated in the TEM is investigated and compared to other established cleaning methods. The TEM grids used in these studies were prepared and cleaned as stated in section 4.3.3 before being exposed to the electron beam for different durations. Accumulated contamination was quantified by EELS. For the evaluation, the thickness of the carbon film itself was subtracted from all contamination measurements as the background. The quality of different contamination removal techniques can be assessed either by comparing the volume of the accumulated carbon contamination or by the thickness within the scanned area. Due to the scanning procedure in STEM mode, the electron beam remains longer at the border of the scanned area, so the accumulated contamination is not distributed homogeneously across the illuminated area. Moreover, the abrasiveness of different cleaning methods can be assessed based on the thickness of the carbon film in areas that are not contaminated.

In fig. 4.6, examples of EELS thickness maps of an investigated area are shown for a sample of toluene dried for 90 min at ambient pressure and exposed for 10 s to the electron beam. At the top left, the area scanned for accumulating contamination is marked by the white square. The areas considered for evaluating the contamination are outlined by the white dashed rectangles: At the top right, an area evaluated for determining the average carbon film thickness is shown. The background is subtracted when evaluating the contamination volume and thickness within the exposed area. At the bottom left, the area considered for the contamination volume and at the bottom right the area used for measuring the average thickness in the inner of the exposed area are marked.

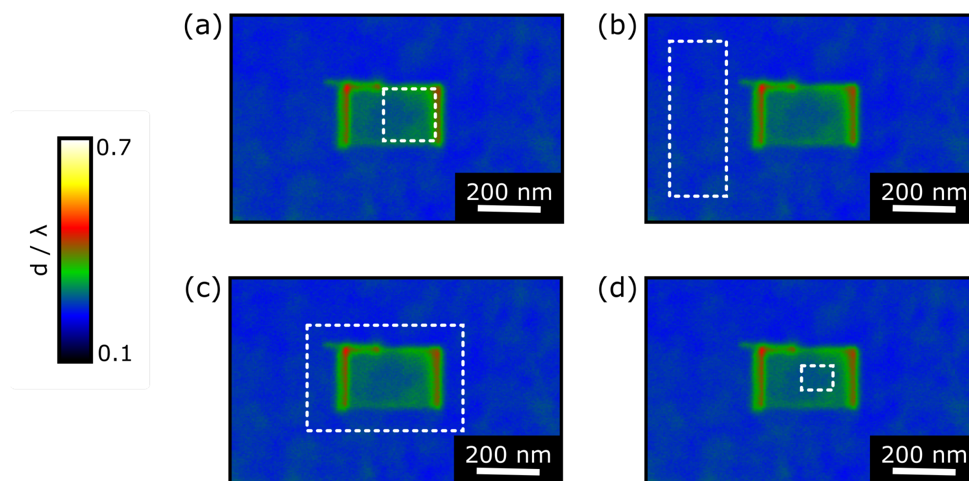

Figure 4.6: EELS thickness map of different areas considered in the evaluation of a sample of toluene, that was dried for 90 min at ambient pressure and exposed for 10 s to the electron beam. The white rectangles outline the following areas that were evaluated: (a) Scanned area, (b) carbon film thickness (background), (c) contamination volume, (d) thickness in the inner of the exposed area.

In fig. 4.7, the contamination of different grids was investigated and compared to grids prepared with solvent and dried in the SCS. The analyzed grids were either used as delivered by the manufacturer without any pretreatment (empty grid), or stored in the SCS over night at room temperature (empty grid SCS). For comparison, empty grids were also treated with ozone cleaning and plasma cleaning. In addition, grids were also prepared by applying 1 µL of either THF or toluene and drying them for 30 min or 90 min in the SCS, respectively.

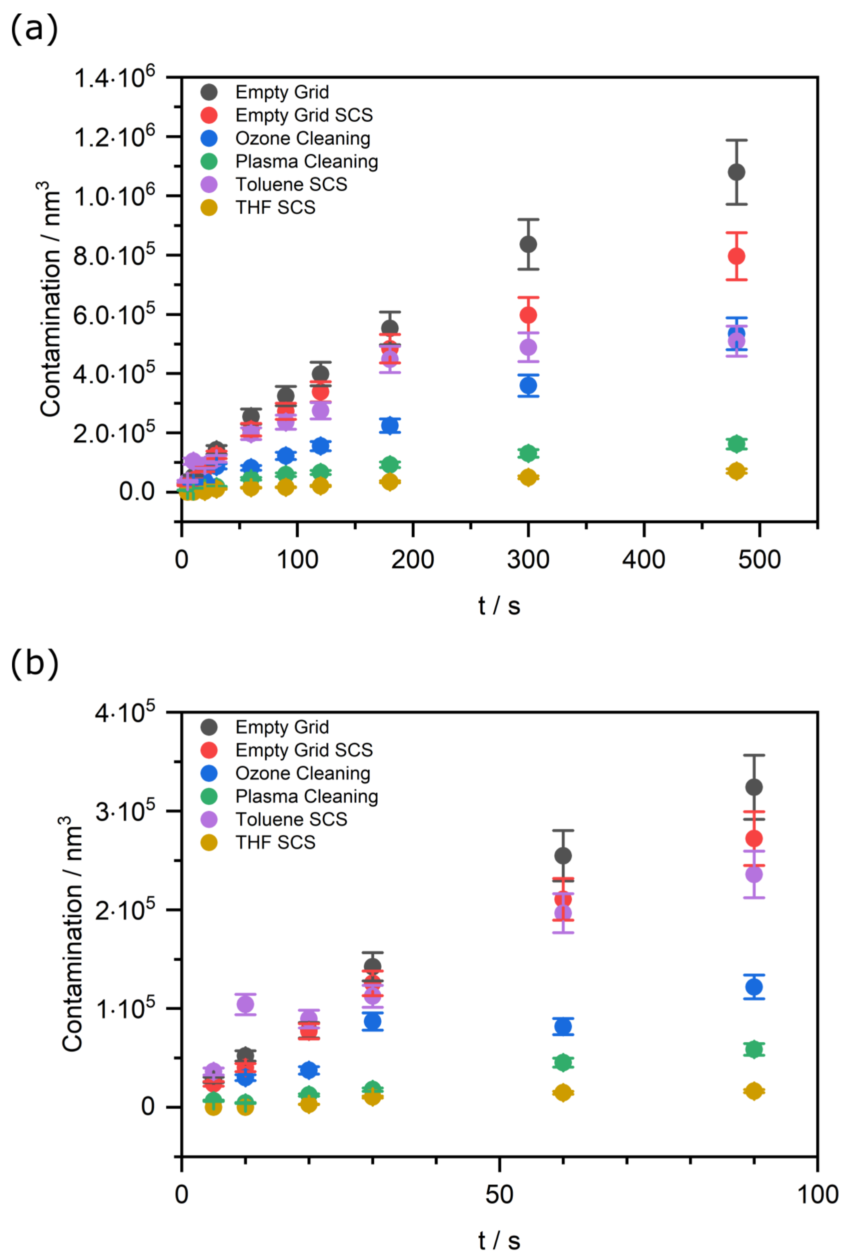

Figure 4.7: Contamination accumulated on empty grids without any treatment, after SCS cleaning, plasma and ozone cleaning and after solvent (toluene and THF) exposure and cleaning by SCS. Measurements up to 480 s beam exposure time are shown in (a), while in (b), the first 100 s are shown enlarged.

The highest degree of contamination was accumulated on the grid that was not treated

at all by any cleaning method and was measured right out of the box it was delivered in. Less contamination was accumulated when the empty grid was cleaned by the SCS. While in the case of plasma cleaning only little contamination was accumulated, a much higher degree of contamination was observed after ozone cleaning. During ozone cleaning, hydrocarbon contamination was broken down to molecular fragments, but not sufficiently removed and instead still adsorbed to the carbon film of the grid, which subsequently lead to contamination induced by the electron beam. Longer pumping durations or a higher vacuum might be beneficial for this cleaning method. The grids prepared with the solvents toluene and THF also showed a lower degree of contamination than even the empty grid cleaned in the SCS. It can be assumed that residues from the grid manufacturing process were dissolved by the solvent and removed by the vacuum in the cleaning station. The grid prepared with THF was contaminated the least, as here again volatile residues on the grid were dissolved or washed away by THF, which itself has a quite high vapor pressure than toluene and therefore can be removed quite well.

While fig. 4.7 shows the total contamination volume depending on the electron beam exposure time, fig. 4.8 shows the thickness in the inner part of the scanned area. For the grids prepared in our SCS, the thickness in the inner parts of their exposed area was very similar to that of the actual carbon film itself, indicating that these areas were barely contaminated. However, if the total accumulated carbon volume was determined instead of the thickness, an increase could still be observed. Due to the microscope's scanning procedure, volatile contaminants diffuse towards the positions where the electron beam dwells longer, namely to the outer parts of the scanned area. Therefore, it is assumed that the empty grids have high amounts of adsorbed species attached to them, which either originate in the manufacturing process or the sample storage. This also confirms the assumption that after ozone cleaning, contaminant fragments remain adsorbed to the grid. When TEM specimens are prepared with the SCS, the inner area is still suitable for analysis that requires low contamination. It can be assumed that residual hydrocarbon molecules are dissolved and washed away by the solvents. For plasma cleaning,

the thickness in the inner part of the exposed areas was small, like the total degree of contamination, so overall the cleaning with this method was very successful.

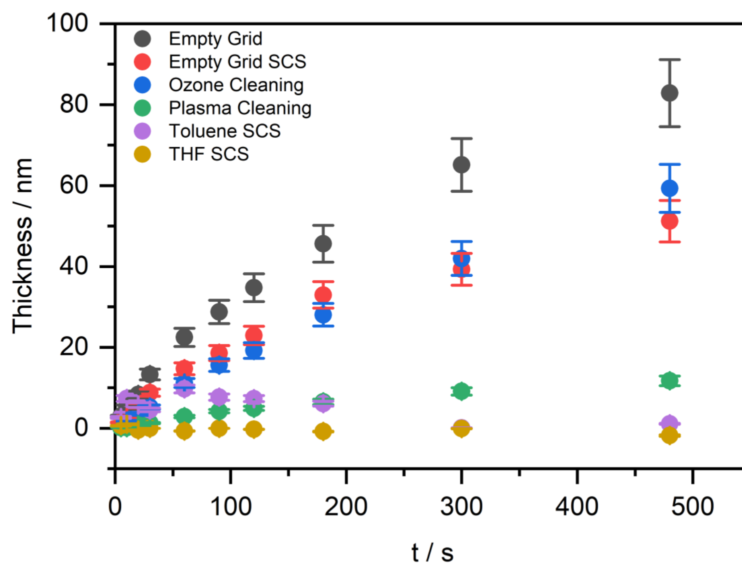

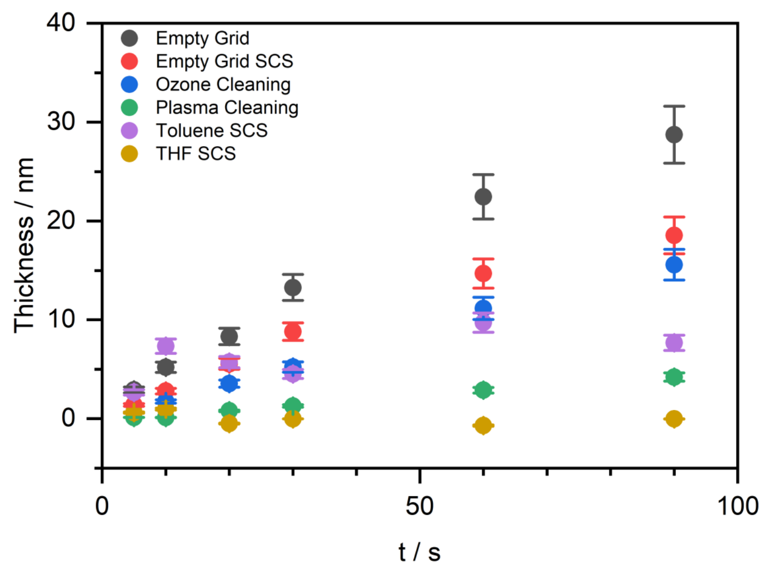

Figure 4.8: Thickness of contamination in the inner part of the exposed area of TEM grids after cleaning by different methods. The whole measured time scale is covered in (a), while the first 100 s of the data are shown enlarged in (b).

In addition to contamination that was accumulated by extended electron beam exposure, the impact of the different cleaning procedures on the carbon film thickness of the grid was investigated, as illustrated by fig. 4.9. That the carbon film has a certain thickness is crucial for supporting the samples and for withstanding selected cleaning procedures. The carbon film on an untreated, empty grid was of similar thickness as that on a grid prepared in the SCS. This also true for the carbon film on grids prepared with THF and toluene and dried in the SCS. In contrast, the abrasive properties of both ozone treatment and plasma cleaning resulted in a significantly thinner carbon film that has lost approximately one third of its thickness.

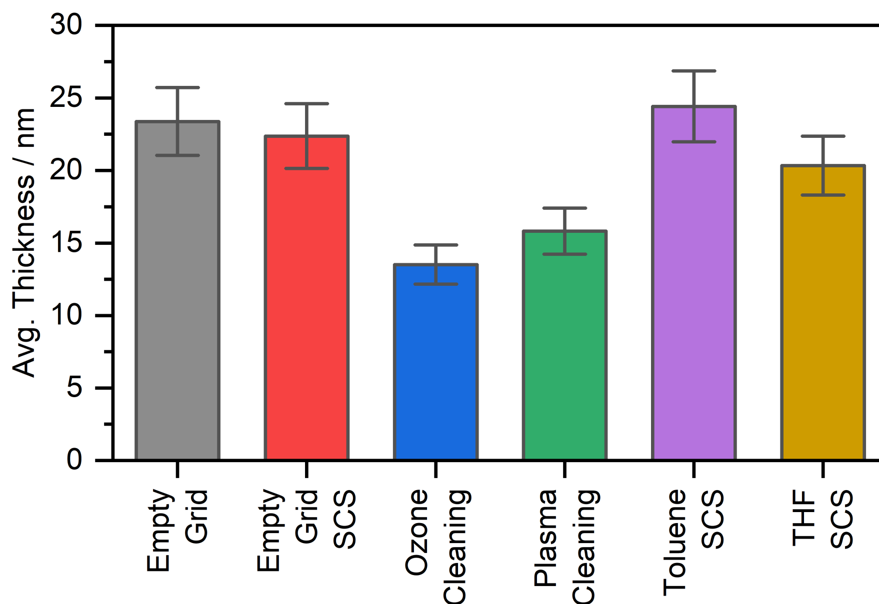

Figure 4.9: Carbon film thickness of grids after applying different cleaning treatments for hydrocarbon removal.

We can conclude that despite thinning the carbon film, plasma cleaning seems suitable for removing contamination, enabling our follow-up experiments, because only little contamination was accumulated after such treatment. In comparison, ozone cleaning thinned

the carbon film even more than plasma cleaning. It is assumed that the hydrocarbons broken down by ozone are still adsorbed to the sample surface, as during ozone cleaning roughly three times more contamination was accumulated than during plasma cleaning. Therefore, ozone cleaning was discarded in further experiments.

4.4.4 Comparison of cleaning methods on the example of toluene

When preparing a specimen by dispersing the sample in organic solvent, removing organic residues as well as possible is crucial for the experiments. While often specimens are dried at ambient pressure, the grids can also be treated by established methods, e.g., heating, plasma cleaning or beam showering, which we compare with cleaning by our SCS in fig. 4.10. Also, the impact of outgassing of a sample in the TEM vacuum is contrasted to cleaning in the SCS vacuum.

By far the highest degree of contamination was accumulated when the sample was dried at ambient pressure for 90 min, making this the least favorable method. Due to toluene's low vapor pressure, a high amount of contaminants remained on the sample surface despite the long drying time. Cleaning a sample for 90 min in the SCS resulted in roughly the same contamination as for a sample that remained 90 min in the TEM, and overall both showed significantly less contamination than the sample dried at ambient pressure. The SCS has the advantage that the outgassing VOCs do not contaminate the pole piece of the TEM, whose removal is a tedious process and often causes significant downtimes of the microscope. Based on the accumulated contamination, beam showering the sample was the most efficient technique, yet here also the sample outgasses in the microscope, as only a small area of the grid is cleaned by this method. Again, like in the previous experiments with empty grids described in section 4.4.3, plasma cleaning emerges as a powerful method for contamination mitigation. However, due to its abrasive properties, it is only suitable for certain TEM specimens. Heating the sample is also an efficient method for contamination removal, though the elevated temperature (90 °C) may alter

the sample's properties, e.g., by oxidation.

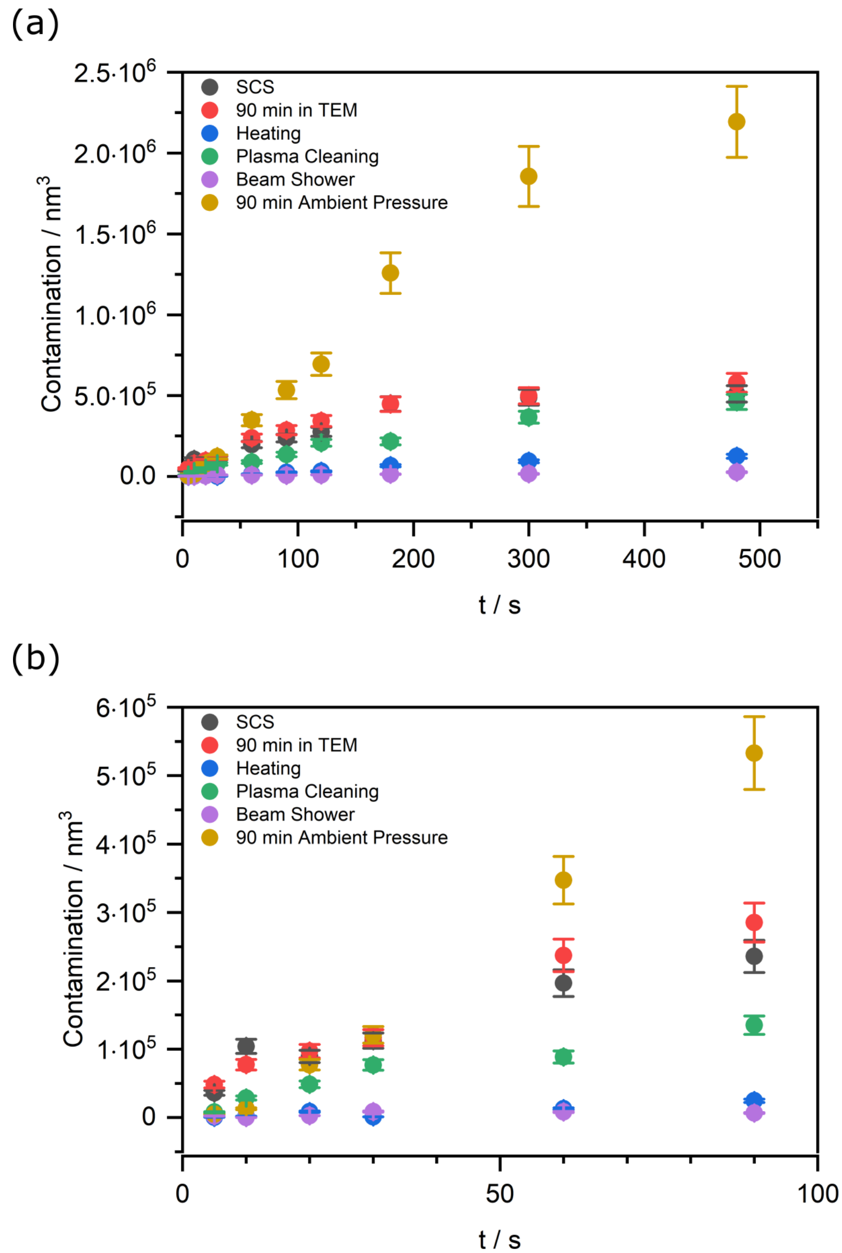

Figure 4.10: Accumulated contamination of grids prepared with toluene and pre-treated by different established methods. Measurements covering the whole range of exposure times are shown in (a), while data with exposure times up to 100 s are shown enlarged in (b).

Contamination growth is linked to diffusion of the VOCs towards the electron beam [13,28,29].

The total contamination volume undergoes a parabolic rate increase, as suggested by Mitchell[25]. The fitted data is included in the supporting information.

In fig. 4.11, the thickness in the inner part of the area exposed to the electron beam is shown. For the sample dried at ambient pressure, a high thickness was observed. The thickness increases for exposure times up to 180 s, and then decreases for exposure times of 300 s and 480 s. The extended exposure times seem to induce more surface diffusion towards the positions where the electron beam remains longer. For the sample prepared in the SCS, the same trend was observed, though the grid was hardly contaminated in the inner part at all. The sample measured after remaining 90 min in the TEM vacuum also showed this behavior, though not in a very pronounced way. For the sample treated with the plasma cleaner, this effect did not occur. Instead, a steady increase of the thickness was measured with longer exposure times. It is assumed that the different behavior reflects to different contaminants. Solvent molecules are broken down by plasma cleaning and therefore it is likely that the contaminants differ from the solvent molecules. Due to their lower masses, these contaminant fragments are probably more mobile when partaking in diffusion processes. For the samples cleaned by heating and by beam showering, a small increase of the thickness was observed, though these samples were overall not too much affected by contamination growth.

(a)

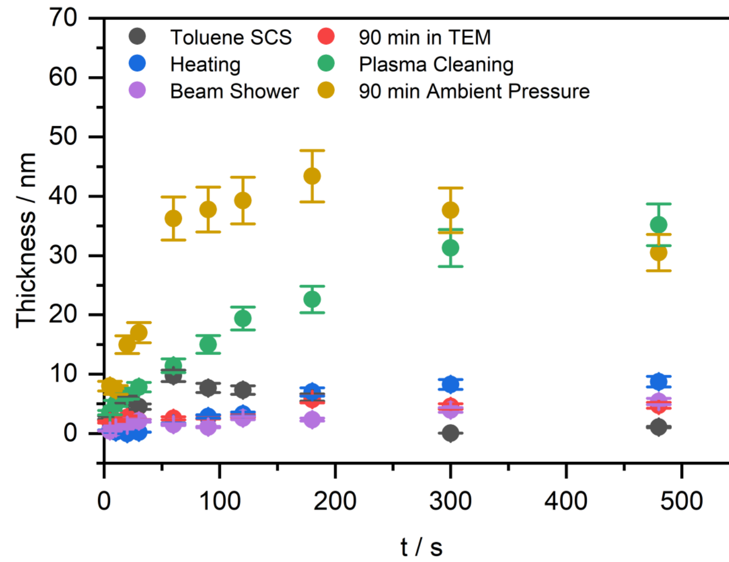

(b)

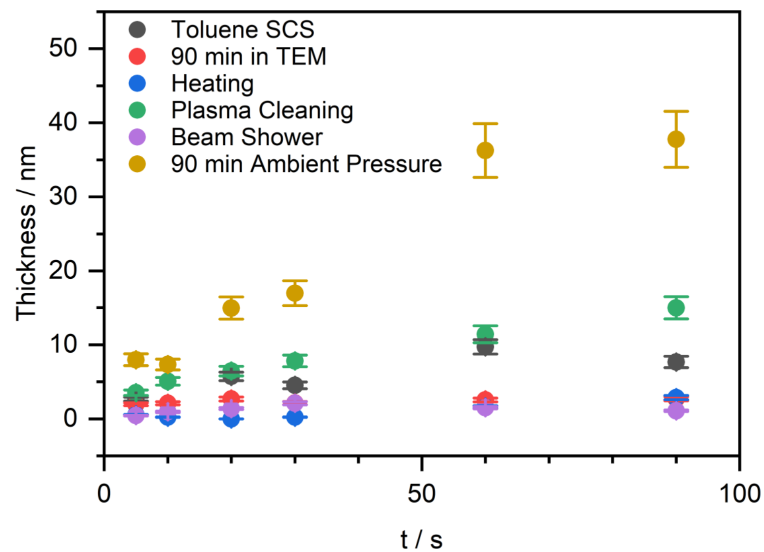

Figure 4.11: Contamination thickness in the inner part of areas exposed to the electron beam of grids prepared with toluene and pre-treated by different established methods. Measurements covering the whole range of exposure times are shown in (a), with the data with exposure times up to 100 s are shown enlarged in (b).

The thickness of the carbon film outside of the exposed areas (fig. 4.12) is in the same

range as that of the carbon film of the samples treated in the SCS and of that remaining in the microscope for 90 min. After plasma cleaning, the carbon film was not etched as in the case of the empty grid (see section 4.4.3), as additional carbonaceous material was added by applying the solvent, though longer cleaning times would also be probably abrasive. Beam showering the sample resulted in a 1.5 times higher thickness than achieved with the previously discussed techniques. This is caused by the high VOC load of the sample when it is inserted in the microscope and immediately exposed to the beam. The increased carbon film thickness (and therefore a thicker sample in the regions of interest) might be a disadvantage in some TEM experiments. Also, drying the sample at ambient pressure leads to a slightly increased carbon film thickness, making drying at ambient pressure the least promising method that should be avoided if other methods can be employed.

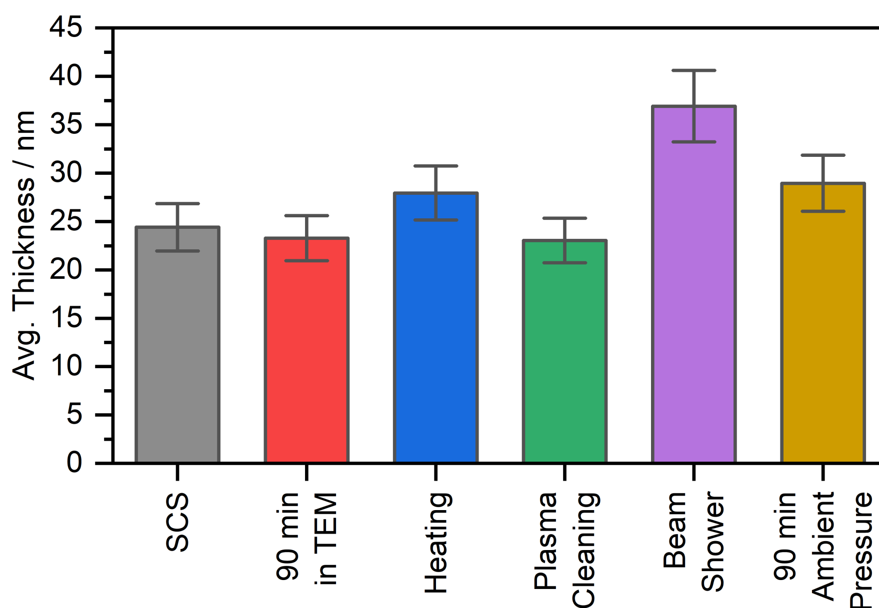

Figure 4.12: Carbon film thickness of grids prepared with toluene after applying different cleaning treatments for hydrocarbon removal.

4.4.5 Nanoparticle samples cleaned by SCS

The efficiency of the cleaning station was tested by investigating different samples of metal phosphide nanoparticles, namely MoP and CoP particles[30]. The particles were dispersed in either THF or toluene and did not react with the selected solvent. Some of these nanoparticle samples were stabilized by supported ionic liquid phase, and therefore contain a high amount of carbon. Overall, this type of sample is prone to contamination and achieving clean measurement data without contamination can be challenging. Consequently, pretreatment of these samples by plasma cleaning or other abrasive techniques is not possible, given the decomposition these cause. Given this, we used our SCS for cleaning these samples. The specimens were prepared by deposing 1 µL of dispersed sample on a TEM grid before drying them in the SCS for the durations determined in section 4.4.1, so samples prepared with THF or toluene were dried for either 30 min or 90 min. For comparison, samples were also investigated after the same drying time at ambient pressure. In fig. 4.13, MoP@SILP particles were prepared in THF and investigated without any further pretreatment in the TEM. Though the contamination is quite low, the margins of the area scanned for EDX acquisition are visible due to contamination.

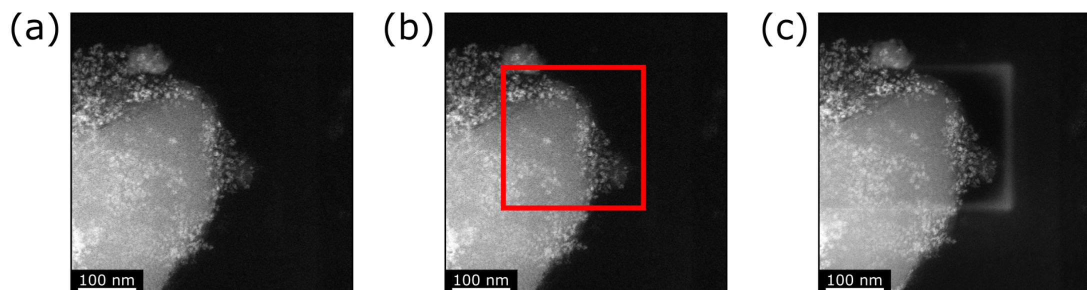

Figure 4.13: High-angle annular dark-field imaging (HAADF) results for MoP@SILP particles dispersed in THF and dried at ambient pressure for 30 min (a) before EDX acquisition. (b) The marked area was investigated by EDX (256×256 px^2, 10 µs dwell time, 204 kx magnification, 601 frames).(c) shows an image of the area after EDX acquisition.

In fig. 4.14, similar CoP@SILP particles were also dispersed in THF and analyzed after the sample was dried for 30 min in the SCS. Here, no contamination residues were visible

after EDX analysis. For both samples, the same EDX parameters were chosen.

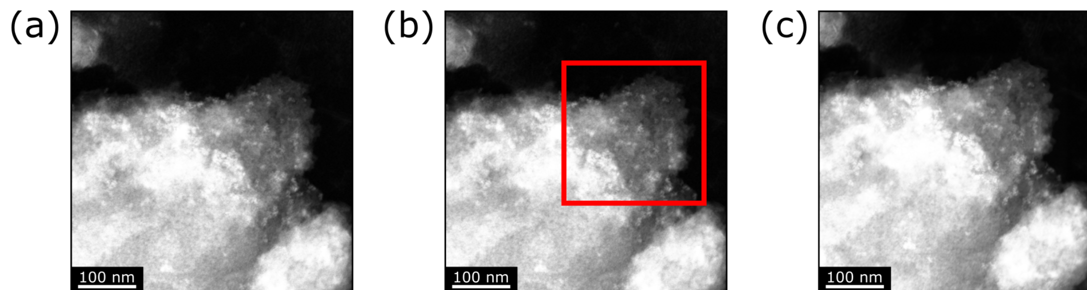

Figure 4.14: HAADF images of CoP@SILP particles dispersed in THF prepared by drying the sample in the SCS for 30 min (a) before EDX acquisition. (b) The marked area was investigated by EDX (256 × 256 px^2, 10 µs dwell time, 204 kx magnification, 601 frames). (c) shows an image of the area after EDX acquisition.

A MoP nanoparticle sample dried for 90 min at ambient pressure in shown in fig. 4.15. Though the EDX acquisition parameters were similar, here significant contamination has accumulated.

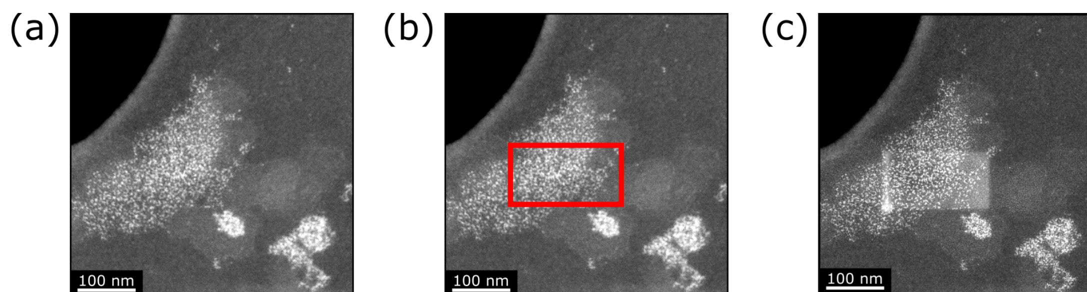

Figure 4.15: HAADF images of MoP nanoparticles dispersed in toluene and dried for 90 min at ambient pressure (a) before EDX acquisition. (b) The marked area was investigated by EDX (423 × 282 px^2, 10 µs dwell time, 816 kx magnification, 690 frames). (c) shows an image of the area after EDX acquisition.

For comparison, fig. 4.16 show a sample of MoP nanoparticles dispersed in toluene. When preparing the specimen, the grid was dried in the SCS for 90 min before insertion into the TEM. Despite the high magnification and high number of frames, no contamination could be observed after EDX acquisition. The sample prepared in our cleaning station showed

less carbon contamination in the investigated area, which therefore advocates preparation with the SCS.

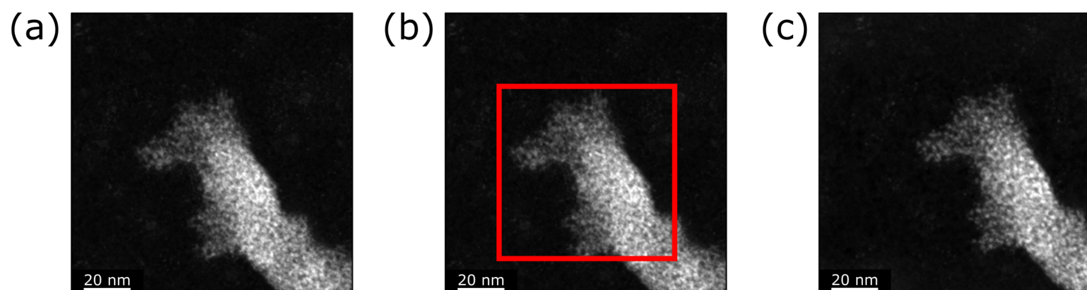

Figure 4.16: HAADF images of MoP nanoparticles dispersed in toluene prepared by drying the sample in the SCS for 90 min (a) before EDX acquisition. (b) The marked area was investigated by EDX (319×312 px^2, 10 µs dwell time, 816 kx magnification, 701 frames). (c) shows an image of the area after EDX acquisition.

4.5 Conclusions

In comparison to other cleaning methods, our suggested cleaning by vacuum removal of contaminants performed very well. Though each method has its advantages and disadvantages, our SCS removes adsorbed hydrocarbon molecules very efficiently without altering the sample. Plasma cleaning removes contamination successfully and is helpful for keeping the equipment, e.g., sample holders clean, but is quite abrasive and not suitable for samples containing carbon. Ozone cleaning has been dismissed for our experiments: While the carbon film gets thinned, the hydrocarbons that are broken down are not removed successfully. We note that longer pumping times after the ozone treatment might be beneficial. Heating the sample reduces the contamination, though there is the possibility that the high temperatures change the properties of the sample. Beam showering a sample is by far the most efficient method for mitigating carbon contamination, though the disadvantages must not be neglected: Residual hydrocarbons are present on the TEM sample and still get inserted in the TEM, where they contaminate the volume close to the sample, as only a small area of the grid gets cleaned. In addition, this method is time consuming,

as cleaning can only proceed during the time the sample is in the TEM. In addition, it was also found that this method increases the overall sample thickness. Drying at ambient pressures does not require any additional equipment in the preparation process, though depending on the solvent, it may take a long time to mitigate contamination.

In this work we have shown that our sample cleaning setup represents a powerful alternative in the sample preparation of TEM specimens. With customized cleaning procedures, it is possible to remove undesired organic contamination caused by the specimen preparation. These clean specimens allow for TEM investigations, while being barely contaminated in the areas of interest, and have a clean vacuum environment. Moreover, the opportunity to prepare samples in advance and store them and other TEM equipment (e.g., empty grids) in a clean environment is helpful. How well the SCS performs could also be demonstrated for the example of MoP and CoP nanoparticle samples dispersed in either THF or toluene, for which we could achieve excellent results by cleaning the samples beforehand in our SCS. Customized cleaning protocols based on a sample's properties can be utilized to remove undesired hydrocarbons and represent a novel approach to achieve high-quality TEM data.

4.6 Supporting information

Fit parameter of the parabolic rate behaviour

The contamination growth with longer exposure times follows a parabolic fit behaviour, which is in agreement with similar results found in literature[25]. The fit function is given by eq. (4.5), with d_V being the accumulated contamination volume, $K_{p,V}$ the parabolic rate constant and c_V a sample-specific constant.

$$d_V = \sqrt{t} \cdot K_{p,V} + c_V \tag{4.5}$$

The values for the fit functions are given in table 4.2. In addition, the coefficient of determination R^2 is also listed. The data with the according fit functions is shown in fig. 4.17 and fig. 4.18.

Sample	$K_{p,V}$ / $\frac{nm^3}{\sqrt{t}}$	c_V / nm^3	R^2
Grid empty	54856	-153001	0.98735
Grid empty SCS	40276	-90788	0.99496
Ozone cleaning empty	26326	-93539	0.94623
Plasma cleaning empty	8457	-21677	0.99110
Toluene 90 min SCS	26584	-6125	0.92925
THF 30 min SCS	3595	-12437	0.97252
Toluene plasma cleaning	3176	-59503	0.97598
Toluene heating	6622	-27277	0.94077
Toluene beam shower	1122	-1507	0.89880
Toluene 90 min ambient pressure	122237	-466004	0.96458
Toluene 90 min TEM	29140	-7613	0.96424

Table 4.2: Fit parameters $K_{p,V}$ and c_V as well as coefficient of determination R^2 for the fit of the contamination following a parabolic law behaviour of the different investigated samples.

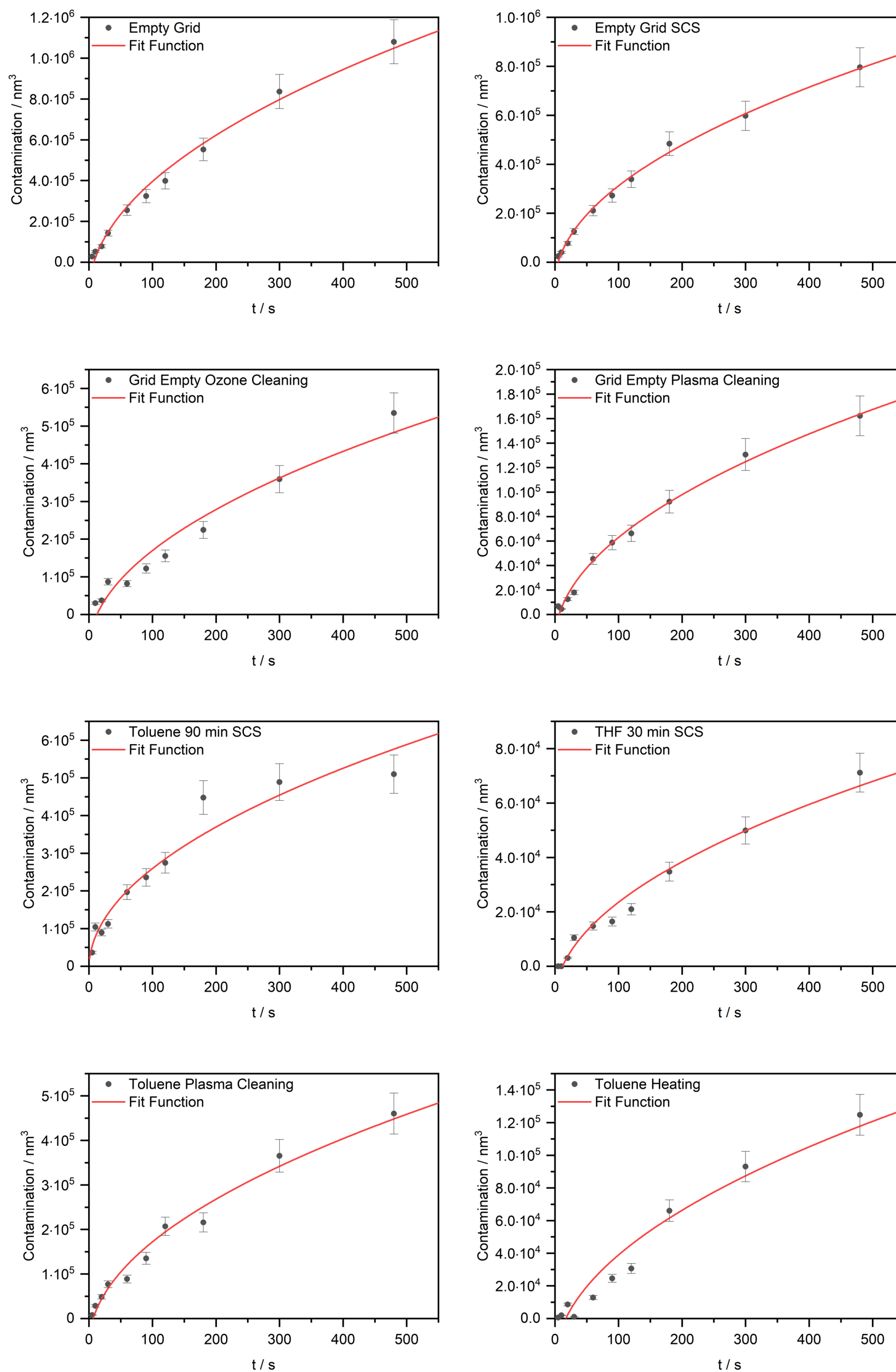

Figure 4.17: Data (dots) and parabolic rate fit (red line) for the contamination of samples prepared with different methods.

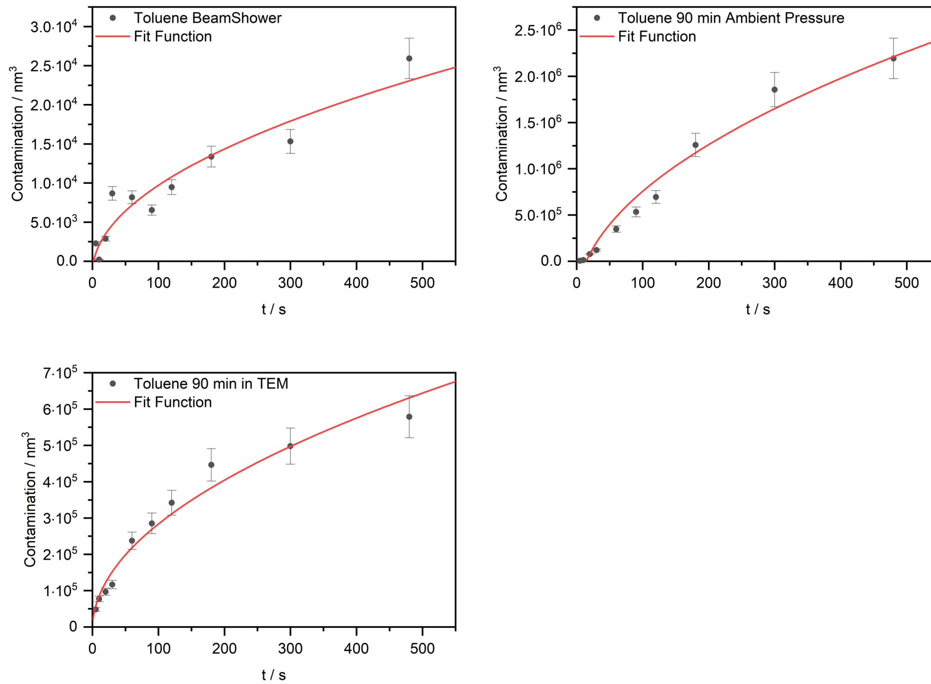

Figure 4.18: Data (dots) and parabolic rate fit (red line) for the contamination of samples prepared with different methods.

The separate thickness measurements in the inner portions of the areas exposed to the electron beam are shown in fig. 4.19 and fig. 4.20. If the data can be fitted by a parabolic rate behavior, these are included as well.

The fit function is described by eq. (4.6), with d_T being the contamination thickness, $K_{p,T}$ the parabolic rate constant and c_T a sample-specific constant.

$$d_T = \sqrt{t} \cdot K_{p,T} + c_T \tag{4.6}$$

Sample	$K_{p,T}$ / $\frac{nm}{\sqrt{t}}$	c_T / nm	R^2
Grid empty	4.1665	-9.1474	0.99601
Grid empty SCS	2.6088	-5.2703	0.99391
Ozone cleaning empty	3.0973	-11.6848	0.98353
Plasma cleaning empty	0.6168	-1.7661	0.99607
Toluene 90 min SCS	-	-	-
THF 30 min SCS	-	-	-
Toluene plasma cleaning	1.7245	-0.8137	0.98714
Toluene heating	0.5197	-1.7239	0.91163
Toluene beam shower	0.21891	0.06933	0.84526
Toluene 90 min ambient pressure	-	-	-
Toluene 90 min TEM	-	-	-

Table 4.3: Fit parameters $K_{p,V}$ and c_V as well as coefficient of determination R^2 for the fit of the contamination following a parabolic law behaviour of the contamination thickness of different investigated samples.

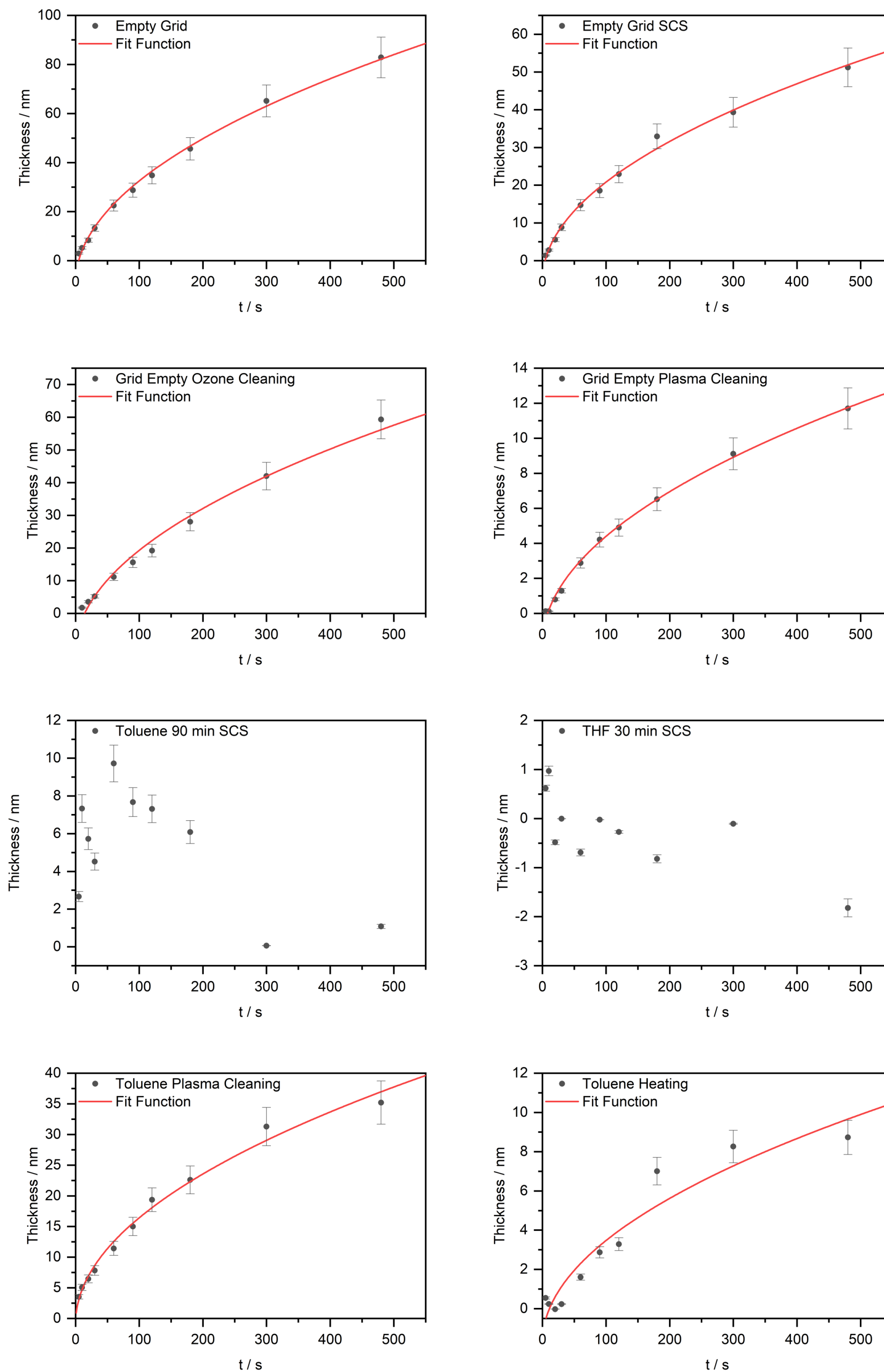

Figure 4.19: Data (dots) and if it applies the parabolic rate fit (red line) for the contamination thickness of samples prepared with different methods.

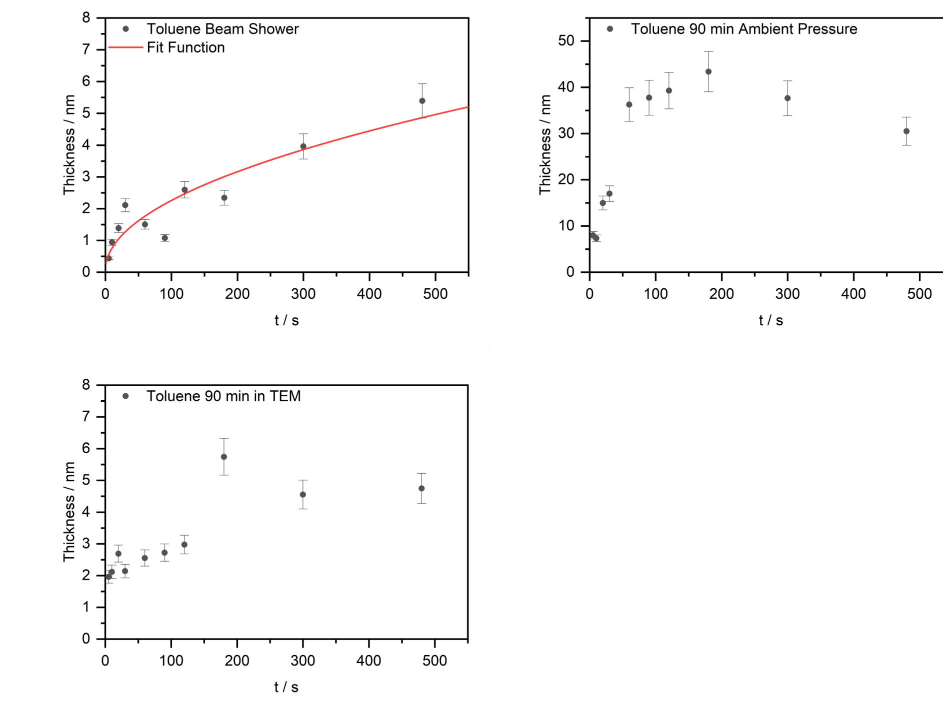

Figure 4.20: Data (dots) and if it applies the parabolic rate fit (red line) for the contamination thickness of samples prepared with different methods.

References

[1] Bordet, A., Leitner, W., 2021. Metal Nanoparticles Immobilized on Molecularly Modified Surfaces: Versatile Catalytic Systems for Controlled Hydrogenation and Hydrogenolysis. Accounts of Chemical Research 54, 2144–2157. doi:10.1021/acs.accounts.1c00013.

[2] Egerton, R.F., Li, P., Malac, M., 2004. Radiation damage in the TEM and SEM. Micron 35, 399–409. doi:10.1016/j.micron.2004.02.003.

[3] Egerton, R.F., Rossouw, C.J., 1976. Direct measurement of contamination and etching rates in an electron beam. Journal of Physics D: Applied Physics 9, 659–663. doi:10.1088/0022-3727/9/4/016.

[4] Ennos, A.E., 1953. The origin of specimen contamination in the electron microscope. British Journal of Applied Physics 4, 101–106. doi:10.1088/0508-3443/4/4/302.

[5] Ennos, A.E., 1954. The sources of electron-induced contamination in kinetic vacuum systems. British Journal of Applied Physics 5, 27–31. doi:10.1088/0508-3443/5/1/307.

[6] Gatzen, H.H., Saile, V., Leuthold, J., 2005. Micro- and Nanofabrication. 1st ed., Springer-Verlag Berlin Heidelberg. doi:10.1201/9781420028270.ch1.

[7] Goh, Y.M., Schwartz, J., Rennich, E., Ma, T., Kerns, B., Hovden, R., 2020. Contamination of TEM Holders Quantified and Mitigated with the Open-Hardware, High-Vacuum Bakeout System. Microscopy and Microanalysis 26, 906–912. doi:10.1017/S1431927620001762.

[8] Griffiths, A.J.V., Walther, T., 2010. Quantification of carbon contamination under electron beam irradiation in a scanning transmission electron microscope and its suppression by plasma cleaning. Journal of Physics: Conference Series 241, 3–7. doi:10.1088/1742-6596/241/1/012017.

[9] Grinham, R., Chew, A., 2017. A Review of Outgassing and Methods for its Reduction. Applied Science and Convergence Technology 26, 95–109. doi:10.5757/asct.2017.26.5.95.

[10] Hansen, R.W.C., Bissen, M., Wallace, D., Wolske, J., Miller, T., 1993. Ultraviolet / ozone cleaning of carbon-contaminated optics. Applied Optics 32, 4114–4116. doi:10.1364/AO.32.004114.

[11] Haynes, W. M., E., 2017. CRC Handbook of Chemistry and Physics. 97th ed., CRC Press/Taylor Francis, Boca Raton, FL. doi:10.1201/9781315380476.

[12] Held, J.T., Hunter, K.I., Dahod, N., Greenberg, B., Reifsnyder Hickey, D., Tisdale, W.A., Kortshagen, U., Mkhoyan, K.A., 2018. Obtaining Structural Parameters from STEM-EDX Maps of Core/Shell Nanocrystals for Optoelectronics. ACS Applied Nano Materials 1, 989–996. doi:10.1021/acsanm.7b00398.

[13] Hirsch, P., Kässens, M., Püttmann, M., Reimer, L., 1994. Contamination in a scanning electron microscope and the influence of specimen cooling. Scanning 16, 101–110. doi:10.1002/sca.4950160207.

[14] Hren, J.J., 1978. Specimen Contamination in Analytical Electron Microscopy: Sources and Solutions. Ultramicroscopy 3, 375–380. doi:10.1016/S0304-3991(78)80057-6.

[15] Isabell, T.C., Fischione, P.E., O'Keefe, C., Guruz, M.U., Dravid, V.P., 1999. Plasma cleaning and its applications for electron microscopy. Microscopy and Microanalysis 5, 126–135. doi:10.1017/S1431927699000094.

[16] Jousten, K., 1999. Thermal outgassing, in: CAS - CERN Accelerator School : Vacuum Technology, pp. pp.111–125. doi:10.5170/CERN-1999-005.111.

[17] Jousten, K., 2018. Handbuch Vakuumtechnik. 12th ed., Springer Fachmedien Wiesbaden. doi:10.1007/978-3-658-13386-3.

[18] Joy, D.C., Romig, A.D., Goldstein, J.I., 1986. Principles of Analytical Electron Microscopy. 1st ed., Springer New York, NY. doi:10.1007/978-1-4899-2037-9.

[19] Kohl, H., Reimer, L., 2008. Transmission Electron Microscopy Physics of Image Formation. 5th ed., Springer New York. doi:10.1007/978-0-387-40093-8.

[20] Li, C., Pedrazo Tardajos, A., Wang, D., Choukroun, D., Van Daele, K., Breugelmans, T., Bals, S., 2021. A simple method to clean ligand contamination on TEM grids.

Ultramicroscopy 221, 113195. doi:10.1016/j.ultramic.2020.113195.

[21] Malis, T., Cheng, S.C., Egerton, R.F., 1988. EELS log-ratio technique for specimen-thickness measurement in the TEM. Journal of Electron Microscopy Technique 8, 193–200. doi:10.1002/jemt.1060080206.

[22] McGilvery, C.M., Goode, A.E., Shaffer, M.S.P., McComb, D.W., 2012. Contamination of holey/lacey carbon films in STEM. Micron 43, 450–455. doi:10.1016/j.micron.2011.10.026.

[23] Middleman, K.J., Herbert, J.D., Reid, R.J., 2007. Cleaning stainless steel for use in accelerators-Phase 1. Vacuum 81, 793–798. doi:10.1016/j.vacuum.2005.11.057.

[24] Mitchell, D.R.G., 2006. Determination of mean free path for energy loss and surface oxide film thickness using convergent beam electron diffraction and thickness mapping: A case study using Si and P91 steel. Journal of Microscopy 224, 187–196. doi:10.1111/j.1365-2818.2006.01690.x.

[25] Mitchell, D.R.G., 2015. Contamination mitigation strategies for scanning transmission electron microscopy. Micron 73, 36–46. doi:10.1016/j.micron.2015.03.013.

[26] Pradhan, S., Hedberg, J., Blomberg, E., Wold, S., Odnevall Wallinder, I., 2016. Effect of sonication on particle dispersion, administered dose and metal release of non-functionalized, non-inert metal nanoparticles. Journal of Nanoparticle Research 18, 1–14. doi:10.1007/s11051-016-3597-5.

[27] Priyadarshi, A., Khavari, M., Subroto, T., Prentice, P., Pericleous, K., Eskin, D., Durodola, J., Tzanakis, I., 2021. Ultrasonics Sonochemistry Mechanisms of ultrasonic de-agglomeration of oxides through in-situ high-speed observations and acoustic measurements. Ultrasonics Sonochemistry 79, 105792. doi:10.1016/j.ultsonch.2021.105792.

[28] Reimer, L., Wächter, M., 1978. Contribution to the contamination problem in transmission electron microscopy. Ultramicroscopy 3, 169–174. doi:10.1016/S0304-3991(78)80023-0.

[29] Rykaczewski, K., Marshall, A., White, W.B., Fedorov, A.G., 2008. Dynamic growth

of carbon nanopillars and microrings in electron beam induced dissociation of residual hydrocarbons. Ultramicroscopy 108, 989–992. doi:10.1016/j.ultramic.2008.04.006.

[30] Sodreau, A., Zahedi, H.G., Dervişoğlu, R., Kang, L., Menten, J., Zenner, J., Terefenko, N., DeBeer, S., Wiegand, T., Bordet, A., Leitner, W., 2023. A Simple and Versatile Approach for the Low-Temperature Synthesis of Transition Metal Phosphide Nanoparticles from Metal Chloride Complexes and $P(SiMe_3)_3$. Advanced Materials , 2306621doi:10.1002/adma.202306621.

[31] Soong, C., Woo, P., Hoyle, D., 2012. Contamination Cleaning of TEM/SEM Samples with the ZONE Cleaner. Microscopy Today 20, 44–48. doi:10.1017/s1551929512000752.

[32] Vig, J., Le Bus, J., 1976. UV / Ozone of Surfaces. IEEE Transactions on Parts, Hybrids, and Packaging 12, 365–370. doi:10.1116/1.573115.

[33] Weigert, F., Müller, A., Häusler, I., Geißler, D., Skroblin, D., Krumrey, M., Unger, W., Radnik, J., Resch-Genger, U., 2020. Combining HR-TEM and XPS to elucidate the core–shell structure of ultrabright CdSe/CdS semiconductor quantum dots. Scientific Reports 10, 1–15. doi:10.1038/s41598-020-77530-z.

5 Conclusions and outlook

In this work, the crucial importance of a careful sample preparation of TEM specimens to mitigate carbon contamination was demonstrated. The influence of different aspects on the sample preparation, i.e., the solvents used for the sample preparation, variations of the drying time, the time a sample remains in the vacuum of the microscope and established cleaning methods, was assessed by quantitative analysis of both the gas environment within the octagon and the accumulated carbon contamination resulting from electron beam exposure.

Analysis of contaminant outgassing from samples in a decommissioned octagon at ETEM pressure was performed by PTR MS experiments. The investigated samples employed solvents typically used in chemical synthesis. After inserting the sample holder, outgassing solvent molecules were measured in long-term experiments over up to 14 h. It was found that the solvent's ion count signal decreased over the duration of the measurement. However, for all but one sample, the ion count rate was found to be higher after this duration compared to measurements before the sample holder was inserted. These result indicate significant outgassing and therefore changes in the supposedly controlled gas composition in the ETEM. While the PTR MS measurements were performed at ETEM pressure to study adsorption of VOCs to the surfaces, the octagon was pumped to a TEM pressure range of 10^{-7} mbar for intervals. It became clear that in addition to changes in the gas composition, also adsorption to the surfaces in the octagon remain a source of contamination for further experiments. While longer pumping durations decrease the contaminant signal intensity, residual VOCs remain in the octagon. Plasma cleaning, which is typically an efficient tool for the removal of carbon contaminants in electron microscopy, was applied to remove remaining solvent contamination. It was possible to reduce contamina-

tion to achieve a state of cleanliness similar to that before the sample holder was inserted. However, this was a tedious process, as hours of plasma cleaning were necessary, while, for comparison, TEM samples are typically cleaned for durations in the range of seconds.

Combining all results, it was found for the different investigated samples that a higher vapor pressure and longer drying time lead to less contamination accumulating in the gas phase of the octagon. The experiments in the octagon show that once VOCs accumulate in the microscope, contaminants remain for a long time in the direct sample environment. It can be assumed that once this happens, even several measurement cycles later additional contaminants might impair TEM experiments and influence the ETEM gas environment.

Experiments in the octagon at ETEM pressure indicate troublesome changes in the gas composition and on octagon surfaces when a sample outgases at this pressure range. However, by using this setup, the impact of the electron beam on the sample during TEM experiments could not be investigated. Therefore, the contamination caused by electron beam exposure in the microscope, the choice of different solvents, the drying time, and the influence of the duration a sample remains in the microscope were quantified by EELS.

Solvents from synthesis (THF and toluene) and solvents typically used by electron microscopists (MeOH, EtOH and iPrOH) were investigated, while mesitylene was dismissed as it was proven to be not suitable for electron microscopy in the octagon experiments. For these experiments, samples were exposed to the electron beam for different durations, as the accumulated contamination increases by diffusion of contaminants towards the electron beam. Like in the octagon experiments, a higher vapor pressure and longer drying times of the solvent samples resulted in less contamination. In addition, the influence of drying the sample before inserting it in the microscope was compared to outgassing of the sample in the high vacuum in the octagon. Here, it was observed that longer drying times before sample insertion were beneficial for the cleanliness of a measurement, while for the octagon, spatial limitations restricted the vacuum removal of contaminants.

Depending on the selected solvent, the accumulated contamination varies in both the

octagon setup and in TEM experiments. It is important to note that it is not always possible to choose a volatile solvent, because a solvent's characteristics need to match the sample's properties to assure that no undesired effects alter them. Therefore, a need for mitigation strategies emerges. Established cleaning methods have been applied and assessed based on accumulated contamination. However, all of these methods come with their own advantages and disadvantages. Ozone and plasma cleaning are abrasive and remove carbonaceous compounds well, though this also applies for the carbon film of TEM grids and sample components. Heating a sample can remove VOCs well, however the chance of altering the samples properties must not be neglected. Also, a clean, preferably inert atmosphere is necessary to prevent oxidation. Heating a sample within the microscope leads to outgassing in the microscope environment, which has been shown to be an issue in previous mentioned experiments. This also applies for beam showering a sample, which otherwise is a promising approach for local cleaning. In addition, for both heating and cooling a sample, a designated sample holder is required, making these methods not easily accessible.

In a novel approach, TEM samples were cleaned in a newly designed SCS, which allows for the removal of VOCs by establishing a vacuum and heating. As it was found that spatial restrictions impede the vacuum removal of contaminants, the setup dimensions were scaled up relative to the gap between the pole pieces of the microscope. When investigating specimens prepared in the SCS by EELS thickness measurements, the area exposed in STEM mode was barely contaminated, though at the borders of the scanned area, some contamination accumulated. Moreover, the carbon film had approximately retained the same thickness as before treatment in the SCS. The efficiency of the SCS was not only studied for solvent samples, but also by investigating metal phosphide nanoparticle samples. Particles of either MoP or CoP were dispersed in toluene and THF and dried in the SCS for removing solvent residues. For obtaining information by EDX analysis, extended beam exposure times were required for obtaining a sufficient signal intensity in the detectors. Despite long exposure times and high magnifications, the investigated

areas were not visibly contaminated after EDX analysis. For comparison, when the samples were dried at ambient pressure, there was some accumulated carbon contamination observable after EDX acquisition with the same parameters.

In the octagon investigations of contamination, the VOCs were investigated in an inert atmosphere. As many catalytic experiments require a reactive gas atmosphere, further investigation of contamination under a different gas environment might be of interest. Depending on the sample, many TEM parameters can be adjusted to characterize a sample with the best results. In the studies of this thesis, the focus was on different solvents and the drying parameters. Further experiments can give insight in how to optimize TEM results by variation of other parameters, for example the acceleration voltage or the probe current. To optimize the sample preparation, further experiments utilizing the SCS with additional heating might be of interest. This might offer the opportunity to remove even more persistent solvents, which would be of interest in chemical synthesis but not favorable for TEM experiments. The SCS can be integrated in these workflows for TEM experiments. The device is helpful for storing used equipment, e.g., the grids or sample holder, in an environment with low contamination that is unaffected by outgassing residual solvent molecules. Moreover, time-consuming cleaning of the prepared samples before measuring them in the TEM saves valuable measurement time.

Overall, the conclusions of this thesis are that there is significant potential for improving the cleanliness of TEM experiments of samples containing high amounts of carbon. The main factors contributing to contamination are the solvent's physical properties, i.e., vapor pressure and boiling point, and the drying conditions, i.e., no spatial restrictions and sufficiently long drying times. This insight can also be extended to other solvents. While samples such as the studied ones are typically prone to contamination, the right choice of solvent and suitable cleaning techniques can greatly improve the quality of measurements. Based on the results presented in this thesis, it is possible to utilize sample-specific preparation steps to achieve lower contamination in TEM measurements. All samples containing solvents benefited from longer drying times, making this the most

crucial and yet easiest step to consider during the preparation; simply speaking: preventing contaminants from entering the microscope is easier then removing them afterwards. In conclusion, diligence and patience in the preparation of TEM specimens open a door for obtaining high-resolution data for difficult samples prone to contamination.

Acknowledgements

During my time as a doctoral student, many people have supported me and given me guidance. Without these people, the research and writing of this thesis would not have been possible.

First, I would like express my gratitude to Prof. Dr. Robert Schlögl for offering me the opportunity to conduct my research under his supervision at the FHI in Berlin and the MPI CEC in Mülheim. I have always appreciated the feedback that has set the right direction for the next steps in my research and am thankful for engaging me in this research topic, which I truly enjoyed working on.

I would also like to thank Prof. Dr. Andreas Hütten for agreeing to be the second supervisor for my doctoral examination.

A special thanks goes to Dr. Walid Hetaba for his work as my group leader. I appreciate that you have shared your in-depth knowledge on electron microscopy and provided comprehensive feedback on my work. Also, I am glad that you have always educated us in Austrian culture and making me aware of my usage of the "rheinischer Imperativ".

Many colleagues have made my first year as a student in Berlin remarkable: I would like to thank Dr. Thomas Lunkenbein for his work as my group leader there, but also Dr. Liudmyla Masliuk, Dr. Thomas Götsch and Dr. Gerardo Algara-Siller for their support and encouragement.

In Mülheim, my work was also accompanied by many amazing colleagues. I would like to thank Dr. Holger Ruland, Dr. Jorge Salazar Gómez and Dr. Corina Pollok as well as Alina Ernst for always supporting me with their knowledge and equipment regarding any questions about gas analysis. In addition, I thank Dr. Simon Ristig for helping out with his CAD software skills and Dr. Marc Tesch and Sven Kubala for passing on their deep experience on vacuum technique on the fly and conveying all the tips and tricks when building a setup that are nowhere written down. I cannot imagine doing my TEM

experiments without Dr. Daniela Ramermann. Though I am confident that stop watches will haunt her after countless TEM sessions, her help during my TEM measurements hes been indispensable.

I would also like to thank Thermo Fisher Scientific and Dr. Stephan Kujawa for letting me investigate contamination in TEM with the help of their Octagon setup.

I am especially grateful for the support of Dr. Alexis Bordet, Hooman Ghazi Zahedi and Johannes Zenner for providing me with samples for my TEM experiments. I appreciate that you were always willing to help me when I went on a quest to find "a sample that most microscopists would like to refuse due to contamination".

Furthermore, I would like to thank my colleagues Dr. Elisabeth Hetaba-Wolf, Melina Müller, Lea Kreuzheide and Agnes Stoer for always being there for me and for either talking about my dissertation project or for chatting about topics as far away from it as possible.

Finally, I would like to thank my parents and my partner for their unconditional support, their patience and their encouragement, without which all of this would not have been possible.

List of figures

1.1 Schematic overview of the most important TEM components in a Thermo Scientific Talos F200X microscope. 2
1.2 EDX spectrum of a Fe_3O_4 sample. 5
1.3 Zero loss, low loss and core loss regions of EELS spectra of a Fe_3O_4 sample. 6
1.4 Volatile contaminants surround the sample environment and form amorphous carbon when exposed to the electron beam. 8
1.5 HRTEM image of an Al-4Cu-1Li-0.25Mn alloy with a precipitate. Sample provided by Ines Häusler, image taken by Walid Hetaba. 10
1.6 Functionalized carbon nanotube sample before and after scanning the sample for 2 min. Sample provided by Wenchao Wan, images taken by Norbert Pfänder. 11
1.7 HAADF and BF images of manganese nanoparticles before and after EDX analysis. 13
1.8 Spectra of the first 50 (black) and the last 50 scans (red) obtained during EDX analysis. 13
1.9 HAADF images at the beginning and end of EDX acquisition. The investigated area is shown enlarged as well as a similar area without contamination. 15
1.10 EELS measurements of contamination resulting from toluene after background subtraction (black) and after deconvolution of the carbon K-edge (red). 16
1.11 EEL spectrum of the carbon K-edge of the amorphous carbon film of a TEM grid and of a sample of THF. 17
1.12 EELS measurements of the carbon K-edge of the investigated solvents. . . 18

1.13 Normalized carbon K-edge EEL spectra of contamination resulting from different solvents. 20
1.14 Different flow regimes of particles in a vacuum, viscous flow and molecular flow. 24
1.15 Schematic overview of physical processes that influence the pressure when pumping a setup from ambient to low pressure. 26
1.16 EEL spectra of toluene samples dried for 30 min or 10 min before being exposed to the electron beam for 180 s. 31
1.17 Gas flow scheme of a PTR TOF mass spectrometer. 32
1.18 Schematic overview of the steps required for achieving corrected time traces out of PTR MS raw data. 33

2.1 Distribution of different setup components across the eight octagon ports. . 51
2.2 Photo of octagon with its different ports. 52
2.3 Photo of octagon setup and its main components. 53
2.4 Long-term measurements of mesitylene contamination resulting from samples dried for 30 min and 60 min. 58
2.5 Long-term measurement of toluene samples dried for 10 min and 30 min before inserting the samples in the octagon. 59
2.6 Long-term measurement of THF samples dried for 10 min and 30 min before inserting the samples in the octagon. 60
2.7 Ion count rate of MES10, MES30 and MES60 depending on the vacuum pumping duration. 61
2.8 Ion count rate of TOL10 and TOL30 depending on the vacuum pumping duration. 62
2.9 Ion count rate of THF10 and THF30 depending on the vacuum pumping duration. 63
2.10 Ion count rate of MES10, MES30 and MES60 after plasma cleaning for different time intervals. 64

2.11 Ion count rate for TOL10 and TOL30 after plasma cleaning for different time intervals. 65
2.12 Ion count rate of THF10 and THF30 after plasma cleaning for different time intervals. 66
2.13 Ion count rate of H_2O-H_3O^+ clusters and the parasitic ions NO^+ and O_2^+ in measurements of samples containing mesitylene, toluene and THF . . . 68
2.14 Spectrum of the raw data taken by measuring the nitrogen gas supply. . . 70
2.15 Raw data in a range between m/z 50 and m/z 60 of the nitrogen gas supply only and the nitrogen gas supply passing through the octagon. 71
2.16 Concentration of MES30 and MES60 determined in long-term measurements while the sample holder is inserted in the octagon. 80
2.17 Concentration of TOL10 and TOL30 determined in long-term measurements while the sample holder is inserted in the octagon. 81
2.18 Concentration of THF10 and THF30 determined in long-term measurements while the sample holder is inserted in the octagon. 81
2.19 Concentration of MES10, MES30 and MES60 after pumping the octagon to TEM pressure for different durations. 82
2.20 Concentration of TOL10 and TOL30 after pumping the octagon to TEM pressure for different durations. 82
2.21 Concentration of THF10 and THF30 after pumping the octagon to TEM pressure for different durations. 83
2.22 Concentration of MES10, MES30 and MES60 after different plasma cleaning intervals. 83
2.23 Concentration of TOL10 and TOL30 after different plasma cleaning intervals. 84
2.24 Concentration of THF10 and THF30 after different plasma cleaning intervals. 84
2.25 Ion count rate of NH_3^+ ions during PTR MS experiments with mesitylene, toluene and THF. 85

2.26 Ion count rate of NH_4^+ ions during PTR MS experiments with mesitylene, toluene and THF. 85
2.27 Ion count rate of N_2H^+ ions during PTR MS experiments with mesitylene, toluene and THF. 85
2.28 Raw data of the nitrogen gas supply only (black) and the nitrogen gas supply passing through the octagon (red)in m/z 10 wide ranges centered on m/z 45 and 65 (top row), m/z 75 and 85 (middle row) and 95 and 105 (bottom row). 86
2.29 Raw data of the nitrogen gas supply only (black) and the nitrogen gas supply passing through the octagon (red) for the m/z 110–120 and 120–130 ranges (top row) and the m/z 130–140 and 140–150 ranges (bottom row). 87

3.1 Carbon contamination of a grid prepared with 1 µL iPrOH and dried for 30 min before insertion into the microscope. The scanned area was exposed to the electron beam for 300 s before EELS data acquisition. 98
3.2 Carbon contamination accumulated by electron beam exposure of different solvents. All samples were dried for 30 min before inserting the specimens in the microscope. 100
3.3 Comparison of contamination accumulated by solvent samples dried for 10 min or 30 min. 102
3.4 Contamination resulting from solvent samples dried for 30 min before TEM investigation immediately after sample insertion and 30 min later. 104
3.5 Contamination of MeOH samples dried for either 10 min or 30 min at ambient pressure immediately and 30 min after inserting the sample into the TEM. 105
3.6 Difference in accumulated contamination when comparing a sample with a drying time of 30 min to a sample dried for 10 min. 106

3.7 Difference in accumulated contamination between a sample remaining 30 min in the microscope and a sample measured immediately after insertion into the TEM. The drying times of the samples were either 10 min or 30 min before insertion. 107
3.8 Accumulated contamination from wet and dry solvent samples of MeOH and EtOH dried for 30 min before sample insertion. 108
3.9 Data and parabolic rate fit of the solvents THF and MeOH for different drying times and times remaining in the microscope. 111
3.10 Data and parabolic rate fit of the solvents EtOH and iPrOH for different drying times and times remaining in the microscope. 112
3.11 Data and parabolic rate fit of the solvent toluene for different times remaining in the microscope. 113
3.12 Data of all toluene measurements (a), with the first 100 s of beam exposure time shown enlarged in (b). 113
3.13 Data of all THF, MeOH, EtOH and iPrOH measurements (a), with the first 100 s of beam exposure time shown enlarged in (b). 114
3.14 Accumulated contamination from wet and dry solvent samples of MeOH and EtOH dried for 30 min before sample insertion. 115

4.1 Working principle of our SCS with its components, with different temperature zones resulting in a contamination gradient, and different temperature zones. 126
4.2 CAD drawing of the assembly of our SCS Setup with its most important components. 127
4.3 Close-up of the sample chamber of the SCS. 128
4.4 (a) Pressure of THF, toluene and the reference measured above the cooler, with the data in the green box shown enlarged in (b). 131
4.5 (a) Pressure of THF , toluene and the reference measured below the cooler, with the data in the green box are shown enlarged in (b). 132

4.6 EELS thickness map of different areas considered in the evaluation of a sample of toluene, that was dried for 90 min at ambient pressure and exposed for 10 s to the electron beam. The white rectangles outline the following areas that were evaluated: (a) Scanned area, (b) carbon film thickness (background), (c) contamination volume, (d) thickness in the inner of the exposed area. 136
4.7 Contamination accumulated on empty grids without any treatment, after SCS cleaning, plasma and ozone cleaning and after solvent (toluene and THF) exposure and cleaning by SCS. Measurements up to 480 s beam exposure time are shown in (a), while in (b), the first 100 s are shown enlarged. 137
4.8 Thickness of contamination in the inner part of the exposed area of TEM grids after cleaning by different methods. 139
4.9 Carbon film thickness of grids after applying different cleaning treatments for hydrocarbon removal. 140
4.10 Accumulated contamination of grids prepared with toluene and pre-treated by different established methods. 142
4.11 Contamination thickness in the inner part of areas exposed to the electron beam of grids prepared with toluene and pre-treated by different established methods. 144
4.12 Carbon film thickness of grids prepared with toluene after applying different cleaning treatments for hydrocarbon removal. 145
4.13 HAADF imaging results of MoP@SILP particles dispersed in THF and dried at ambient pressure for 30 min. 146
4.14 HAADF imaging results of CoP@SILP particles dispersed in THF prepared by drying the sample in the SCS for 30 min. 147
4.15 HAADF imaging results of MoP nanoparticles dispersed in toluene and dried for 90 min at ambient pressure. 147

4.16 HAADF imaging results of MoP nanoparticles dispersed in toluene prepared by drying the sample in the SCS for 90 min. 148
4.17 Data and parabolic rate fit for the contamination of samples prepared with different methods. 151
4.18 Data and parabolic rate fit for the contamination of samples prepared with different methods. 152
4.19 Data and parabolic rate fit for the contamination thickness of samples prepared with different methods. 154
4.20 Data and parabolic rate fit for the contamination thickness of samples prepared with different methods. 155

List of tables

1.1 Typical collection semi-angles of the detectors in the Thermo Scientific Talos F200X microscope at a camera length of 98 mm. 4
1.2 Atomic fraction in % by averaging the signal of the first 50 frames and last 50 frames. 14
1.3 For the carbon K-edge measurents of different solvents, the energy resolution, relative thickness, jump ratio and number of pixel are listed. 19
1.4 Estimations of the inelastic mean free path depending on the local sample composition at 200 kV and a collection semi-angle of 41 mrad[24]. 30

2.1 Calculated reaction rate constant based on a method suggested by Chesnavich *et al.*[5] for THF, toluene and mesitylene. 54
2.2 Molecular composition of the most important parasitic ions observed during PTR MS measurements. 67
2.3 Fragmentation products of mesitylene found in PTR MS analysis. 69
2.4 Compounds found in PTR MS analysis in the range between m/z 50 and m/z 60. 72
2.5 Compounds found in PTR MS analysis of the empty octagon up to m/z 150. 72
2.6 Overview of fragments found in traces with a fluctuating signal intensity in the presence of a solvent. 74

3.1 Vapor Pressure at 25 °C and boiling point at 101.325 kPa of the solvents used in the experiments[11]. 101
3.2 Fit parameters $K_{p,V}$ and c_V as well as coefficient of determination R^2 for the fit of the contamination following a parabolic law behaviour of the different solvent samples. 110

4.1 Vapor pressure and boiling point of THF and toluene at 20 °C and 101.325 kPa[11] 130
4.2 Fit parameters $K_{p,V}$ and c_V as well as coefficient of determination R^2 for the fit of the contamination following a parabolic law behaviour of the different investigated samples. 150
4.3 Fit parameters $K_{p,V}$ and c_V as well as coefficient of determination R^2 for the fit of the contamination following a parabolic law behaviour of the contamination thickness of different investigated samples. 153

Hiermit versichere ich, dass ich die vorliegende Arbeit mit dem Titel

„Quantification of Carbon Contamination Resulting from Sample Preparation in Transmission Electron Microscopy"

selbst verfasst, keine außer den angegebenen Hilfsmitteln und Quellen benutzt habe, alle wörtlich oder inhaltlich übernommenen Stellen als solche gekennzeichnet sind und die Arbeit in dieser oder ähnlicher Form noch bei keiner anderen Universität eingereicht wurde.

Mülheim an der Ruhr, November 2023

____

Julia Menten